Spring 2017

Remote sensing and localization of smart rocks with orientation-controlled magnets for real-time monitoring of bridge scour and riprap effectiveness

Yan Tang

Department: Civil, Architectural and Environmental Engineering

Recommended Citation

Tang, Yan, "Remote sensing and localization of smart rocks with orientation-controlled magnets for real-time monitoring of bridge scour and riprap effectiveness" (2017). *Doctoral Dissertations*. 2573.
https://scholarsmine.mst.edu/doctoral_dissertations/2573

REMOTE SENSING AND LOCALIZATION OF SMART ROCKS WITH ORIENTATION-CONTROLLED MAGNETS FOR REAL-TIME MONITORING OF BRIDGE SCOUR AND RIPRAP EFFECTIVENESS

by

YAN TANG

A DISSERTATION

Presented to the Faculty of the Graduate School of the

MISSOURI UNIVERSITY OF SCIENCE AND TECHNOLOGY

In Partial Fulfillment of the Requirements for the Degree

DOCTOR OF PHILOSOPHY

in

CIVIL ENGINEERING

2017

Approved
Dr. Genda Chen, Advisor
Dr. Guirong (Grace) Yan
Dr. Lesley Sneed
Dr. Cesar Mendoza
Dr. David Pommerenke

ABSTRACT

This study aims to develop and implement a novel smart rock technology for real-time monitoring of the maximum scour depth and the effectiveness of riprap mitigation measures. A smart rock is one or more stacked magnets encased in concrete that can automatically roll to the deepest point of a scour hole around a bridge pier and provide its location through remote measurement over time. Once integrated into a riprap measure, the smart rock moves together with natural rocks and is thus a potential indicator of the effectiveness of the riprap measure. Therefore, the localization and movement of smart rocks were investigated and validated at various bridge sites. Specifically, three types of spherical smart rocks designated as Arbitrarily Oriented System (AOS), Automatically Pointing South System (APSS) and Automatically Pointing Upward System (APUS) were deployed. The AOS and APSS were employed to develop and validate the localization algorithm at an open and bridge sites. The APUS was used in smart rock prototyping for field testing and implementation at three bridge sites. It was demonstrated that the effect of steel reinforcement in bridge piers and decks on the orientation of smart rocks was negligible. The localization accuracy with a single smart rock met the general requirements for scour depth measurement in engineering application. The spherical smart rock placed directly on riverbed at Roubidoux Creek successfully demonstrated its movement to the scour hole during the December 27, 2015, flood. The smart rocks deployed at Waddell Creek and at Gasconade River, however, were washed away. Thus, additional smart rocks were deployed by making their top in flush with the riverbed for future monitoring. Additionally, spherical smart rocks are not stable for riprap effectiveness monitoring and polyhedral shapes are recommended for future study.

ACKNOWLEDGMENTS

First and foremost, I would like to express my sincere appreciation to my advisor Dr. Genda Chen for his support, expert guidance, understanding and encouragement throughout my study and research at Missouri University of Science and Technology. I would also like to thank my committee members, Drs. Cesar Mendoza, Lesley Sneed, Guirong (Grace) Yan and David Pommerenke, for their time and effort. Their thoughtful questions and comments are valued greatly.

Financial support for this study was provided by the U.S. Department of Transportation Office of the Assistant Secretary for Research and Technology (USDOT/OST-R) under Cooperative Agreement No. OASRTRS-14-H-MST and by Missouri Department of Transportation (in-kind). Special thanks are due to California and Missouri Departments of Transportation for their assistance in traffic control during field tests.

I would like to express my gratitude to the Center for Infrastructure Engineering Studies senior specialist, Mr. Jason Cox, for his assistances during field tests. Thanks are extended to Dr. Richard Elgin for allowing us to use survey equipment during field tests. I would also thank Civil, Architectural, and Environmental Engineering Department laboratory technicians, Mr. Gary Abbott, Mr. Brian Swift, Mr. John Bullock, Mr. Greg Leckrone, and Mr. Mike Lusher, for their assistance during the preparation for field tests.

I also appreciate the assistance from my fellow students and friends during field tests, including Dr. Fujian Tang, Dr. Andriy Radchenko, Mr. Yizheng Chen, Mr. Yi Bao, Mr. Zhaochao Li, Mr. Chuanrui Guo, Mr. Liang Fan, Mr. Xiuyan Hu, and Mr. Mattew Klegseth.

Last but not the least, I wish to express my special and sincere gratitude to my husband, grandparents, parents, parents in law, uncles, aunts and my brothers for their unconditional love and encouragement throughout my Ph.D. study.

TABLE OF CONTENTS

LIST OF ILLUSTRATIONS

LIST OF TABLES

1. INTRODUCTION

1.1. BACKGROUND

Bridges connect otherwise geographically isolated communities and represent one of the most significant financial investments in ground transportation infrastructure. Failure of these structures can significantly impact human welfare and economic development. In the U.S., bridges collapse due to the removal of riverbed deposits around bridge pier and abutment foundations, a process known as scour, which undermines the structural stability of bridge elements located in the flow.

Scour and other hydraulic induced failures, accounting for 58% of all bridge failures [1], have resulted in direct loss of lives and hundreds of millions of dollars in damage repair. For instance, 10 people lost their lives during the collapse of the I-90 Bridge over the Schoharie Creek in New York in 1987 when a pier footing was inadequately protected from the formation of a scour hole that undermined the pier [2 NTSB 1987]. As a result of the migration of the main channel which undermined a bridge column and thus led to the collapse of the U.S. 51 Bridge over the Hatchie River in Tennessee in 1989, 8 lives were claimed [2, 3]. The collapse of I-5 Bridge over the Arroyo Pasajero River in California in 1995 costed the lives of 7 individuals after a 9.8 ft scour hole had been developed over time [3, 4]. It is reported that the repair cost of bridges with scour damage would be $100 million per event during 1964-1972 [5]. The cost of flood repairs during the 1980s was estimated to be $300 million [6]. Between 993 and 1995, the costs for the floods in the Midwest, Georgia and Virginia were $178 million, $130 million, and $40 million, respectively [7]. Additionally, bridge collapses due to scour can have a dramatic impact on local communities with financial impact estimated to be five times the actual repair cost [8]. Therefore, it is necessary to protect these critical infrastructure elements against scour-induced potential damage.

Scour induced damage can be prevented by armoring the riverbed around bridge piers to reduce the amount of scour or by adjusting the river hydraulics to reduce the peak flow, both requiring a significant amount of time and financial resources for implementation. Scour monitoring, however, can be implemented quickly at a reduced cost relative to the other preventive measures. For this reason, the Federal Highway

Administration (FHWA)'s Highway Engineering Circular (HEC) No.23 lists scour monitoring as a viable countermeasure for scour critical bridges [9]. The existing monitoring methods, however, cannot be applied to assess the condition of bridge scour in real-time because the continuous changes in the river and flow conditions required for the prediction of the maximum scour depth [10, 11] are not made available during a flood event. Real-time monitoring and assessment of bridge scour is critical not only to maintaining ground transportation services but also ensuring the transportation safety in hours or days during flood events [2]. Therefore, real-time field scour monitoring is crucial for a more accurate prediction of scour and a further calibration of bridge design equations.

1.2. LITERATURE REVIEW

Over the past half century, the United States Geological Survey (USGS) along with FHWA and the state Departments of Transportation (DOTs) in the U.S. have made significant efforts into the study of scour at bridge sites. In 1987, FHWA funded the USGS to initiate the National Bridge Scour Program. After many years of studies, the USGS published a national bridge scour report [12], which aimed to guide the practice of engineers. From the report released by the USGS, countermeasures to mitigate bridge scour usually involve physical protection, such as riprap, and/or monitoring. In case physical countermeasures are cost prohibitive, monitoring can be used to ensure that bridge foundations are stable. Monitoring can detect the evolvement of bridge scour around piers and abutments that are either always under river or flooded in heavy raining seasons, and provide warning prior to a sudden failure, thus protecting the lives of bridge users and preventing bridges from collapsing if promptly mitigated.

1.2.1. State-of-the-art Development. Over the past few decades, measurement and monitoring instrumentation has been developed for bridge scour. FHWA's HEC-18 by Richardson and Davis [13] first recommended the use of fixed instrumentation and sonic fathometers (depth finders) as scour monitoring countermeasures. The NCHRP Project 21-3 by Lagasse et al. [9], *Instrumentation for Measuring Scour at Bridge Piers and Abutments*, developed, tested, and evaluated fixed scour monitoring methods both in laboratory and field. The NCHRP Synthesis 396 by

Hunt [14], *Monitoring Scour Critical Bridges,* assessed the state of knowledge and practice for fixed scour monitoring of scour critical bridges. In addition, the technical literature documented a number of scour detection and monitoring methods that have been developed over the past two decades.

Lagasse et al. [9] classified various monitoring techniques into portable and fixed instrumentations. Portable instrumentation such as diving, sounding rod, radio controlled boat, reflection seismic profile, and ground penetrating radar, involves a manual operation of measuring stream bed elevations at bridge foundations. The portable devices can be used to monitor the entire bridge or transported from one bridge to another so that they are cost effective tools to address the scour monitoring needs in a bridge network. However, the portable devices cannot offer a continuous detection on the scour condition of bridge foundations. On the other hand, fixed instrumentations involves monitoring devices that are attached to bridge structures to detect scour at a particular location when frequent measurements or real-time monitoring are desirable.

There are many options available for bridge scour monitoring. The selection of a most effective and appropriate monitoring method itself could be a challenge for practical engineers. Ideally, appropriate instrumentation should be selected based on site conditions, operational limitations of specific instrumentation and engineering judgment, the advantages and disadvantages of different technologies [9]. To facilitate the selection of monitoring technologies, Lueker et al. [15] developed a scour monitoring framework for instrumentation selection given site-specific bridge and stream conditions. The framework is a Visual Basic for Applications (VBA) enabling excel workbook that requires the input for site specific information of one bridge at a time, such as the details of bridge, stream, and scour; it compares the application attributes with critical characteristics of fixed scour monitoring equipment. The final output is a list of instrument ranking in the framework and an overview of how various characteristics of this application affect the ranking score for each instrument.

Although various scour monitoring techniques have been developed, by 2005 only approximately 100 out of 25,000 over-water bridges in the U.S. were instrumented due to their limitations and associated costs, among which 90% were equipped by fixed instruments. The sonar scour system was the most popular device used at 51 bridge sites, followed by magnetic sliding collar at 23 sites and float-out device at 13 sites [16]. To date, little or no real time scour data exists from historic flood events.

1.2.2. Existing Monitoring Methods. Visual inspection has been applied as a primitive and rapid visual inspection technique for bridge scour, which could not only result in a poor degree of accuracy, but also pose a threat to the safety of the diver [17]. In addition, the diver must have relevant experience in scour measurement [18].

Radar. Particularly Ground Penetrating Radar as a geophysical technique has been successfully applied to identify and determine the depth of scour [9, 18-24]. The measurement of scour depth through radar is based on the wave propagation and reflection at river bed. A diverging pulse of electromagnetic radiation from the transmitting antenna (Tx) propagates through water and experiences multiple reflections/transmissions at the bottom of the river when it encounters interfaces with different dielectric constants (e.g. sediment and river bed). The reflections propagate back to the water surface where the receiving antenna (Rx) is located. The variations recorded in the received radar signal represent the change in river bed profile.

Sonar. Following the same principle as radar, a sonar device transmits a wave toward an object to measure the time and amplitude of the reflected wave or echo. In other words, the sonar technology is based on the round trip travel time of an acoustic pulse from a sensor to the riverbed [25, 26]. Sonar instruments measure scour depth through a supersonic sensor mounted on the edge of a sounding rod extending from a bridge deck or an inspection scaffold on a bridge inspection vehicle [27]. Sonar has been developed and used to characterize the sea bed by extracting the sediment type and properties from echo signals [28]. Alternatively, sonar as a non-optical underwater imaging technology has demonstrated the most potential application in scour monitoring [29]. Underwater acoustic imaging can provide photo quality visual images of submerged elements for structural inspection documentation and channel texture information for scour monitoring during a flood event in an easy, fast and safe approach.

Although radar and sonar have been conveniently and successfully used to detect the profile of a bridge scour hole, the monitoring results are sensitive to noise and difficult to interpret especially when the water contains high concentration sediments, debris or rocks in a flooded river. Therefore, radar and sonar are usually good for applications after flooding and thus cannot detect the maximum scour depth that is achieved during a flood at a peak discharge [30].

Magnetic sliding collar (MSC). MSC is another effective device used for the detection of scour. This instrument consists of a collar wrapped around a rod with a series of magnetically activated switches at predetermined locations along the length of the rod. The rod is driven into the streambed and the collar is embedded into the streambed [1, 31]. The scour depth is determined by the movement of the collar, which slides down the magnetic rod as the deposits around the foundation is eroded away. Lu et al. [32] used an MSC and a steel rod to monitor the total bridge scour during floods. The lower tip of the steel rod was initially placed slightly below the riverbed in the main channel. When scour occurred, the steel rod would sink as the surface of the riverbed was lowered. The scour depth was determined based on the total lowering distance of the steel rod with respect to its initial position.

Tilt sensor. A tilt meter basically detects scour-related settlements of pier or abutment foundations [33, 34]. However, it can be a challenge to differentiate the movement by scour and other factors such as traffic, thermal, wind and ambient perturbations.

Float-out device. A float-out device has a radio transmitter buried in the riverbed at particular locations (a certain depth) near bridge piers or abutments. As scour develops and reaches that depth, the device floats up to the water surface and transmits a signal that can be detected by a receiver at a remote station such as bridge deck [9]. Float-out devices are inexpensive, but only measure the particular depth where each is buried. Furthermore, such a device requires replacement once activated and washed away in the river. Another similar technology using a high frequency band (13.56 MHz) radio frequency identification (RFID) system with advantages of simple and low cost is developed to directly monitor the scour condition around a bridge pier. A series of passive tags with a unique number code each are buried in the riverbed near a bridge foundation and interrogated by the reader antenna coil to check their existence. When a tag is washed away due to scour, its response disappears during the one-to-one interrogation from the RFID reader, indicating the position and depth of the scour by the pre-embedment information uniquely assigned to the tag identification number [35].

Sounding rods. Sounding rods are manual or mechanical (automated) gravity-based physical probes [6, 9, 14]. A gravity-based probe drops with any change to the streambed depth. As a result of self-weight, the probe may penetrate through granular soils. To prevent self-penetration and vibration of the rod from flowing water, the foot of the rod must be sufficiently large.

Radio-Controlled Boat. Fukui and Otuka [17] developed a Radio-Controlled Boat (RC Boat) to detect bridge scour. A RC Boat system consists of a digital fathometer for the measurement of scour depth, a telemeter transmitter of the measured data, a telemeter receiver of the measured data, a total station installed at the river bank to locate the boat, and a personal computer. The received data from the receiver and the location data from the total station are automatically transmitted into the computer for processing and evaluation of the scour depth at the streambed. The RC Boat can provide a precise streambed condition around bridge piers, but cannot be used during a flood event when debris or ice floats on water.

TDR. In recent years, time domain reflectometry (TDR) has been developed and used for real-time monitoring of bridge scour. It operates by sending an electromagnetic pulse through a transmission line with a fixed velocity. The pulse propagates down the transmission line until the end of the line or some intermediate discontinuity (air/water interface and water/sediment interface), where part of the pulse is reflected back to the source. By measuring the returning time of the sent pulse, the physical distance between the line end or the discontinuity and the TDR source can be calculated. In 1994, Dowding and Pierce [36] adopted a vertically buried TDR sensor in the sediments adjacent to a structural element. When scour occurred, a portion of the TDR sensor was exposed, broken off, and shortened by the stream flow, which can be detected and measured.

However, the TDR sensor will be destroyed and must be replaced after each scour event. Yankielun and Zabilansky [37] first introduced a TDR probe to identify the sediment/water interface for scour monitoring. The TDR sensor made of steel pipe can be permanently installed under the river bed. Field evaluation at several locations indicated that the sensor was sufficiently rugged. Even so, the intrinsic design of the probe made it difficult to install in the field condition. The acquired signals can be difficult to interpret and the application was limited to a relatively short sensing range. Attempts were made to develop a robust algorithm for scour measurements and systematically interpret TDR signals by understanding the electromagnetic wave phenomena and TDR system characteristics [38]. The automatic scour monitoring system was demonstrated in laboratory experiments; the robust algorithm can accurately evaluate the thickness of sedimentation. Yu and Yu [39] developed a theoretical framework for an automatic scour monitoring system using the TDR principle and analyzing the TDR signals to determine scour condition and sediment status. In addition, it is indicated that TDR could accurately measure the scour depth, the density of sediment materials and the electrical conductivity of river water. The robust algorithm for TDR signals was further described, assessed and evaluated by Yu and Yu [40-42] and compared with the ultrasonic method to illustrate the advantages of the new TDR in Yu and Yu [43]. A new TDR sensor was designed with a metallic coating to increase the sensing depth and the level of protection by Yu et al. [44]. Tao et al. [45] designed an innovative TDR scour sensor for field applications and the robust algorithm was used to retrieve scour information from TDR signals. To further improve the sensitivity of the TDR sensor, an spiral TDR sensor was proposed and laboratory validated for scour depth detection [46]. The sensitivity of spiral TDR is four times than that of the straight TDR due to the spirally wrapped copper wire around a rod increases the travel distance of the electromagnetic wave per unit length in the spiral probe.

Fiber optic sensor. Fiber optic sensors have been used for scour measurement in recent years based on wavelength or intensity measurement methods. They have many advantages such as long-term stability and reliability, resistance to environmental corrosion, high resolution, serial multiplexing capability, small size, geometrical and structural compatibility, immunity to electrical and electromagnetic noise, and low cost [47]. Wavelength based sensors [48-51] consists of a number of Fiber Bragg Gratings (FBG) instrumented on a rod at predetermined locations and embedded into the sediment. The scour detection principle was based on the fact that individual sensors are subjected to increasing strains when exposed to the river flow as a result of scour [49].

Lin et al. [50] designed two systems for local scour monitoring. In the first design, three FBG sensors were mounted on the surface of a cantilevered beam and arranged in series along one single fiber. In the second design, several FBG sensors were arranged along one single optical fiber, but mounted on cantilevered plates installed at different levels of a hollow steel pile attached to a pier or abutment. The beam or plates were bent in the scour process and the induced strains were measured by the FBG sensors as running water flows around the cantilevered beam or plates. The scour depth can be detected by knowing the strain information indicated from the explosion condition of the FBG sensors that were buried under the sediment or river bed [50]. This FBG-based scour sensor was subsequently installed at the Dadu bridge site in Taiwan for scour monitoring during floods. The FBG monitoring system appeared robust and reliable for real-time scour depth measurements [51]. Huang et al. [52] developed a new type of optical FBG-based scour monitoring sensors that excluded the influences of soil pressure and static water pressure varying with the depth. In addition, FBG sensors were embedded in a fiber reinforced polymer beam to improve the accuracy and durability of measurement [53]. Three designs of a scour monitoring system using FBG were compared in terms of the measurement of water level, maximum scour depth, scour process and refilling deposition height [30]. The proposed system was tested in the laboratory and then implemented with two test piles at a bridge site for long-term monitoring [54]. The intensity-based measurement of scour depth is related to the fundamental frequency of vibration of a rod embedded in the riverbed to the scour depth and a single FBG sensor was used to measure the vibration frequency to obtain the scour depth by the inverse relationship of fundamental frequency and the length of the sensor rod [34]. In addition, a scour monitoring network of polymer fiber optic sensors (PFOSs) and MicroElectroMechnaical System (MEMS) such as switches, phototransistor, LED, amplifier, detector and multiplexing system [55] was designed and fabricated for monitoring and detecting scour at bridge piers and abutments; the response of sensor was greatly affected by the reflection property of different mediums so that the scour was detected by the change of various mediums. However, for the use of FBG sensors, installation design and fabrication techniques remain to be improved to withstand harsh operation conditions in field application [51].

Piezoelectric film sensors. Piezoelectric films were applied to monitor the water flow condition since voltage was generated as they were deformed (bent) under the effect of water flow [56, 57]. Such a sensing device was built by attaching piezoelectric thin films to a rod at certain spacing and inserting the rod into a guide rail installed next to the bridge pier. If the embedded piezoelectric films in the riverbed were disturbed by the water current as a result of scour, the output voltage were large than that when not disturbed. Therefore, the signals from all the piezoelectric sensors can indicate the variation of soil/water interface before, during and after a food event. This device may lead to false measurements as the result of high sensitivity [58].

Temperature sensors. Bridge scour can also be detected based on the measurement of temperature variations at the water/sediment interface. A series of thermocouples spaced 2 inches apart along a partially buried rod may determine the scour depth by measuring the temperature gradient along the length of the rod [59]. The FBG sensors were also adopted as an array of temperature sensors instrumented along the length of a rod buried in the sediment to measure in real time the scour depth around a structure under both ordinary and flood conditions [60-62]. The rate of heat loss of the heated FBG by an electrical circuit embedded in sediment is slower than that in the flow; therefore, when the temperature of sensors buried in the sediment is large than those in flowing water, the bed level can be detected. The same idea based on the theory of heat conduction was also employed to develop a new design of temperature-based sensor consisting of a stainless steel cuboid shell, a heating piece and two temperature probes for bridge scour monitoring [63]. The laboratory test, numerical analysis, and in-situ field test were conducted to study a new large-diameter, hollow tube as a heat probe for scour monitoring based on the different thermal properties of two environments: water and soil [64]. These temperature-based devices are simple in concept to understand and available for scour monitoring. However, they may not be accurate enough to read a temperature change over small intervals. Their validations are mainly limited to laboratory evaluation.

Vibration based methods. The vibration-based methods have been used to relate the dynamic response of a bridge to the scour condition of bridge foundations [65]. The average spectral shape of the vibration of a bridge measured from two three-axis accelerometers deployed on the upstream and downstream side of a pier was monitored to see if the natural frequencies of the pier had been changed. A similar approach was taken to monitor both the natural frequency and the mode shape of a bridge, which were related to the sediment variation surrounding the bridge foundations [66]. A tilt sensor was used to monitor sensitive bridge columns by relating the fundamental frequency of the bridge with the scour depth [67]. Although the vibration-based measurements are a potential indicator to the health of piers, variations in ambient temperature and traffic loading could cause more changes in the fundamental frequency of a pier than changes by the bridge scour. Vibration-based turbulent pressure sensors (VTPs) were proposed to detect scour by installing them on a partially-buried pipe [68]. The energy content of each VTP along the pipe was monitored to indicate the scour level since the energy content of the sensors exposed to water flow is one or two orders of magnitude greater than that of the sensors buried in the sediment. The VTP sensors have been shown to be reliable and robust in harsh hydraulic environments [58]. However, the VTPs are still limited to the length of a pipe and the vibration may be caused by debris or traffic loading. More recently, the natural frequency of a pile was monitored and numerically analyzed to detect the presence of scour and possibly estimate the scour depth [69]. The developed numerical model was further extended to consider the effect of a bridge superstructure and establish the relationship between the structure's natural frequency and the scour of the foundation [70]. A vehicle-bridge-soil interaction (VBSI) model was developed to possibly detect changes in frequency using the bridge dynamic response to a passing vehicle. An Extended Kalman Filter (EKF) using the time history of dynamic measurements along with a finite element model was proposed to identify the scour depth with high sensitivity and better accuracy [71].

Tracking or imaging sensors. Lin et al. [72] used distributed MEMS sensors for pressure measurement. Chang et al. [73] developed a multi-lens monitoring system that can track scour images and retrieve the scour information through an image recognition process. Another tracking technique for sediment transport and scour around bridges was developed by Lauth and Papanicolaou [74] using radio waves, a communication between a RFID and transponders embedded in individually tracked particles that are directly involved in the process of scour. A combination of multi-beam ultrasonic echo sounders and vibrating wire piezometers was used to measure and map the riverbed topography and detect local scour appeared within and around the pile group [75, 76]. A three dimensional profiling of the river bed around bridge piers has also been attempted using a rotatable sonar profiler [77, 78]. The scour monitoring around a bridge can be realized by tracking the bed-level images with a micro camera mounted on a movable holder that can be driven by the motor to move on the rail fixed on the pier. The system can recognize in real time the bed-level position and obtain the scour-depth evolution by adopting two scour image processing methods: brightness intensity segmentation (BIS) and particle motion detection (PMD) [79].

Smart scour sensor. A post instrumented with an array of wireless smart scour sensors at varying heights can be installed around bridge abutments or piers to monitor the sediment depth and profile around the foundation in real time [80]. The sensor array is composed of bio-inspired, whisker-shaped magnetostrictive flow sensors that are highly rugged, self-powered, and able to detect water flow by bending. The sensors located above the sediment level respond to the dynamic flow and the sensors located below the sediment line only return with static measurements. A real-time bridge pier scour monitoring system with low cost commercial hall-effect sensors was developed and verified in laboratory experiments [81]. The monitoring system is based on a master-slave configuration composed of a host controller (master), a gateway (slave), a Power over Ethernet (POE) switch and a sensor node to send and receive commands and access the data collected. The sensor node is configured with a thin metal strip attached with a neodymium magnet and a hall-effect sensor. The distance between the magnet and the hall-effect sensor varies as the thin metal strip is bent due to water flow, and the variation is reflected by the output voltage of the hall-effect sensor. During experiments, it was observed that the output voltage of the hall-effect sensor dropped quickly when the sensor node buried in the sand was washed away due to the rapid scour erosion. The slow scour process and partial sand removal around the hall effect sensor module results in a slow rate of voltage change in the hall-effect sensor. Therefore, the scour condition is evaluated according to the rate of voltage change of the corresponding pre-buried hall-effect sensor node. Similarly, a rugged sensor system using under-water sensor node buried deeply in the riverbed close to the bridge pier was developed to monitor scouring condition of the bridge pier in real time [82]. The under-water sensor node consists of two stacked octagon PCBs with a plastic enclosure that is then set up in a steel hollow ball. An accelerometer attached on the PCB is steady in normal condition when the under-water sensor is fully buried in the sand. However, it would be exposed and vibrate when the sand of the riverbed is scoured due to the river water flow during a heavy rain or storm. Therefore, the vibration data of each sensor sent to the control box can be used to identify the scouring condition.

Medium property sensor. A scour probe embedded into the sediment next to a foundation to detect underwater bed level variation based on the measurement of soil electromagnetic properties was proposed to remotely monitor in real time scour and sediment deposition processes [83]. Another similar approach for scour depth measurement was to measure the oxygen level of water to identify the water level around a pier. The optical dissolved oxygen (DO) probes [84] were installed along the buried length of a bridge pier or abutment to monitor DO levels at various depths. The scour depth is then evaluated by comparing the DO levels of sensors embedded in soil, which are negligible, to those exposed to water flow because of scour, which will increase significantly and reach the flowing water DO level.

1.3. RESEARCH OBJECTIVES AND SCOPE OF THIS WORK

The above review clearly indicated two groups of scour monitoring techniques: fixed and portable instrumentations. The fixed instrumentation is installed prior to storm events and limited to the measurement of scour condition near the fixed location around a bridge pier or abutment. Two challenges arise in applications. First, the scour information monitored may not be most critical due to fixation of the monitoring devices in horizontal plane. Second, whether the monitoring device can survive the harsh environment during a flood event is yet to be tested. Although the portable instrumentation can be applied to cover a wide area of a bridge pier or abutment, it is too risky to operate most, if not all, the portable devices during a flood event. Overall, monitoring the scour process of a pier or abutment during a flood event is an unsolved challenge in bridge engineering.

The goal of this study is to develop and implement a novel smart rock technology for the measurement of scour depths and the effectiveness detection of riprap mitigation measures in real time. The main objectives of this study are to: (1) develop, design, package, and prototype smart rocks; (2) develop and validate the localization algorithms of smart rocks at several test sites; and (3) implement the smart rock technology at representative bridge sites. To achieve the main objectives, seven research tasks are designed and planned as follows:

1. Design guidelines of smart rocks for scour and riprap effectiveness monitoring,
2. Type, prototyping, and deployment of smart rocks at three bridge sites,
3. Localization of a single smart rock in uniform ambient magnetic field,
4. Localization of a single smart rock in non-uniform ambient magnetic field,
5. Localization of two smart rocks in non-uniform ambient magnetic field,
6. Evolutionary mapping of smart rocks over time, and
7. Semi-active smart rocks for enhanced sensitivity and spatial resolution.

Tasks 1 and 2 address the first objective. Tasks 3-5 and 7 are designed to achieve the second objective. Tasks 2 and 6 are proposed to meet the third objective.

1.4. ORGANIZATION OF THIS DISSERTATION

This dissertation consists of seven sections. Section 1 introduces the main objectives and scope of work, literature reviews on bridge scour monitoring, and seven technical tasks that will be addressed in the following five sections. Section 2 introduces the development of the smart rock technology, deals with the design of smart rocks for scour and riprap effectiveness monitoring, and finalizes the smart rocks for three different bridge sites. Section 3 deals with the localization of a single smart rock with an automatically pointing south magnet or with an arbitrarily oriented magnet in uniform ambient magnetic field. Section 4 deals with the localization of a single smart rock automatically pointing south magnet or with an arbitrarily oriented magnet in non-uniform ambient magnetic field. Section 5 presents the field implementation of smart rocks at three bridge sites and the validation of the localization algorithms developed in Section 4. To improve the sensitivity and spatial resolution of smart rocks based on the static measurement of magnetic fields, Section 6 explores a semi-active concept of smart rock with an embedded magnet and communication electronics for the dynamic measurement of magnetic fields. The main research outcomes, findings, and future studies are summarized in Section 7.

2. SMART ROCK TECHNOLOGY FOR BRIDGE SCOUR AND RIPRAP EFFECTIVENESS MONITORING

2.1. CONCEPT AND MEASURAND OF SMART ROCKS

Smart rocks are either natural rocks or concrete encasements with embedded permanent magnets. Properly-designed smart rocks automatically roll to the deepest point of a scour hole when deployed in top river-bed deposits around a bridge pier. Once accurately positioned over time, they can function as field agents to collect the scour depth as scour develops. During a flood event, the scour depth data can be transmitted to the engineer-in-charge or decision makers through remote measurement of the magnetic field strength of the magnets in smart rocks. In addition to the maximum scour depth that is most critical to the engineering design and maintenance of bridge foundations, smart rocks can be used to evaluate the effectiveness of a rip-rap scour countermeasure in real time since rock movement is an indicator of its incipient failure.

To track the location of a smart rock, a commercial magnetometer is used to measure the intensity of the total magnetic field of the Earth, the permanent magnet inside the rock and any other ferromagnetic substances. A piece of survey equipment is employed to survey the measurement stations of the magnetometer. The position of the smart rock can be inversely obtained through a mathematical relationship between the magnetic intensity and the position of the magnet inside the smart rock. Therefore, the measurand for bridge scour monitoring is the intensity of magnetic field and the positions of the measurement stations.

2.2. APPLICATION SCENARIOS OF SMART ROCKS

For scour monitoring as illustrated in Figure 2.1(a), properly-designed smart rocks are near-surface deployed in riverbed deposits on the upstream of a bridge pier. They can automatically roll to the deepest point of a scour hole as it develops over time, and thus provide the maximum scour depth through their positioning by remotely measuring the magnetic field of the embedded magnet with a magnetometer from the bridge deck. When the scour hole is refilled, the smart rocks can be buried into debris and deposits but still give the maximum scour depth to which the bridge pier is ever exposed. A smart rock can be tracked over time by measuring its disturbance to the ambient (the Earth +

other ferromagnetic substances) magnetic field with a magnetometer set up at several remote stations. Since the maximum scour depth is directly associated with the position of the smart rock, localization of the smart rock is a major effort in bridge scour monitoring.

For riprap effectiveness monitoring as illustrated in Figure 2.1(b), smart rocks are mixed with natural rocks that are used to protect a bridge pier. The incipient motion of properly-deployed smart rocks is a good indication of riprap disassembling. Like scour hole monitoring, localization of the smart rocks is critical in this application.

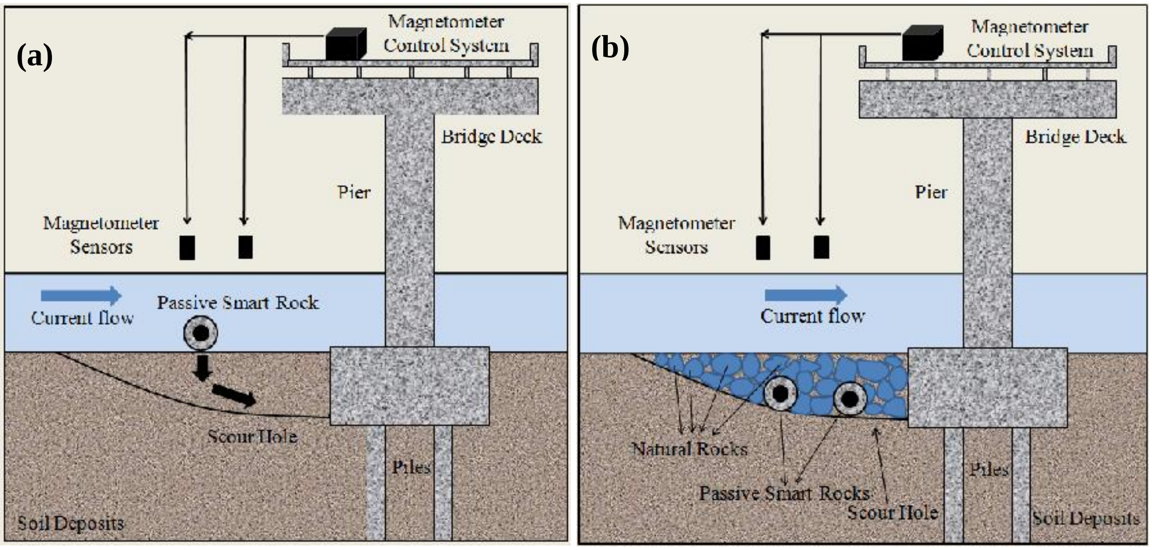

Figure 2.1. Two application scenarios of smart rocks: (a) maximum scour depth monitoring and (b) riprap protection effectiveness monitoring.

2.3. DEVELOPMENT OF SMART ROCKS

A smart rock can be made of a spherical concrete encasement of one or more permanent magnet(s) for easy rolling to the bottom of a scour hole in application. For maximum magnetic field strength, off-the-shelf (large, cylindrical) permanent magnets can be selected to fit into the design size of a smart rock. To date, neodymium-iron-boron ($Nd_2Fe_{14}B$) magnet is one of the most advanced permanent magnets commercially available in the world. As such, two types of magnets, N42 (Br Max: 1.32 Tesla) with 10.2 cm (4") in diameter and 5.1 cm (2") in thickness and N45 (Br Max: 1.38 Tesla) with 15.2 cm (6") in diameter and 5.1 cm (2") in thickness are considered. The magnet(s) can be arranged differently inside a concrete encasement, resulting in different types of smart rocks. For instance, a N42 magnet can be configured to make its poles to be directed randomly, to geographical South Pole, and upward. The three types of configuration are referred to as Arbitrarily Oriented System (AOS), Automatically Pointing South System (APSS), and Automatically Pointing Upward System (APUS).

2.3.1. AOS. The easiest and simplest fabrication of a smart rock is just to encase a magnet in a sphere concrete mold to form the AOS whose magnet pole direction rotates arbitrarily as the smart rock moves under water flow. Figure 2.2(a) and 2.2(b) show the schematic view and one prototype of a smart rock with the AOS.

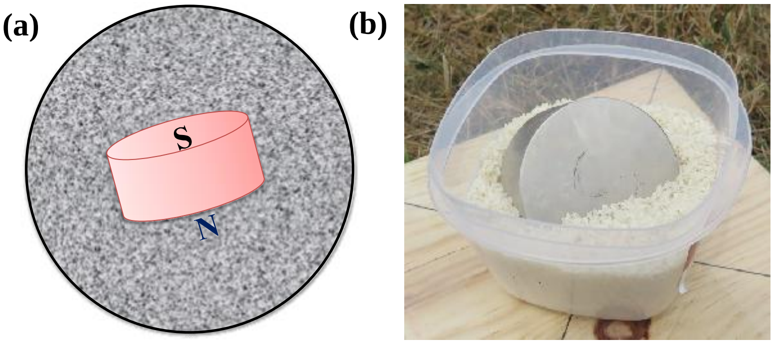

Figure 2.2. AOS design: (a) Schematic view with concrete and (b) Primitive view.

2.3.2. APSS. Like a compass that has been widely used for direction and navigation around the world, the magnet embedded inside a smart rock can be designed such that it always points to the North Pole or near geographical south of the Earth. Such a magnet and its supporting components constitute an APSS proposed and developed in this study. The pole direction of the magnet always points to the North Pole of the Earth’s magnetic field as the smart rock moves or rotates under water flow. Since the magnetic field around a magnet is directly related to the rotation of the magnet, the fixed direction simplifies the calculation of the magnetic field and thus the optimization process to locate the smart rock.

Figure 2.3(a) shows the schematic view of an APSS design. The key to this design is to create a frictionless mechanism that makes a magnet free to rotate at all times. This design consists of an inside organic glass ball, an outside organic glass ball, low viscosity liquid filled in between the two balls, one cylindrical N42 magnet placed into the inside ball, a level indicator, and some copper beads distributed as balanced weights. As shown in Figure 2.3(b) for the final design, the magnet is 10.2 cm in diameter and 5.1 cm in height. Its side face is glued to the surface of the inside ball with a diameter of 20 cm. The outside ball has a diameter of 22 cm. The inside ball with the magnet and the level indicator is designed to remain in equilibrium or to be free to rotate once the inside ball floats within the outside ball. Therefore, the magnet in the APSS will always point to the North Pole of the Earth's magnetic field, which is near the geographical South of the Earth.

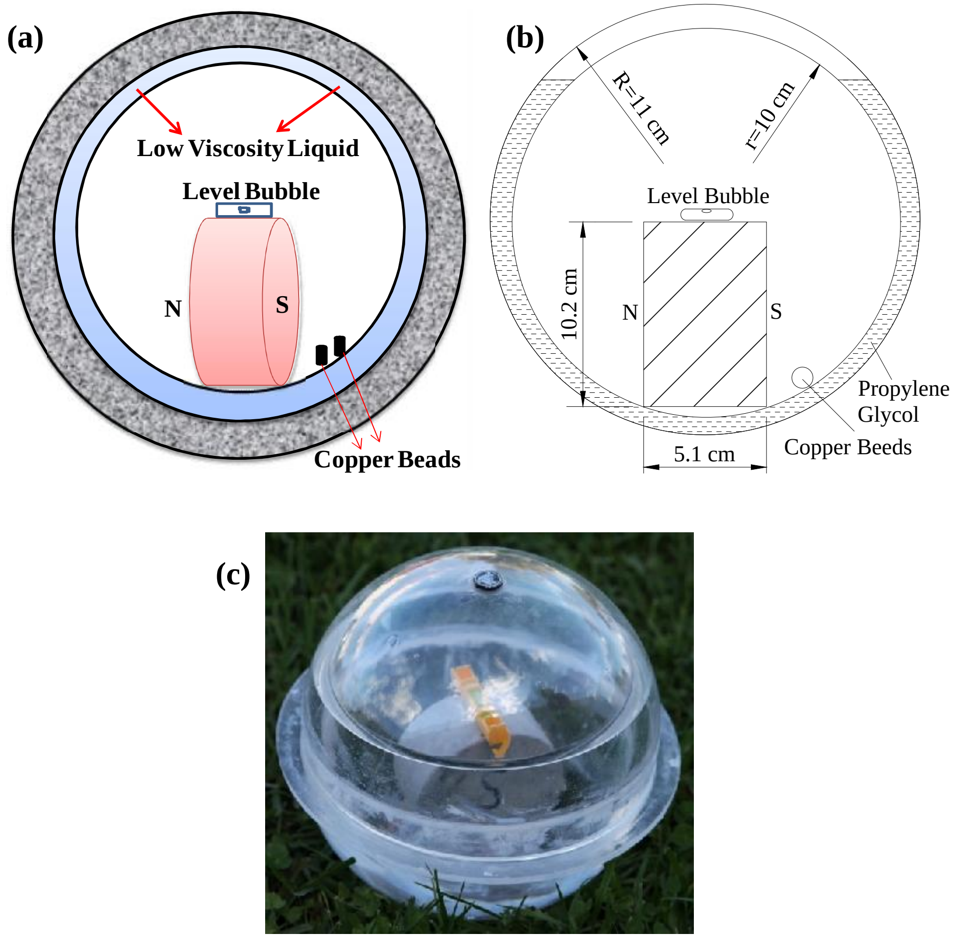

Figure 2.3. APSS Design: (a) schematic view with concrete encasement, (b) specifications, and (c) first prototype.

2.3.3. APUS. Like the APSS, an APUS is made of two concentric plastic balls. In this case, however, the center axis of the magnet fixed to the inside ball is perpendicular to the ground and the South Pole of the magnet is directed upward or downward based on unbalanced weights. Unlike the APSS, the gravity-based APUS is designed to be not influenced by any surrounding ferromagnetic objects in practical applications. Figure 2.4 shows the design of an APUS with the same size of two concentric balls and N42 magnet as those of the APSS.

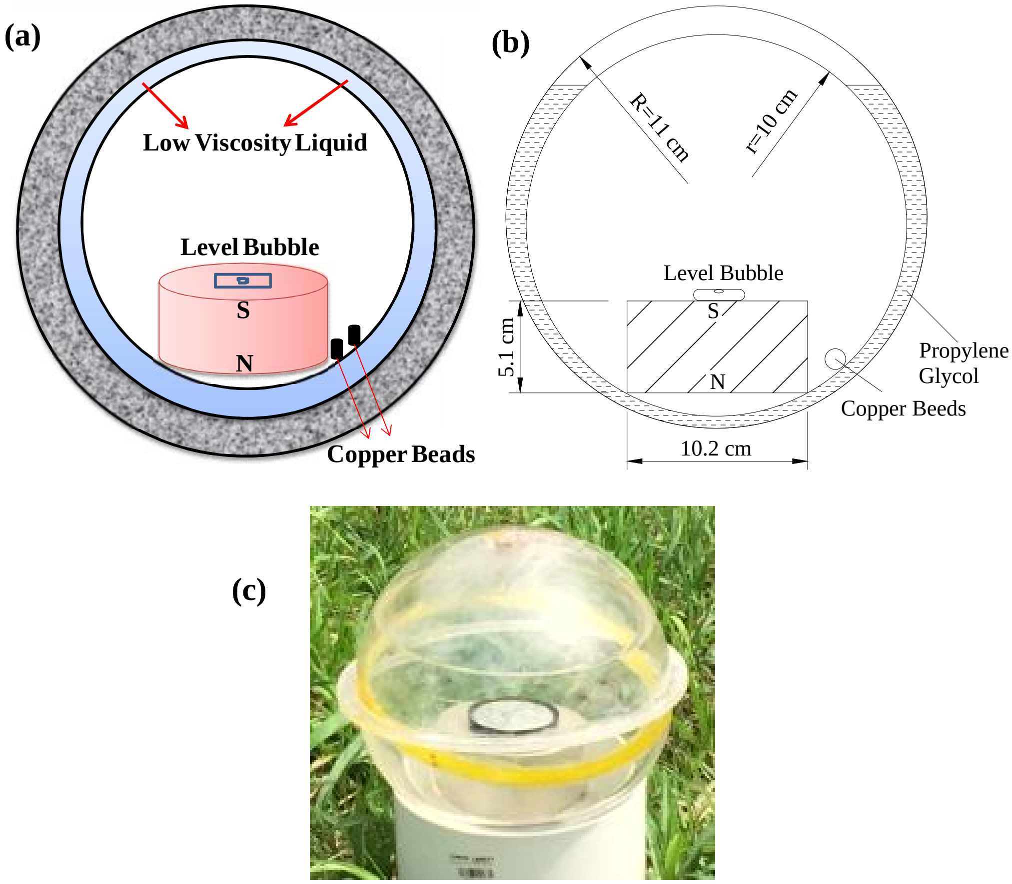

Figure 2.4. APUS design: (a) schematic view with concrete encasement, (b) specifications, and (c) primitive prototype.

2.3.4. Design Guidelines. Smart rocks are natural rocks or concrete encasements with embedded objects to facilitate the remote measurements of their spatial locations. They are passive when the embedded objects are permanent magnets and the magnets are remotely located with one or several magnetometers, and active when the embedded objects are sensors and communication devices and the sensors are located from a remote measurement station through wireless communication. When deployed near a scour critical bridge pier, smart rocks are displaced as their underlying deposits are eroded away. Therefore, properly-designed smart rocks can provide the critical information about the onset movement of riprap slope protection. If the motion of smart rocks can be controlled such that the rocks remain at the bottom of a developing scour hole near the bridge pier, the smart rocks can also provide critical information about the maximum scour depth, which is the most important parameter in bridge engineering and design for scour effect.

2.3.4.1 Design considerations. Smart rocks are designed to meet two requirements: 1) facilitate remote measurement for rock localization and 2) ensure automatic movement to the bottom of a scour hole to be monitored. The size of smart rocks is often constrained by the minimum size of embedded objects, such as permanent magnets, that are required for sufficient localization accuracy and measurement distance. The size and density of smart rocks must be selected such that the rocks can always stay at the river bed, overcome water current and roll down the slope of a scour hole, and remain at the bottom of the hole. Therefore, the density of smart rocks should range from that of water and that of rocks used in riprap slope protection.

To overcome water current and roll down the slope of a scour hole, the size and density of smart rocks highly depend on the critical velocity of water flow and the water depth at a bridge site. The critical velocity of water flow is defined as the velocity at which deposits at the river bed begin to move or when the local shear stress of deposits exceeds its critical value. The water depth represents the effect of gravity on the movement of smart rocks, which affects the critical velocity of water flow.

For simplicity, the equation for the critical velocity of water flow in HEC 18 and the equation for the riprap size in scour protection in HEC 23 are referenced in the determination of the size and density of smart rocks. The two equations in SI units are rewritten as follows:

$$d = \frac{(nV_c)^2}{K_s y^{1/3}\left(S_s - 1\right)} \tag{2.1}$$

$$D_{50} = \frac{0.692(KV)^2}{2g\left(S_s - 1\right)} \tag{2.2}$$

where d represents the size of a smart rock in *m*; n is the Manning's roughness coefficient; V_c is the critical velocity of flow in *m/s*; K_s is a dimensionless Shields parameter related to the initiation of motion of smart rocks (0.052~0.054 for cobbles and boulders); $S_{s=} \rho_s/1000$ where ρ_s is the mass density of smart rocks in kg/m^3; y is the depth of water flow in m; D_{50} is the median diameter of smart rocks in m; K is the coefficient for pier shape (1.5 for round-nose piers and 1.7 for rectangle piers); V is equal to the average channel velocity, m/s, multiplied by a coefficient of 0.9 for a pier near the river bank in a straight uniform stream or 1.7 for a pier in the main current of flow around a bend; and g is the gravitational acceleration in m/s^2.

2.3.4.2 Design procedure. A 3-step design procedure for the selection of the size of the size and density of smart rocks is described as follows.

Step 1**:** Determine hydraulics parameters near a bridge site. The flow velocity in the channel at a bridge site and the water depth directly in the upstream of scour critical piers, corresponding to a 100-year flood, are two most important parameters needed for the selection of smart rock size and density. They can often be found from hydraulic studies by the United States Geological Survey (USGS) or Federal Emergency Management Agency (FEMA).

When no hydraulic studies are available near a bridge site, the flow discharge from a recent flood event and its corresponding water depth are first estimated from the data collected at any USGS gage station deployed at the upstream or downstream of the bridge site. Considering no water loss, the flood discharge at the bridge site is assumed to be equal to that in the upstream or downstream of the bridge site. The average channel velocity can then be estimated by dividing the flood discharge by the flow cross section, which in turn depends on the water depth at the bridge site. For a given water depth, the flow cross section can be estimated based on the as-built bridge drawings or a site visit with necessary measurements. Next, the local velocity at a scour critical bridge pier is determined by multiplying the average channel velocity by an amplification factor depending on the shape of river at the bridge site, the location of the pier (in main channel or close to the river bank), and the shape of the pier. Finally, the relationship between the local velocity and water depth can be established for sensitivity analysis.

Step 2: Constrain the size and density of a smart rock. Eq. (2.1) is applied to guide the selection of the size and density of a smart rock. With the local velocity and water depth from Step 1, the size of a smart rock can be related to the density of the rock in an inversely proportional relation. In other words, the larger a smart rock, the lighter the rock for given local velocity and water depth. In practice, either the size or density of a smart rock can be estimated from application needs. For example, the minimum dimension of a magnet to be embedded in a smart rock to meet the required localization accuracy and measurement distance can be referenced in the selection of rock size (e.g. > 20 cm). The density of the smart rock can then be determined correspondingly. Alternatively, the density of a smart rock can be considered to be same as that of natural rocks (2,650 kg/m^3), particularly when the smart rock is deployed to monitor the effectiveness of a riprap slope protection strategy. However, the size corresponding to the density of natural rocks is too small in general. Therefore, smart rocks should be sized first before their density is determined from the critical flow velocity and riprap sizing equations.

Step 3: Finalize the design of smart rocks. After the size and density of smart rocks have been estimated in accordance with the incipient motion of the rocks, the size and density must be modified by a design factor (1.2~1.3) that accounts for any uncertainties associated with the estimation of hydraulic data and the use of empirical equations. By considering the design sensitivity to the flow velocity and water depth at the bridge site and the physical constraint on the size and density of smart rocks, several choices of smart rocks are determined. The final selection of the size and density is made by rounding up their calculated numbers and easing the deployment and fabrication of smart rocks, such as the use of standard mold sizes for the casting of concrete encasement.

2.3.5. Evaluation of Size and Density of Smart Rocks at Various Bridge Sites.

The incipient motion of a single particle is likely activated by the threshold condition between erosion and sedimentation of the rock. Based on the river geometrics, the hydraulic conditions, the channel bed shapes, the bed sediment size, and the viscous properties of the bed sediment materials, different empirical criteria can be used to evaluate the incipient motion of a sediment particle. According to HEC18, the critical velocity V_c is referred to as the velocity at which cohesionless particles begin to move. Similarly, the critical shear stress τ_c is referred to as the shear stress that represents the initiation of motion for cohesionless particles. In addition, the HEC 23 provided a formula for rock riprap sizing d_{50} on a channel bed around bridge piers. These approaches were the empirical equations obtained through model experiments and may have different application limitations. Since the critical velocity of a rock is derived as its local shear stress reaches a critical value referred as the critical shear stress, the outcomes from critical velocity or critical shear stress are equivalent. The incipient motion empirical Eq. (2.1) and Eq. (2.2) provided in Section 2.3.4 will be employed to evaluate the size and density of smart rocks at different bridge sites.

In this study, three bridges over rivers or creeks are selected for validation testing of the monitoring technology with smart rocks. One of them is located in California on Highway 1 over the Waddell Creek (Br. No. 36-0065). The other two bridges are located in Missouri on US63 Highway over the Gasconade River and I-44 Highway over the Roubidoux Creek.

According to guidelines described in Section 2.3.4, in order to increase the effective measurement distance for magnetic fields, two stacked N42 magnets (10.2 cm or 4" in diameter and 10.2 cm or 4" in total height) or one larger N45 magnet (15.2 cm or 6" in diameter and 5.1 cm or 2" in height) are considered as the magnetic core of a smart rock for field deployment. The sizes of inside and outside balls are also increased to meet the floating requirement of the inside ball with the two stacked magnets within the outside ball. The diameters 25 cm and 28 cm, commercially available for the inside and outside balls, are respectively selected. Further, to cast concrete encasement as the enclosure of a smart rock, a 36.8 cm (14.5 in)-diameter standard mold is selected. Substituting this size of smart rock (d = 36.8 cm or 14.5 in.) into the incipient motion Eq. (2.1) and Eq. (2.2) yields the density of smart rocks for three bridge sites:

2.3.5.1 Highway 1 over the Waddell Creek (Br. No. 36-0065). The bridge is located approximately 28 km (17 miles) north of the City of Santa Cruz in Santa Cruz County. Built in 1947, the 4-span structure as shown in Figure 2.5 is 55.1 m (180.8 ft) long and 9.7 m (31.7 ft) wide. Continuous reinforced concrete (RC) T-girders are supported on RC piers and seat-type abutments. In the upstream of the bridge, the terrain is dominated by small mountain ranges that flank both sides of the creek. In the downstream of the bridge, the channel alignment changes with flow intensity as it flows through the beach (loose, coarse sand) towards the Pacific Ocean.

In February of 2000, high flows from a storm caused severe erosion to the upstream channel banks of the south roadway approach, extending into the embankment at Abutment 1. The high flows also exposed some piles at Pier 2 up to 2.7 m (9 ft). Rock slope protection (0.7 to 1 m in diameter) was placed in March of 2000 along the eroded sections of the roadway embankments and channel banks. Since then, this bridge has been classified as scour critical. In order to estimate its scour potential, hydraulic parameters (flow skew, tidal influence, flow contraction, and pressure flow) were obtained from an advanced 2-D hydraulic model established by the California Department of Transportation (Caltrans).

Figure 2.5. Highway 1 Waddell Creek Bridge.

The 100-year flood discharge (Q_{100}) in the channel was estimated from the regional flood-frequency equation based on the historical gage data from USGS. It was calculated to be 162 m^3/s and rounded up to 170 m^3/s in this study. During the 100-year flood, the high water elevation (HWEL) reached 2.865 m, which was well below the bottom of girder elevation (El = 4.145 m). Therefore, no submersed condition existed and no pressure flow occurred. In normal conditions, the uncontrolled tide from the Pacific Ocean has no effect on the flow elevation at the bridge site. The flow depth (y) and velocity (V) in the directly upstream of various piers obtained from the 2-D analysis model are listed in Table 2.1. The materials in channel bed varied from coarse sands to large cobbles. Specifically, coarse sands were noted in the vicinity of the bridge, small pebbles were found in the upstream of the bridge, and pebbles and/or cobbles were noted in the downstream of the bridge. The Manning's roughness "*n*" value was 0.02 for the channel and beach areas, 0.04 for the grassy banks, 0.045 for the large rock slope protection zone, and 0.10 for the bank sections lined up with small trees.

Table 2.1. Hydraulic Parameters at Various Bents

Bent No.	2	3	4
y (m)	3.566	2.012	0.152
V (m/s)	2.286	3.048	1.585

It was concluded by Caltrans that Bent 2 would be laterally unstable during the anticipated 100-year flood event due to excessive pile exposure. Scour at Bents 3 and 4 should not have any instability issues. Therefore, the hydraulic parameters at Bent 2 were selected to estimate the size and density of smart rocks in this study.

The evaluation for scour depth and riprap effectiveness monitoring at Bent 2 was conducted based on the critical velocity and the riprap size, respectively. Eq. (2.1) was used to estimate the density of a smart rock from the critical velocity equation with the following parameters: $K_s = 0.052$ for fine cobbles from the USGS Scientific Investigations Report 2008-5093; $S_s = \rho_s/1000$, where ρ_s is the mass density of smart rocks in kg/m^3; $g = 9.81\ m/s^2$; $d = 0.368$ m for smart rocks based on the required space for magnet embedment; $V_c = V = 2.286\ m/s$ at Bent 2; $y = 3.566\ m$ at Bent 2; and $n = 0.041\mathrm{d}^{1/6}=0.0347$. That is,

$$2.286 = \frac{0.052^{1/2}\left(\frac{\rho_s}{1000}-1\right)^{1/2} 0.368^{1/2} 3.566^{1/6}}{0.0347}, \quad \rho_s = 1215\, kg/m^3$$

2.3.5.2 US63 Highway over the Gasconade River (Br. No. A3760). The bridge over the Gasconade River on US Highway 63 is located approximately *8.9 km* (*5.5 miles*) southeast of Vienna in Maries County, MO. Built in 1970's, it is a 12-span concrete-girder structure as schematically shown in Figure 2.6. The main flow goes between Bents 4 and 5 during dry seasons. During a flood season, Bent 4 could be potentially subjected to severe contraction scour and local scour, threatening the safety of the bridge. The 100-year flood discharge in the channel ($Q_{100} = 4234\ m^3/s$ or $146000\ ft^3/s$) was estimated from the historical data recorded from the USGS gage station at Jerome, MO (gage No. 06933500).

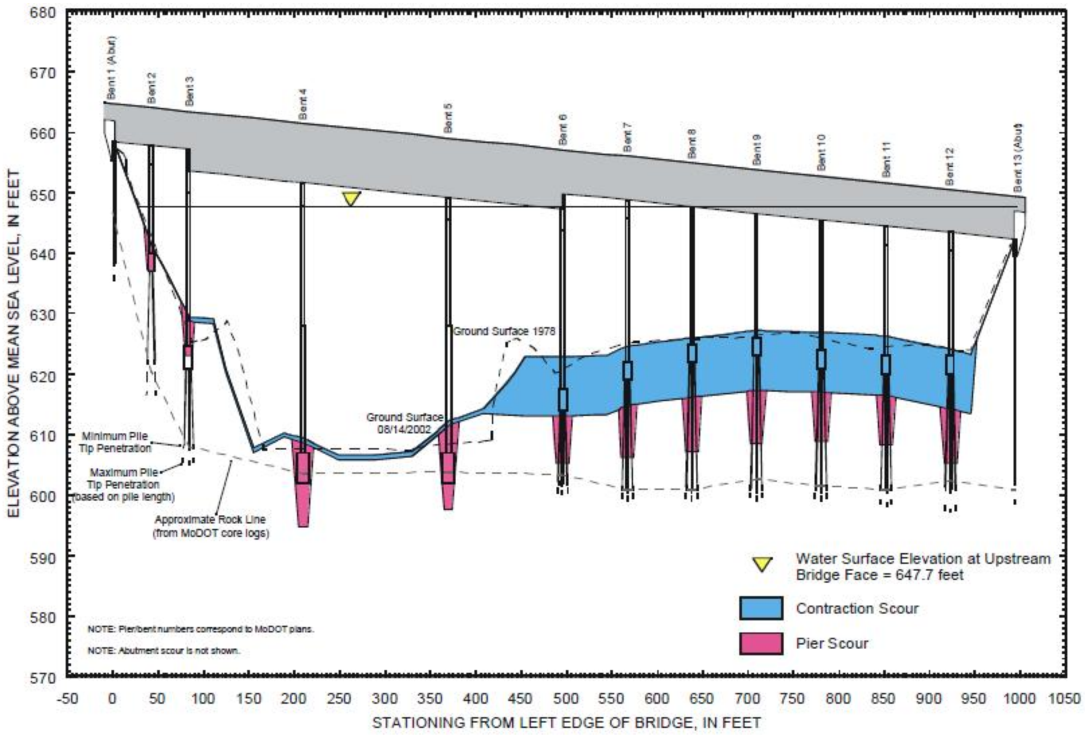

Figure 2.6. Scour condition of the Gasconade River Bridge.

The average flow velocity at the bridge site was estimated by dividing the 100-year discharge by the cross sectional area of the channel. Based on the as-built bridge drawings and flow elevations, the cross sectional area (A) was estimated to be $3395\ m^2$ ($36544\ ft^2$). Thus, the average channel velocity $V_{average} = Q_{100} / A = 1.218\ m/s$. The velocity directly in the upstream of Bent 4 was then calculated by multiplying the average channel velocity by *1.7* for a pier in the main current of flow. The flow depth at Bent 4 is approximately *12.2 m* (*40 ft*) estimated from Figure 2.6. Once again, the diameter of smart rocks was taken to be *0.368 m*, and $n = 0.041d^{1/6} = 0.0347$. Therefore, the density of smart rocks can be determined from the critical velocity criterion.

$$1.218 \times 1.7 = \frac{0.052^{1/2}\left(\frac{\rho_s}{1000} - 1\right)^{1/2} 0.368^{1/2} 12.192^{1/6}}{0.0347}, \quad \rho_s = 1117\, kg/m^3$$

2.3.5.3 I-44 over the Roubidoux Creek (Br. No. L0039). The Interstate I-44 over the Roubidoux Creek near Waynesville, MO, is located about *19 km* (*12 miles*) South of Crocker in Pulaski County. From the bridge drawings provided by Missouri

Department of Transportation, this bridge has 10 spans with the main flow going between Bents 5 and 7 as shown in Figure 2.7. The pier at Bent 6 may be scour critical. Since there is no documented record for the 100-year flood discharge near the bridge site, the maximum discharge and flow depth ($Q_{max} = 515.4\ m^3/s = 18200\ ft/m^3$ and y = 5.70 m = 18.7 ft) recorded at the USGS gage station (USGS 0698300, Roubidoux Creek above Fort Leonard Wood, MO) during the flood event in August, 2013, were used in calculation. The cross sectional area (A) during the flood event was estimated to be $1087\ m^2$ ($11703\ ft^2$) from the bridge drawings. Therefore, the average channel velocity $V_{average} = Q_{max}/A = 0.474\ m/s$, and the velocity directly in the upstream of Bent 6 was estimated by multiplying the average channel velocity by a coefficient of *1.7*.

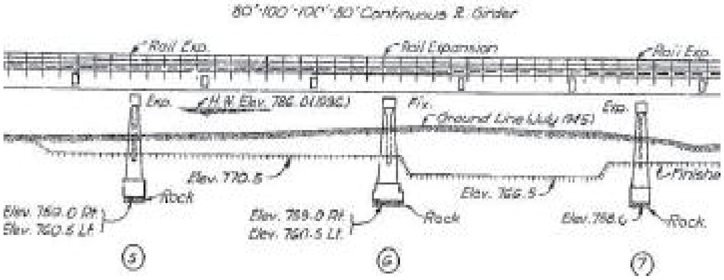

Figure 2.7. Drawing of I-44 Roubidoux Creek Bridge at Bents 5-7.

Once again, the diameter of smart rocks was kept to be *0.368 m*, and $n = 0.041d^{1/6} = 0.0347$. Therefore, the mass density of smart rocks can be determined based on the critical velocity as follows.

$$0.474 \times 1.7 = \frac{0.052^{1/2}\left(\frac{°_s}{1000}-1\right)^{1/2} 0.368^{1/2} 5.70^{1/6}}{0.0347}, \quad °_s = 1022\ kg$$

2.3.6. Final Design of Smart Rocks. The final design of smart rocks not only depends on the hydraulic condition they are subjected to, but also on the intensity of magnetic fields they can generate at a required measurement distance. The field intensity is significantly affected by the size and orientation of the magnets encased in the smart rocks.

2.3.6.1 Size and density. Smart rocks will be deployed in the river around a bridge pier to measure the maximum scour depth or mixed with natural rocks to form a riprap countermeasure and monitor the effectiveness of the riprap protection. The hydraulic condition of a smart rock was taken into account in the estimation of the rock size and density in Section 2.3.5. Due to deployment convenience and standard mold sizes for the concrete casting of round encasements, the diameter of smart rocks was taken to be *0.368 m*. The initial mass density of the smart rocks can then be determined from the local flow velocity and water depth at various bridge sites as discussed in Section 2.3.5. However, due to the uncertainties of estimated hydraulic parameters, the calculated mass density from the critical velocity should be increased by *1.2* or *1.3* times in order to prevent the deployed smart rocks from being washed away, depending on the available hydraulic data at bridge sites.

Specifically, for *Highway 1 Waddell Creek Bridge,* a design factor of *1.2* was considered since a detailed 2D hydraulic model was developed by Caltrans to derive the hydraulic parameters at the bridge site. Therefore, the density of smart rocks should be $1.2 \times 1215 = 1458\ kg/m^3$ based on the evaluation of critical velocity. For all other bridges, a larger design factor of 1.3 was considered due to insufficient information on the local hydraulic data at these sites. Therefore, the density of smart rocks should be $1.3 \times 1117 = 1452 kg/m^3$ for *US63 Gasconade River Bridge,* and $1.3 \times 1022 = 1432\ kg/m^3$ for I-44 *Roubidoux Creek Bridge*. For easy fabrication, the target density of smart rocks was finally taken to be $1495\ kg/m^3$ for a given diameter of *0.368 m*.

2.3.6.2 Internal configuration. The magnetic field of a permanent magnet changes with the orientation of the magnet. For example, the intensity at two poles of the magnet is twice as much as that at its equator. In practical applications, the magnetic field of a smart rock with an embedded magnet is measured from a magnetometer that is stationed either on the river bank or on the bridge deck.

When a magnetometer is set on the river bank, the two poles of a magnet should be aligned with the Earth's magnetic field for maximum sensitivity. Such a smart rock with the magnet was referred to as an APSS as detailed in Figure 2.3. The advantage of the APSS monitored along the river bank is that the measurement station can be located in South or North pole of the magnet, which accelerates the convergence of the APSS localization algorithm with high accuracy. The disadvantage of the APSS is that the direction of the magnet is easy to be affected by strong ferromagnetic substances in the river. To avoid the direction variation by surrounding ferromagnetic substances, the south or north pole of the magnet can be faced to the sky. In this case, however, the measurement for maximum sensitivity is restricted to one side of the magnet, which may reduce the accuracy of rock localization. Besides, during a storm season, river banks are often submerged under water and inaccessible to field tests. Therefore, the APSS is preferred to be studied in open field for smart rock characterization and less desirable for deployment in river or creek for field measurement.

When a magnetometer is set on the bridge deck, the two poles of the magnet should be aligned vertically due to several reasons. First of all, the strongest magnetic field of a magnet can be found at its two poles, which is in good alignment with the vertical sensor of the magnetometer. Secondly, the direction of the magnet is less affected by surrounding ferromagnetic substances, which ensures stable and repeatable measurements over time. Finally, the gravity-oriented direction of the magnet considerably reduces the degree of freedom in the localization algorithm. Furthermore, the south pole of the magnet should be faced up or to the bridge deck for larger intensity of the combined magnetic field of surrounding ferromagnetic substances and the magnet since the three bridges are located in northern hemisphere. In this case, the smart rocks with an APUS are a reasonable choice for field deployment.

Therefore, the final internal configuration of smart rocks for three bridge sites is APUS. Specifically, for Highway 1 over the Waddell Creek and I-44 over the Roubidoux Creek, two stacked N42 magnets (maximum residual flux density: 1.32 Tesla) are configured for practical applications. Figure 2.8 (a) shows the schematic view of an APUS with two stacked N42 magnets. The diameter of inside and outside balls are 25 cm and 28 cm, respectively, to ensure that the inside ball with two magnets placed at the bottom always remains in suspension. For the US63 highway bridge over the Gasconade River, one larger N45 magnet (maximum residual flux density: 1.38 Tesla) with 15.2 cm (6") diameter and 5.1 cm (2") height was selected to generate a stronger magnetic field for practical application. Figure 2.8 (b) illustrates the schematic view of an APUS with one N45 magnet placed at the bottom of the inside ball.

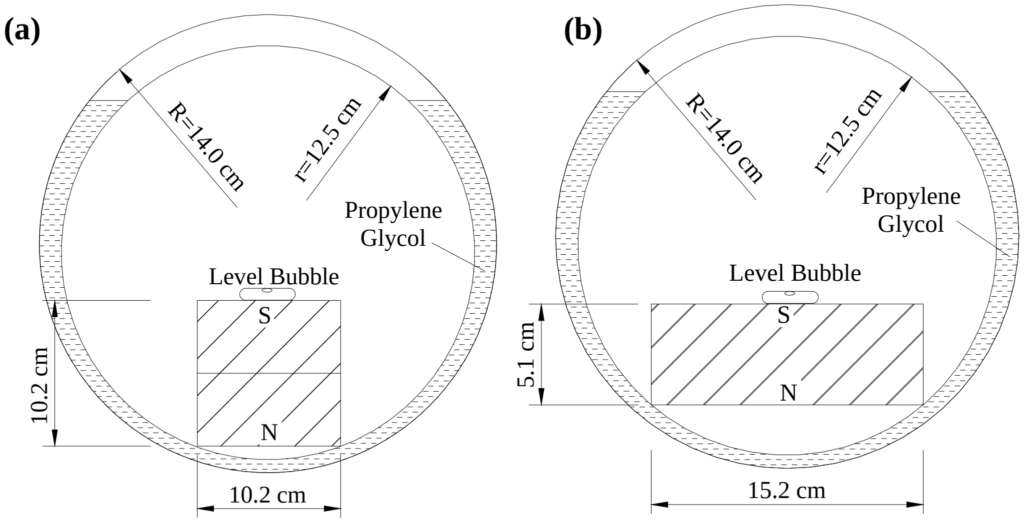

Figure 2.8. Schematic view of an APUS: (a) two stacked N42 magnets and (b) one N45 magnet.

2.3.6.3 Design details. A smart rock with APSS or APUS consists of one or two magnet(s) placed inside an organic glass ball (inside ball), an outside organic glass ball, liquid filled in between the two balls, and a concrete shell encasement. As the type and number of magnet are determined, the determination of the diameter of two balls and the liquid selection are aimed to realize the unique orientation of magnet. The optimum diameter of two balls and liquid can not only realize the unique orientation, but also meet the size and density of a concrete encased smart rock determined from the hydraulic conditions at different bridge sites.

The selection of ball diameter depends upon three factors: commercial availability of casting molds for two halves of a concrete ball, smart rock size, and floating requirement of the inside ball with negligible friction. To ensure that the inside ball can float in the liquid, the average density of the inside ball with the embedded magnet and other components must be slightly less than that of the liquid. For an APSS or APUS with one N42 magnet, an inside ball of 20 cm in diameter was considered. In this case, the mass of the inside ball is equal to the sum of the magnet (*3.06 kg*), organic glass ball and copper beads (total *0.5 kg*), and glue and level indicator (negligible). That is, $\rho_0(\pi)(0.2)^3/6 = 3.06+0.5$ *or* $\rho_0=850\ kg/m^3$, which is less than water density ($1000\ kg/m^3$). Therefore, an inner diameter of 20 cm is a viable choice for the inside ball. The inner diameter of the outside ball can be approximately selected to be *21 cm*, which will leave a sufficient space for lubrication liquid between the inside and outside balls. For an APUS with two N42 magnets or one N45 magnet, the inside ball of *25 cm* is considered as the total mass of the inside ball is *6.82 kg* (*6.12 kg* of two N42 magnets and *0.7 kg* of total weight of glass ball, glue and level indication) and the density of inside ball is $834\ kg/m^3$. The outside ball is selected as *28 cm* for commercial available.

The liquid between the inside and outside balls must be selected such that the inside ball with the magnet can always float without inducing any notable friction force on the inside ball as it rotates inside the outside ball. For a *20 cm* or *25 cm*-diameter inside ball, the liquid density must exceed $850\ kg/m^3$ and $834\ kg/m^3$. Although water is a viable candidate in terms of density and nontoxicity requirements, water does not provide sufficient lubrication between the two balls. Lubrication oil is good for minimum friction but insufficient in mass density of the inside ball floating requirement. Consequently, propylene glycol with a mass density of $1040\ kg/m^3$ is chosen for satisfactory lubrication and nontoxicity requirements.

2.3.7. Fabrication of APSS or APUS. To fabricate an APSS as shown in Figure 2.9 (a), a level indicator with bubble was first attached and glued on one side of a magnet. The opposite side of the magnet was glued to the bottom of half an inside ball with attached copper beads for weight balance. The other half of the inside ball was attached and sealed to complete the inside ball. The complete inside ball was then placed in half of a larger ball, and covered and sealed by the other half to complete the outside ball. Next, a 1-cm-diameter hole was drilled on the outside ball and propylene glycol liquid was injected into the outside ball until the inside ball completely floated and the top of the inside ball was in contact with the outside ball to avoid a large drift of the inside ball. Finally, the injection hole was sealed by a small piece of plastic with adhesives.

For the fabrication of an APUS prototype as shown in Figures 2.9 (b) and 2.9 (c) with two stacked N42 magnets and one N45 magnet, respectively, a high-precision level indicator was glued to the top face (South or North pole) of a magnet. The bottom face (North or South Pole) of the magnet was glued to the bottom of half an inside ball. Adhesives were used as needed to provide unbalanced weights. The remaining fabrication steps for the APUS are the same as those for an APSS.

Figure 2.9. Prototype: (a) APSS with one N42 magnet, (b) APUS with two stacked N42 magnets, and (c) APUS with one N45 magnet.

2.3.8. Effect of deposit resetting on magnetic field. In practice, a scour hole is created due to deposit erosion but may be refilled over time. The smart rocks rolling down to the bottom of the scour hole may be covered by the refilling deposits. Whether deposit resetting affects the measurement of magnetic fields was investigated at the Gasconade River Bridge site.

As shown in Figure 2.10, a 1-m deep hole was excavated approximately 10 m away from a bridge pier. A magnet was first wrapped with a plastic bag that was tied with a rope, and then placed into the bottom of the hole. The rope was used to pull the magnet out of the refilled hole after the test was over. The two sensors (F1 and F2) of a magnetometer were fixed on the top of two wood poles that were inserted into the ground on two sides of the hole. The magnetometer was set in between the two sensors. Another wood pole was placed next to the magnet with marks in *0.5 m* interval up to *1.5 m* to measure the height of the refilling deposits. As indicated in Figure 2.11, the measurements were first taken with no deposits, then with the excavated soils refilled to the *0.5 m* and *1.0 m* marks, and finally with additional deposits piled up to *1.5 m*.

Table 2.2 lists the measured intensity of magnet's and ambient magnetic fields. It can be seen from Table 2.2 that the maximum variation of the intensities measured for deposits refilled to various heights is *0 nT* and *10 nT* at F1 and F2, respectively. These variations are significantly less than *100 nT*, the level of intensity change that begins to influence the localization accuracy of the magnet. These variations may be caused by the change in Earth's magnetic field at different times of measurement or by other disturbances on the sensor head in the process of deposits refilling.

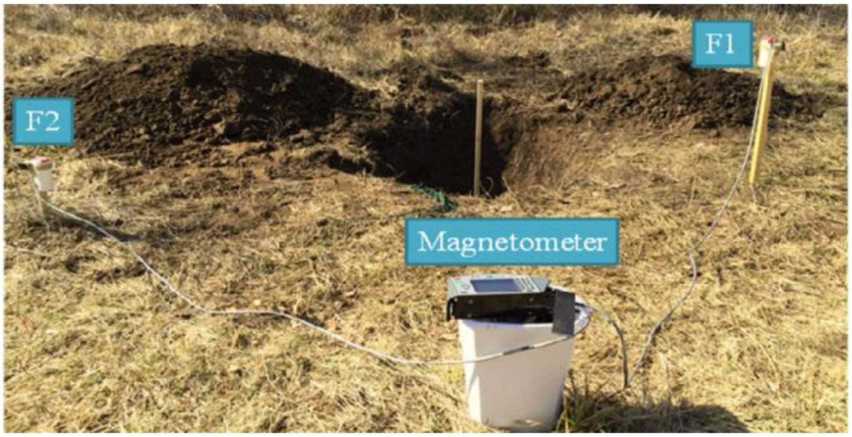

Figure 2.10. Overall arrangement of resetting tests.

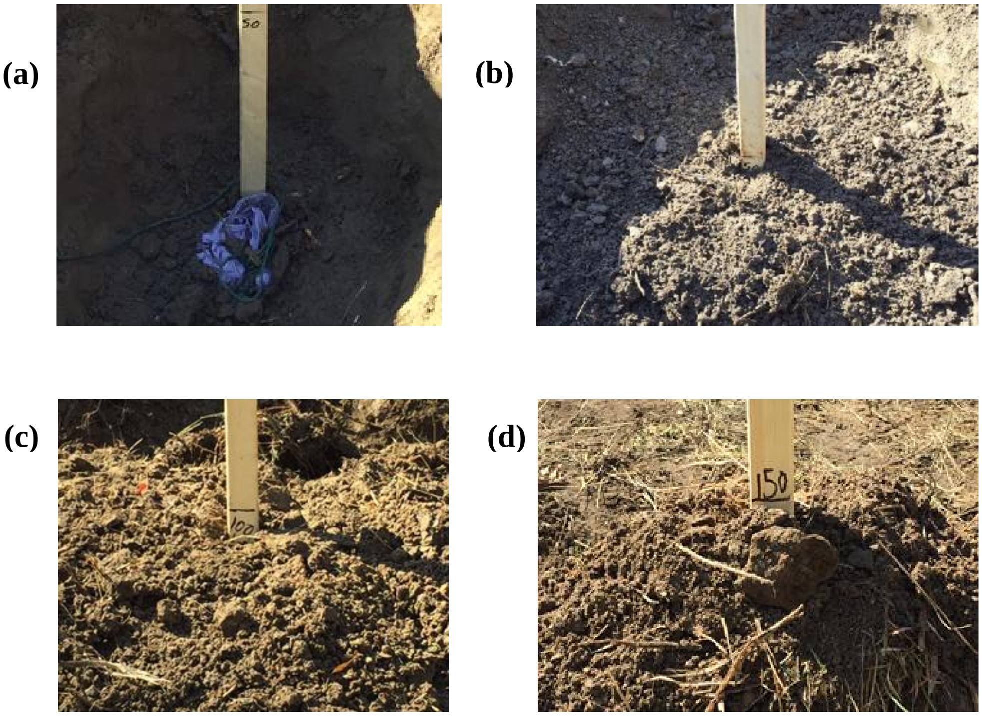

Figure 2.11. Deposits refilled to various heights: (a) 0.0 m, (b) 0.5 m, (c) 1.0 m, and (d) 1.5 m.

Table 2.2. Intensity at various deposit heights

Deposit Height (m)	Intensity (10^4 nT)	
	F1	F2
0.0	5.087	5.073
0.5	5.087	5.073
1.0	5.087	5.072
1.5	5.087	5.072

2.3.9. Effect of steel reinforcement on smart rock operation. An attempt was made to keep the two poles of a magnet aligned vertically during measurements so that the magnet orientation is known *in prior* and the localization of the magnet becomes simplified. One concern to this effort in practical applications is the potential influence of the ferromagnetic substances in bridge piers or abutments. Therefore, a simple field test was carried out to rule out this possibility.

Figures 2.12 and 2.13 show the APUS prototype placed next to a bridge pier and on the bridge footing, respectively. It can be seen from Figures 2.12 and 2.13 that the bubble slightly deviated from the center of a high-precision level, indicating an inclination angle of less than 0.5° and thus little effect on the localization of the APUS. It was verified during the field tests that the bubble remained in the center of a high-precision level attached on the APUS when placed at least 10 m away from the bridge pier and footing.

Figure 2.12. The APUS prototype placed next to a bridge pier.

Figure 2.13. The APUS prototype placed on a bridge footing.

2.3.10. Concrete encasement of smart rocks. For field deployment at bridge sites, each APUS smart rock was cast in a spherical concrete encasement. The smart rock with concrete encasement as schematically shown in Figure 2.14 was cast in a 36.8 cm-diameter mold. The total density of the smart rock is ρ_s = [(0.28^3 m^3) (850 kg/m^3) + (0.368^3 m^3-0.28^3 m^3)(2000 kg/m^3)] / 0.368^3 or ρ_s =1495 kg/m^3, which is appropriate for all three bridge sites.

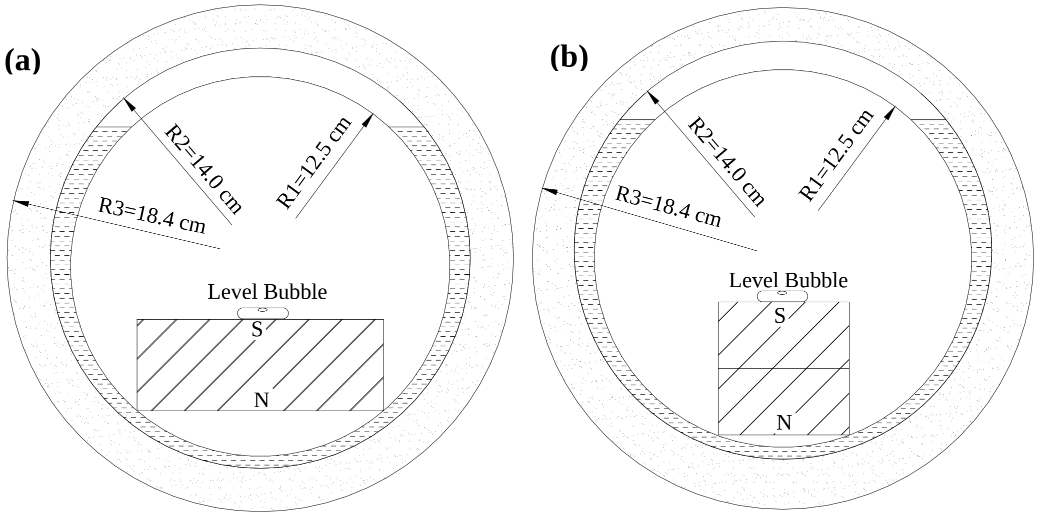

Figure 2.14. Schematic view of concrete encasement: (a) APUS with one N45 magnet, and (b) APUS with two stacked N42 magnets.

The mix proportion of concrete was selected to be: water = 288 kg/m^3, cement= 640 kg/m^3, sand (diameter = 4.75 mm) = 1023 kg/m^3, fiber = 2 kg/m^3 and water reducer admixture = 8 kg/m^3. The concrete fiber (FORTA ULTRA-NET) was made of virgin homopolymer polypropylene and came in a collated fibrillated twisted bundle, which is often used to reduce plastic and hardened concrete shrinkage, improve impact strength, and increase fatigue resistance and concrete toughness. A rope across the outside ball and concrete encasement was tied around the stiffener of two halves of the outside ball and used to pull the smart rock into its final position during field deployment and mark the rock location after the deployment. The four-step fabrication process of concrete encasement is shown in Figure 2.15: 1) preparing fiber reinforced concrete; 2) pouring a small amount of concrete into the bottom half of a plastic mold, placing and pushing an APUS into the concrete, and covering the APUS with the top half of the mold; 3) filling the mold with concrete while tapping the mold with a hammer to remove potential air bubbles; and 4) removing the mold once concrete is set in one day and putting the smart rock under water to cure for 14 days.

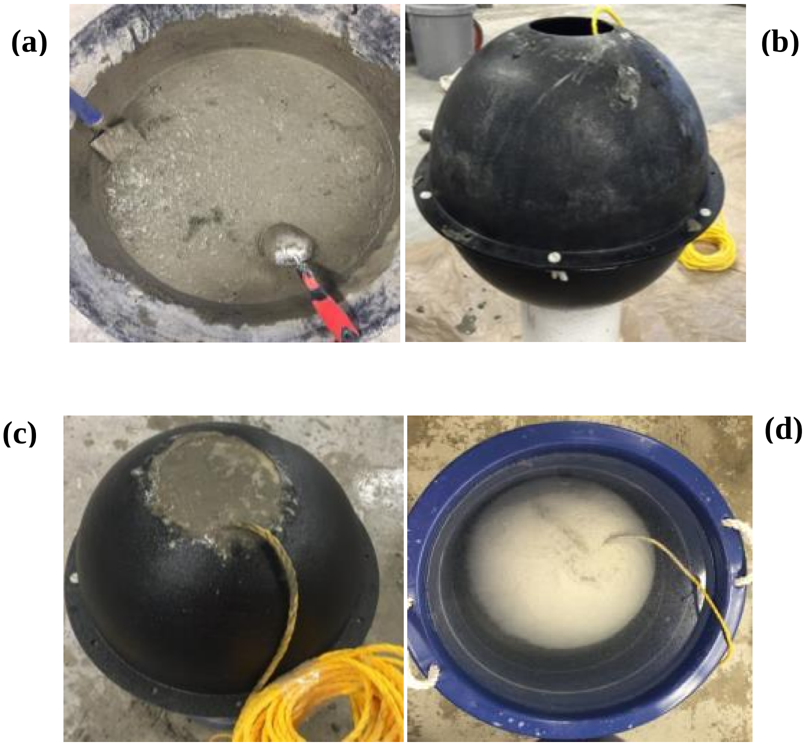

Figure 2.15. Four-step fabrication of concrete encasement: (1) preparing fiber reinforced concrete, (b) placing an APUS into concrete and mold, (c) filling the mold with concrete, and (d) curing the concrete encasement in water for 14 Days.

2.4. SUMMARY

In this section, the working principle of the smart rock technology was introduced for the monitoring of maximum scour depth and riprap effectiveness. Three types of smart rocks (AOS, APSS, and APUS) were proposed, designed, and prototyped. The design guidelines of smart rocks were developed. The equation for critical flow velocity in HEC18 was mainly used to establish the relationship between the size and density of smart rocks based on their incipient motion. The equation was applied into three bridge sites in the states of California and Missouri. The size of smart rocks was first determined to meet the requirements for fabrication and measurement. The density of smart rocks was calculated from their incipient motion.

The effect of resetting deposits on the magnetic field near the Gasconade River Bridge site was tested. To this end, a hole was excavated near a bridge pier, a magnet was placed at the bottom of the hole and covered by deposits to various heights, and the intensity of the magnetic field of the magnet and other ferromagnetic substances were measured at two fixed locations. As expected, the resetting deposits had little effect on the magnetic field measurement. In addition, whether steel reinforcement in a bridge pier would affect the magnetic measurement was investigated. Based on the field tests, no obvious change was observed in the orientation of a magnet when placed near a bridge pier with steel reinforcement.

The final design of smart rocks was a sphere of 0.368 m in diameter and 1495 kg/m^3 in density, which was determined by multiplying a design factor by the density calculated from the analysis of incipient motion. The design factor was introduced to take into account the uncertainties about the hydraulic parameters and the empirical equation for critical velocity. A factor of 1.2 was considered for bridge sites with detailed hydraulic analysis and 1.3 for bridge sites with no hydraulic analysis. A gravity-oriented magnet was embedded inside each smart rock so that the pole direction of the magnet would be known *in priori* and remained vertical during measurements. When the sensors of a magnetometer are placed vertically, the gravity-oriented magnet also results in the most sensitive range of measurement. The designed smart rocks were then prototyped as a concrete encasement in applications.

3. LOCALIZATION OF A SINGLE SMART ROCK IN UNIFORM AMBIENT MAGNETIC FIELD

3.1. INTRODUCTION

Tracing a magnet from its magnetic field has been widely used in medical science to differentiate human bodies [85]. A tiny magnet simplified as a dipole with non-invasive and non-wire power is employed to generate the magnetic strength around a human body. The dipole can be positioned by an inverse calculation of a mathematic function, thus leading to the change of the human body through continuous monitoring. Similarly, a permanent magnet as the core of a smart rock would be simplified as a dipole to establish a mathematical relationship between the magnetic field and the position of the magnet. A single smart rock placed in a uniform ambient magnetic field (due to the Earth only) is localized in order to determine the movement of the rock in scour monitoring application. Two types of smart rock prototypes, Arbitrarily Oriented System (AOS) and Automatically Pointing to South System (APSS) developed in Section 2, are considered as models of the smart rocks. The localization mechanism for AOS and APSS is introduced and analyzed by measuring the ambient magnetic field of the Earth and a combined magnetic field of the Earth and the smart rock. The magnetic field parameters of the magnet and the Earth are first evaluated by an approach proposed in this section. The proposed approach and the localization algorithm are then validated at an open site experimentally for two types of smart rocks with AOS and APSS, respectively. Finally, an application example is conducted using an APSS to simulate the movement of the smart rock in practical application.

3.2. THE MAGNETIC FIELD OF A PERMANENT MAGNET

The magnetic field of a permanent magnet can be numerically solved using an equivalent magnetic charge method [86], an Amperian current method [87] and the finite element method. The equivalent charge and current methods are used to derive the analytical solution of permanent magnets in simple shape while the finite element method is used to address the integral or differential equation expressed for permanent magnets with intricate shapes. Also known as the scalar magnetic potential method in engineering applications, the equivalent charge method employs the key concept of an imaginary magnetic charger and its surface density. The magnetic field of a permanent magnet is then calculated by superimposing the magnetic fields generated by all magnetic chargers. The Amperian current method, also referred to as the magnetic vector potential method, deals with the circular electric current with a certain density that exists in a permanent magnet. Specifically, the inner circular electric current is canceled out for a uniform magnetization of the magnet. However, a certain surface current density still exists in the boundary of the magnet. For example, the uniformly magnetized cylinder magnet has the cylindrical surface current that is equal to the circular current loops uniformly distributed along the cylinder length. Thus, the magnetic field generated in space from a magnet can be computed by integrating the magnetic field produced from each circular electric current. These two equivalent models involve differential equations derived from the Maxwell's equations with scalar magnetic potential and magnetic vector potential, respectively. Numerical approaches are then adopted to solve the differential equations for the magnetic field in space.

In this section, a cylindrical or disc permanent magnet is considered. The Amperian current model is employed to represent and calculate the magnetic field of the cylindrical magnet since it is easier than the magnetic charge model in terms of numerical calculation. An idealized solenoid with strictly azimuthal current in a thin sheet wrapped around a right circular cylinder [88] can serve as a better model of a permanent cylindrical magnet, provided that its magnetization is sufficiently uniform/homogeneous. The ideal solenoid was treated as a stack of loops to calculate its magnetic field by a straightforward integration of circular current loop that is analytically expressed in elliptic integrals [88]. The exact solution of the solenoid was developed in a simple and efficient way with a single function and a generalized complete elliptic integral. In terms of computation, the simplified point dipole model of an ideal solenoid with finite length is quite simple and fast [88]. The simplified model is valid when the distance between a point of interest and the solenoid significantly exceeds the size of the solenoid or the permanent magnet.

The localization of a permanent magnet is an inverse problem from the measured magnetic field to the source magnet [89]. The magnetic field signals generated by the magnetic dipole can be measured by magnetometers at various spatial points around the object including the dipole. The positions of these spatial points can also be surveyed. The localization parameters such as positions and orientation of the dipole can be computed by solving a high-order nonlinear function with an appropriate optimization algorithm [90-92]. The non-linear optimization algorithms, such as Powell's [93], Newton's method [91], Levenberg-Marquardt (LM) [89, 92-96], genetic algorithm [97], and particle swarm optimizer [97, 98], the linear optimization algorithm [99], the combined nonlinear (LM) and linear algorithm [100], and the Random Complex Algorithm (RCA) [101] were investigated, each having its advantages and shortcomings. In this study, a magnetic dipole was also used as the simplification of a cylindrical magnet since the measurement points are far away from the magnet.

3.2.1. Mathematic Expression for a Cylindrical Magnet. Consider a disc/cylinder magnet of 2a in diameter and 2b in length in a local cylindrical coordinate system as shown in Figure 3.1. Here, the origin of the coordinate system is located at the centroid of the magnet, *y* axis represents the magnetized direction from South Pole to North Pole inside the magnet, and *ρ* axis represents the radial direction perpendicular to the *y* axis.

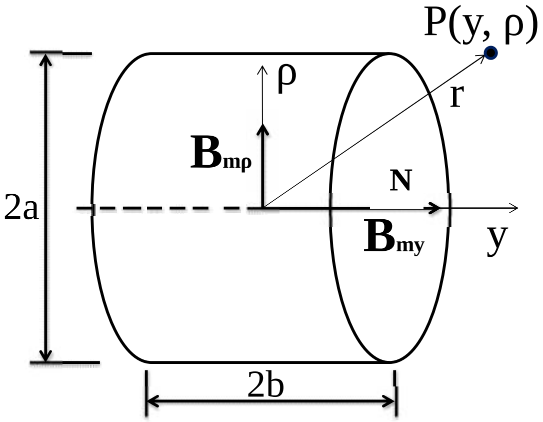

Figure 3.1. A cylinder magnet in a local cylindrical coordinate system.

The magnetic field induced by the magnet is axis-symmetric about the centerline of the magnet. It can be represented by a vector $\mathbf{B}_m$ (y, ρ) at any point P. The magnetic field vector can be decomposed into a longitudinal component $\mathbf{B}_{my}$ and a radial component $\mathbf{B}_{m\rho}$. When the radial coordinate ρ at Point P is significantly larger than the radius *a* of the magnet or the longitudinal coordinate *y* is significantly larger than half of the magnet length *b*, the magnitudes B_{my} and $B_{m\rho}$ of two components of the magnetic field vector can be approximated by [88]:

$$\begin{cases} B_{my}(y, \circ) = k\,\dfrac{(2y^2 - \circ^2)}{r^5} \\ B_{m\circ}(y, \circ) = k\,\dfrac{3\circ\, y}{r^5} \end{cases} \tag{3.1a}$$

$$B_m(y, \circ) = \sqrt{B_{my}^2(y, \circ) + B_{m\circ}^2(y, \circ)} \tag{3.1b}$$

where $k = «_0« / 4®$ is a coefficient related to the strength of the magnet, μ_0 is the permeability of vacuum in *T·m/A*, and μ is the magnetic moment of the magnet. These parameters are either obtained from the manufacturers (e.g. technical specification of permanent magnets) or evaluated by the calibration test developed in this study.

3.2.2. Mathematic Expression in Global Cartesian Coordinate System.

As shown in Figure. 3.2, the local Cartesian coordinate system (*p*-xyz) is originated at the center of the cylindrical magnet and fixed to the magnet. The y axis is along the thickness direction from South to North Pole of the magnet. Since it moves together with the magnet, the local coordinate system cannot be used to define the position of the magnet. Therefore, a global Cartesian coordinate system O-XYZ is introduced and fixed in space. Determined by a compass, Y-axis points to the North Pole of the Earth's magnetic field that has a declination angle with the geographical South Pole. Then, X-axis is perpendicular to Y-axis and has the declination angle with the geographic west and Z-axis is determined according to the right-hand rule as vertically upward. For convenience, the Y-axis is simply referred to the geographical south and labeled as Y (South), and the X-axis to the geographical west and labeled as X (West) as shown in Figure 3.2. The center of the magnet is designated as Point *P* (X_M, Y_M, Z_M) at global coordinates (X_M, Y_M, Z_M) and as Point *p* (*0, 0, 0*) at local coordinates (*0, 0, 0*). An arbitrary point in space is designated as Point *q* (x_i, y_i, z_i) in the local coordinate system and Point Q_i (X_i, Y_i, Z_i) in the global coordinate system. The magnetic field expressed in Eq. (3.1) in the local coordinate system must be translated to the global coordinate system in order to be combined with the magnetic fields generated by other sources.

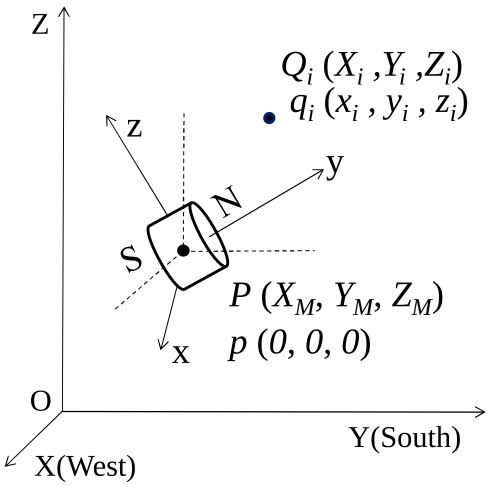

Figure 3.2. Global versus local Cartesian coordinate systems.

In the local coordinate system (*p*-xyz) as shown in Figure 3.2, the magnetic field intensity vector at an arbitrary point $q(x_i, y_i, z_i)$ can be written as $\boldsymbol{B_i}=(B_{xi}, B_{yi}, B_{zi})$. The two components of the magnetic field generated by a magnet are given in Eq. (3.1). The radial component can be further decomposed into x- and z-components. The x-, y- and z-components of the magnetic flux at point *q* in the p-xyz coordinate system can then be expressed into:

$$\begin{cases} B_{xi} = k\dfrac{3x_i y_i}{r^5} \\ B_{yi} = k\dfrac{2y_i^{\,2} - x_i^{\,2} - z_i^{\,2}}{r^5} \\ B_{zi} = k\dfrac{3z_i y_i}{r^5} \end{cases} \tag{3.2a}$$

$$r = \sqrt{x_i^2 + y_i^2 + z_i^2} \tag{3.2b}$$

$$B = \sqrt{B_{xi}^2 + B_{yi}^2 + B_{zi}^2} \tag{3.2c}$$

In order to transfer the magnetic field components from the local coordinate to the global coordinate, the global coordinate system must be first rotated at its origin to become parallel to the local coordinate system and then moved translationally to the local coordinate system. First, consider three Euler angles, $\alpha\in[0,2\pi]$, $\beta\in[0,2\pi]$, and $\gamma\in[0,2\pi]$ about X-, Y-, and Z-axis following the right-hand rule. A rotation matrix from the XYZ coordinate system to the xyz coordinate system can be expressed into:

$$\mathbf{R}=\begin{bmatrix} \cos\quad \cos\yen & \cos\quad \sin\yen & -\sin \\ \sin\sim\sin\quad \cos\yen-\cos\sim\sin\yen & \sin\sim\sin\quad \sin\yen+\cos\sim\cos\yen & \sin\sim\cos \\ \cos\sim\sin\quad \cos\yen+\sin\sim\sin\yen & \cos\sim\sin\quad \sin\yen-\sin\sim\cos\yen & \cos\sim\cos \end{bmatrix} \tag{3.3}$$

Then, consider (X_M, Y_M, Z_M) as the global coordinate of the origin of the local coordinate system. After translational movement from the global to local coordinate system, the local coordinate at Point Q_i can be derived as:

$$\begin{pmatrix} x_i \\ y_i \\ z_i \end{pmatrix}=\mathbf{R}\cdot\begin{pmatrix} X_i-X_M \\ Y_i-Y_M \\ Z_i-Z_M \end{pmatrix} \tag{3.4}$$

According to the vector rotation transformation **R** in Eq. (3.3), the magnetic field intensity at any point Q_i (X_i, Y_i, Z_i) around the magnetic dipole can be written as $\boldsymbol{B_i}=(B_{Xi}, B_{Yi}, B_{Zi})$ in the global coordinate system and can be related to that in the local coordinate system by:

$$\begin{pmatrix} B_{Xi} \\ B_{Yi} \\ B_{Zi} \end{pmatrix}=\mathbf{R}^{-1}\begin{pmatrix} B_{xi} \\ B_{yi} \\ B_{zi} \end{pmatrix}=\mathbf{R}^{-1}\begin{pmatrix} k\dfrac{3x_iy_i}{r^5} \\ k\dfrac{2y_i^{\,2}-x_i^{\,2}-z_i^{\,2}}{r^5} \\ k\dfrac{3z_iy_i}{r^5} \end{pmatrix} \tag{3.5a}$$

$$r=\sqrt{x_i^2+y_i^2+z_i^2} \tag{3.5b}$$

$$B_i=\sqrt{B_{Xi}^2+B_{Yi}^2+B_{Zi}^2} \tag{3.5c}$$

By substituting Eqs. (3.3) and (3.4) into Eq. 3.5, the three components (B_{Xi}, B_{Yi}, B_{Zi}) of the magnetic field at an arbitrary point can be completely represented by its relative position to the magnet in the global coordinate system. In general, six parameters are required to define the location of a magnet: position (X_M, Y_M, Z_M) and orientation that is represented by a unit vector of y-axis in the global coordinate system, $\mathbf{n}_y = (l, m, n)^T$. Since the flux intensity is invariant to a rotation of the magnet about y-axis, the orientation of the magnet can be uniquely determined by the unit vector of y-axis. Considering the constraint on the directional cosines of any unit vector, $l^2 + m^2 + n^2 = 1$, only five unknowns are required to be determined for magnet localization in theory. In practice, however, the magnetic field generated from the magnet is to be combined with those from other sources that are not axis-symmetric, the axis-symmetric property of the magnet is not considered in the following derivation.

As indicated in Eq. (3.5a), when left multiplied by $\mathbf{R}^{-1}$, a unit vector of y-axis in the local coordinate system, $(0, 1, 0)^T$, becomes the y-axis in the global coordinate system, represented by $(l, m, n)^T$. Therefore, the second column of $\mathbf{R}^{-1}$ (corresponding to the second row of the rotation matrix $\mathbf{R}$ since $\mathbf{R}^{-1}=\mathbf{R}^{T}$) is equal to the orientation vector $(l, m, n)^T$. That is, $l = \sin \alpha \sin \beta \cos \gamma - \cos \alpha \sin \gamma$, $m = \sin \alpha \sin \beta \sin \gamma + \cos \alpha \cos \gamma$, and $n = \sin \alpha \cos \beta$. Therefore, solving for the directional cosines l, m, and n is equivalent to solving for the Euler angels α, β, and γ.

3.3. LOCALIZATION PRINCIPLE

The scalar magnetometer G858 used in the early part of this study measures a total intensity of the magnetic fields of the Earth, the magnet, and nearby ferromagnetic substances. At any point, the magnitude and direction of a geomagnetic vector can be determined according to its longitude and latitude. The magnitude B_E can be measured from the magnetometer G858. The direction is described by a dip angle θ of the Earth's magnetic field lines with a horizontal plane and the hemisphere in which the investigated site is located. The dip angle can be either evaluated by inputting the longitude and latitude of a certain point to the software provided together with the magnetometer, or computed using the approach developed in this study. When the nearby substances are neglected at an open site and the Earth's magnetic field is assumed to be unchanged over time and in a small space of interest, the total magnetic field intensity $B_{//i}$ depends upon the Earth's magnetic field intensity B_E, the dip angle θ, and the coefficient k of the magnet in addition to the coordinates $(X_M, Y_M, Z_M, \alpha, \beta, \gamma)$. That is, $B_{//i} = B_{//i}(B_E, \theta, k, X_M, Y_M, Z_M, \alpha, \beta, \gamma)$.

3.3.1. Localization of AOS. As shown in Figure 3.3, the geomagnetic field vector, $\boldsymbol{B_E}$, is parallel to the YOZ plane in the XYZ Cartesian coordinate system. Its direction depends on whether the investigated site is located in north or south hemisphere of the Earth. Since the project (bridge) sites in this study are located in North America, the geomagnetic field vector approximately points to the geographical North and faces to the ground with a corresponding dip angle of the field site. Therefore, the Earth's magnetic field vector is $\boldsymbol{B_E} = (0, -B_E \cos\theta, -B_E \sin\theta)^T$ in the global coordinate system. The total magnetic field intensity vector, $B_{//i}$, at an arbitrary point Q_i can then be expressed into:

$$B_{//i} = \sqrt{(B_{Xi})^2 + \left[B_{Yi} + (-B_E \cos\theta)\right]^2 + \left[B_{Zi} + (-B_E \sin\theta)\right]^2} \qquad (3.6)$$

Note that, the magnitude of $\boldsymbol{B_E}$ is measured by means of the magnetometer prior to the deployment of the magnet at a project site. Given the coefficients k and θ and the Earth's magnetic intensity B_E for the project site, the total magnetic intensity of the Earth and a magnet, $B_{//i}$, at any point Q_i (X_i, Y_i, Z_i) is a function of (X_M, Y_M, Z_M) and (α, β, γ) only. To determine the location and orientation (6 parameters) of a magnet, measurements must be taken at a minimum of six stations in practical applications.

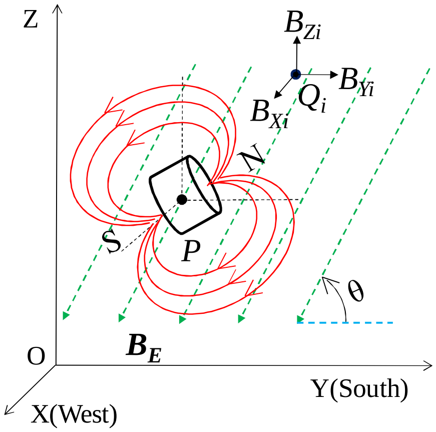

Figure 3.3. The magnetic field of an AOS.

Eq. (3.6) is a high-order nonlinear function of the 6 location and orientation parameters of a magnet. To solve for the parameters (X_M, Y_M, Z_M, α, β, γ), a nonlinear optimization algorithm is developed based on an objective error function that represents the difference between the predicted and measured magnetic field intensities. Let a N number of measurements, $B_{//i}^{(M)}$ ($i=1, 2, \ldots, n$), be taken at n stations Q_i (X_i, Y_i, Z_i) ($i=1, 2, \ldots, n$). At each station, the theoretically predicted intensity $B_{//i}^{(P)} = B_{//i}$ can be calculated from Eqs. (3.4) - (3.6). Therefore, the square-root-of-the-sum-of-the-squared (SRSS) error between the calculated intensity $B_{//i}^{(P)}$ and the measured intensity $B_{//i}^{(M)}$, $J(X_M, Y_M, Z_M, \alpha, \beta, \gamma)$, can be evaluated by:

$$J(X_M, Y_M, Z_M, \sim, \quad, ¥) = \sqrt{\sum_{i=1}^{n}[B_i^{(P)} - B_i^{(M)}]^2} \tag{3.7}$$

The objective error *J* is minimized to solve for the unknown location and orientation of the magnet embedded in a smart rock. Specifically, six equations will be formulated by taking the derivative of *J* with respect to any one of the six unknown parameters. Multiple solutions may be obtained from the high-order nonlinear equations due to unknown orientations. Engineering judgment must be exercised to select an appropriate solution in practical application based on the previous location and orientation of the magnet. Therefore, AOS is not an ideal candidate for the development of smart rocks in practical applications.

3.3.2. Localization of APSS. In an APSS, the y-axis from S to N pole points to the opposite direction of the South. Therefore, $\alpha = \pi$, $\beta = 0$, and $\gamma = 0$. Figure 3.4 shows an APSS located at Point *P* in the global coordinate system XYZ. The total magnetic field intensity $B_{//i}$ as shown in Eq. (3.6) at an arbitrary point Q_i is significantly simplified into a function of X_M, Y_M, and Z_M given the Earth's magnetic field intensity B_E, the dip angle θ, and the coefficient *k* of the magnet. By substituting the rotation matrix in Eq. (3.3) and the relation in Eq. (3.4) into Eq. (3.5), the three components (B_{Xi}, B_{Yi}, B_{Zi}) in Eq. (3.6) can be expressed into:

$$\begin{pmatrix} B_{Xi} \\ B_{Yi} \\ B_{Zi} \end{pmatrix} = \begin{pmatrix} -k\dfrac{3(X_i - X_M)(Y_i - Y_M)}{\left(\sqrt{(X_i - X_M)^2 + (Y_i - Y_M)^2 + (Z_i - Z_M)^2}\right)^5} \\ -k\dfrac{2(Y_i - Y_M)^2 - (X_i - X_M)^2 - (Z_i - Z_M)^2}{\left(\sqrt{(X_i - X_M)^2 + (Y_i - Y_M)^2 + (Z_i - Z_M)^2}\right)^5} \\ -k\dfrac{3(Z_i - Z_M)(Y_i - Y_M)}{\left(\sqrt{(X_i - X_M)^2 + (Y_i - Y_M)^2 + (Z_i - Z_M)^2}\right)^5} \end{pmatrix} \tag{3.8}$$

The total magnetic field intensity $B_{//i}$ for an APSS is then obtained by substituting Eq. (3.8) into Eq. (3.6). The SRSS error in Eq. (3.7) is also reduced into *J* (X_M, Y_M, Z_M) in which $B_{//i}^{(P)} = B_{//i}$ can be evaluated by Eq. (3.6). As such, only three unknown parameters must be solved for localization of the magnet.

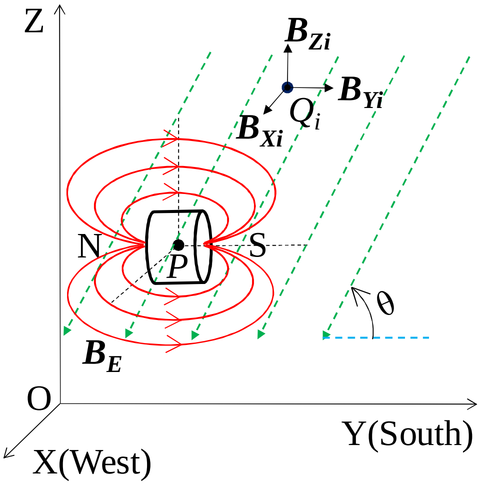

Figure 3.4. The magnetic field of an APSS.

For both AOS and APSS, the sequential quadratic programming (SQP) algorithm [102] was used to iteratively find the optimization solution for the position of the magnet from the high-order nonlinear equation sets. The algorithm was implemented in MATLAB through the use of Fmincon code for non-linearly constrained optimization problems. It has been proven to be among the most effective general algorithm currently available.

3.4. DETERMINATION OF THE MAGNET LOCATION IN OPEN FIELD

A field test was firstly carried out in an open field with parallel magnetic lines of the Earth magnetic field located in the Ber Juan Park, Rolla, MO to validate the feasibility of the magnet localization algorithm.

3.4.1. Experimental Layout. The test layout is shown in Figure 3.5(a). The APSS or AOS was located at the origin of the Cartesian Coordinate O-XYZ as shown in Figure 3.5 (b). To locate APSS or AOS, a sensor head of G858 Magnetometer [103] was separately stationed at Q_1, Q_2, Q_3 …, Q_{25}, Q_{26} and Q_{27} as shown schematically in Figure 3.5 (c). The selection of the 27 points for the measurements of the total magnetic intensity and X-, Y-, Z- coordinate considered the influence of the inclination angle and distance on the intensity. Specifically, the measurement points were selected with a radial distance of 1.5 m and 5 m from the magnet. In addition, the wooden poles with various heights from 0.2 m to 1.0 m with an increment of 0.1 m were used to taking into account the impact of the inclination angle. A total station was set up at a far distance to survey the coordinates of APSS, AOS and 27 sensor positions with a prism placed on top of each wooden pole. The coordinates surveyed from the total station were then transferred to the coordinate system O-XYZ as shown in Figure. 3.5 (c).

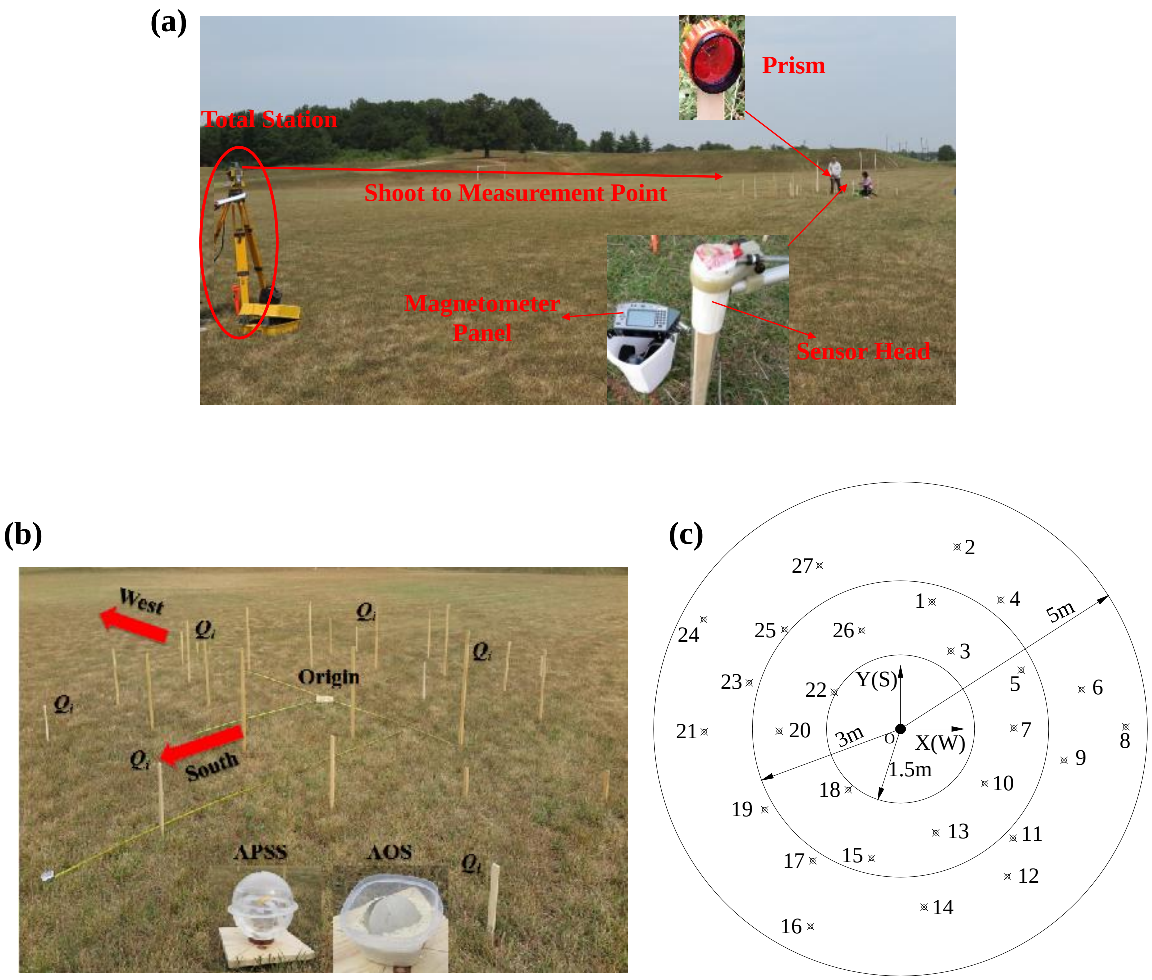

Figure 3.5. Field tests in Ber Juan Park, Rolla, MO: (a) test setup and layout, (b) layout of sensor and magnet, and (c) schematic view of measurement points.

3.4.2. The Earth Magnetic Field Intensity B_E and Coefficients k and θ. The Earth's magnetic field intensity, B_E, changes from one place to another and the coefficient of the magnet may change slowly over time. Therefore, k and θ must be evaluated for a specific study. The Earth's magnetic field lines are considered to be parallel at the test site without any ferromagnetic structures. Considering the geographical location in Rolla, MO, with latitude and longitude coordinates being 37°57′12″N and

91°45′27″W, respectively, and a magnet pointing due geographical south of the Earth, Figure 3.4 illustrates the XYZ coordinate system and the relative directions of the magnetic fields of the Earth and the magnet.

3.4.2.1 Earth's magnetic field intensity B_E. The magnetic field intensity of the Earth was first evaluated with a series of field tests. To this end, the open field was selected to avoid the potential effect of electric lines, train tracks, and other ferromagnetic substances. During the tests, mobile phones and magnets were taken far away from the magnetometer sensor heads. Based on 15 measurements, the average Earth’s field intensity at the field test site was found to be 52342 Nano Tesla (or nT) with a standard deviation of 0.23 nT.

3.4.2.2 Coefficient *k* and *θ*. The coefficient k and the inclination angle θ are related by Eq. (3.6) when the predicted total magnetic field intensity $B_{//i}$ is equal to the measured intensity at each measurement point. A trial-and-error method was used to determine the k and θ in three steps from n sets of calibration test data collected at the test site, each including the total magnetic field intensity as a function of the XYZ coordinates. In Step 1, k is assumed to vary from 36000 to 48000 with a step size of 50 based on manufacturers’ data for various magnets. For each k value, θ_i ($i=1, 2,\ldots,$ *or* n) was calculated with a set of the test data (intensity and coordinate) from the equality of the predicted and the measured intensities. In Step 2, the n numbers of θ_i were used to determine the unbiased mean and standard deviation:

$$\overline{\overline{\ }} = \frac{1}{n}\sum_{i=1}^{n}\overline{\ }_{i} \qquad\qquad \pm = \sqrt{\frac{\sum_{i=1}^{n}(\overline{\ }_{i} - \overline{\overline{\ }})^{2}}{n-1}} \tag{3.9}$$

In Step 3, the k value corresponding to the minimum standard deviation and its corresponding average $\overline{\overline{\ }}$ value is determined. They contributed to the least-squared error in comparison with the measured data as specified in Eq. (3.7).

A calibration test was conducted to determine the k and θ at the same test site with the Cartesian Coordinate System O-XYZ defined as Y in South direction, X in West direction and Z in vertically upward direction as shown in Figure 3.6 (a, b). The APSS and AOS were adopted to calibrate the magnet coefficient and the dip angle of the Earth. They were placed separately at the origin to generate the magnetic field around them. A total of 21 points, labeled as N1, N2, …, and N21 on the top of wood poles of various heights, were selected in the distance range of 1.3 m to 3.0 m along the Y-axis. The total station as shown in Figure 3.5 (a) was employed to survey the 21 calibration points. The AOS was achieved by placing a magnet in half a plastic ball that floated on water in a bucket as shown in Figure 3.6 (a). A high-precision level with an accuracy of 0.025^{o} was placed on top of the AOS to keep the axis of the magnet in horizontal plane by weight balance.

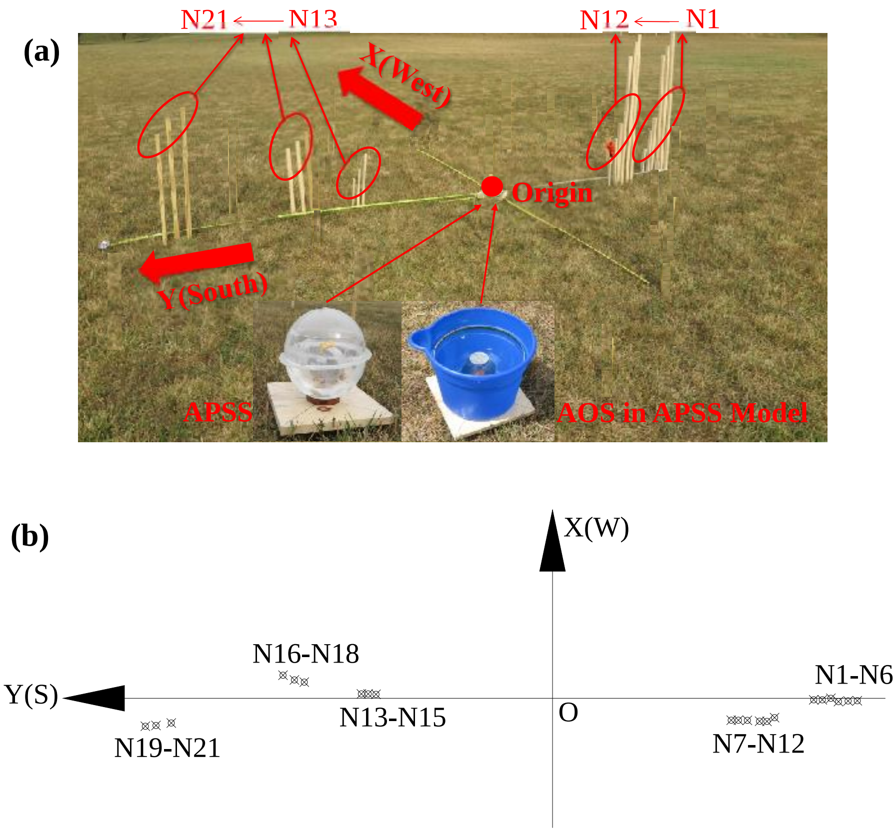

Figure 3.6. Calibration test: (a) experimental setup and (b) relative locations of the magnet and measurement points in horizontal plane.

Based on a preliminary sensitivity analysis in MATLAB, 8 out of the 21 data sets from the APSS and AOS, as listed in Table 3.1, were chosen to evaluate the k and θ. Note that M_{APSS} and M_{AOS} in Table 3.1 represent the magnets in the APSS and AOS. The first four points were located on the plus Y-axis side and the remaining four on the minus Y-axis side. In the case of the APSS, eight inclination angles were related each coefficient k

as shown in Figure 3.7 (a) using the trial-and-error method. Their corresponding unbiased standard deviation σ is presented in Figure 3.7 (b). It can be seen from Figure 3.7 that the standard deviation is a minimum when the eight θ values are nearly equal. Specifically, the eight θ values are *67.3º*, *67.9º*, *67.8º*, *68.0º*, *67.5º*, *67.3º*, *68.1º*, and *67.6º* when k = 42542 nT·m^3. The mean and standard deviation of θ values are 67.7º and 0.34º, respectively. The coefficient of variation of θ is *0.340°/67.7° = 0.42%*.

Table 3.1. Coordinates and total magnetic field intensities at selected points

	APSS					AOS			
	X_i (m)	Y_i (m)	Z_i (m)	B_{APSS} (10^4 nT)		X_i (m)	Y_i (m)	Z_i (m)	B_{AOS} (10^4 nT)
M_{APSS}	0.00	0.00	0.00	NA	M_{AOS}	0.00	0.00	0.00	N/A
N2	-0.03	-2.30	1.32	5.086	N1	-0.03	-2.38	1.42	5.102
N3	-0.04	-2.23	1.23	5.081	N3	-0.04	-2.23	1.19	5.098
N7	-0.16	-1.73	1.43	4.858	N7	-0.16	-1.73	1.39	4.873
N9	-0.19	-1.61	1.22	4.787	N9	-0.19	-1.61	1.19	4.815
N16	0.12	1.94	0.61	6.006	N16	0.12	1.94	0.58	6.006
N18	0.17	2.10	0.49	5.818	N18	0.17	2.10	0.45	5.807
N20	-0.22	3.09	0.81	5.413	N19	-0.20	2.97	0.84	5.439
N21	-0.23	3.17	0.70	5.394	N21	-0.23	3.17	0.67	5.394

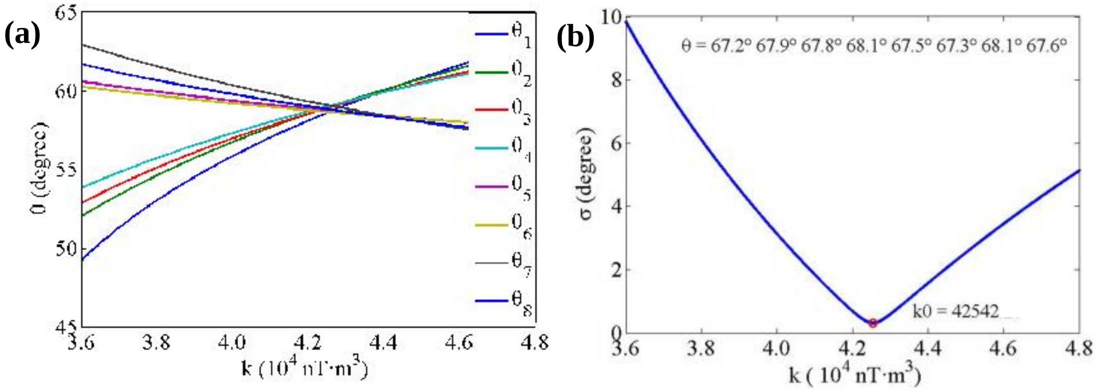

Figure 3.7. Evaluation of θ and k values from the APSS: (a) eight θ samples for each k, and (b) standard deviation of eight θ samples as a function of k value.

Similarly, in the case of the AOS, the eight curves shown in Figure 3.8 (a) provide a k value of 41890 nT·m^3 corresponding to the minimum standard deviation as presented in Figure 3.8 (b). In this case, the eight θ values are *66.9º*, *66.4º*, *66.2º*, *66.0 º*, *66.7º*, *66.8º*, *66.3º*, and *66.1º* with their mean and standard deviation of 66.4º and 0.32º, respectively. The coefficient of variation of θ is *0.322°/66.4° = 0.48%*. The differences in the evaluation of *k* and *θ* were likely caused by the approximate trial-and-error method, the imperfect alignment between the Y-axis and y-axis, the small angle deviation from due south of the APSS, and the misalignment of the prism and the magnetometer sensor for coordinate measurements.

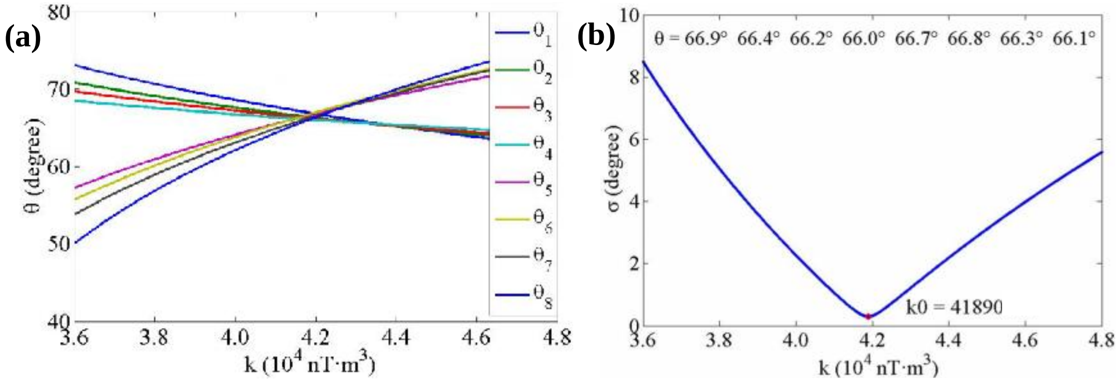

Figure 3.8. Evaluation of *θ* and *k* values from the AOS: (a) eight *θ* samples for each *k* and (b) standard deviation of eight *θ* samples as a function of *k* value.

To sum up, the *k* values for the APSS and AOS obtained from the calibration test are 42542 nT·m^3 and 41890 nT·m^3, respectively. The *θ* values for the APSS and AOS are 67.7 ° and 66.4 °, respectively. Due to low accuracy with the level bubble used on top of the APSS, an initial angle exists between the axis of the magnet and the horizontal plane. As a result, the 67.7° is the angle between the dip angle of the Earth's magnetic field and the axis of the magnet instead of the horizontal plane. On the other hand, a high-precision level bubble was installed on top of the AOS to ensure that the axis of the magnet aligns with the horizontal plane. Therefore, *θ* = 66.4 ° is considered as the final inclination angle of the uniform Earth's magnetic field in the open field.

3.5. RESULTS AND DISCUSSION OF MAGNET LOCALIZATION

In this section, the measured data collected from the test were used to conduct the localization of AOS with three orientations and the localization of APSS placed at the origin of the global coordinate system to validate the localization algorithm. Also, the selection of measurement points was analyzed to determine the effective measurement points during the test.

3.5.1. Localization of AOS. Table 3.2 shows the coordinates (X_i, Y_i, Z_i) and intensity $B_{//i}^{(M)}$ of the AOS in three orientations OR1, OR2 and OR3, as shown in Figure 3.9, measured at locations Q_1 to Q_{27}, respectively. The three orientations were selected arbitrarily to represent the random rotating of the smart rock in the river. In the coordinate system O-XYZ as shown in Figure 3.9, the south-to-north pole direction (y-axis) of the magnet in OR1 points to the northwest & down octant of the coordinate system while the south-to-north pole direction (y-axis) of the magnet in OR2 and OR3 points to the southeast & up and southwest & up octants, respectively. The coordinate and orientation of the magnet in each of the three cases (OR1, OR2, OR3) were determined by first substituting the coordinates of 27 points into Eq. (3.4-3.6) to obtain the relationship between the predicted total intensity $B_{//i}^{(P)}$ and the six unknowns, and then minimizing the objective function in Eq. (3.7) after substituting the corresponding total intensity $B_{//i}^{(M)}$ measured to evaluate the six unknowns.

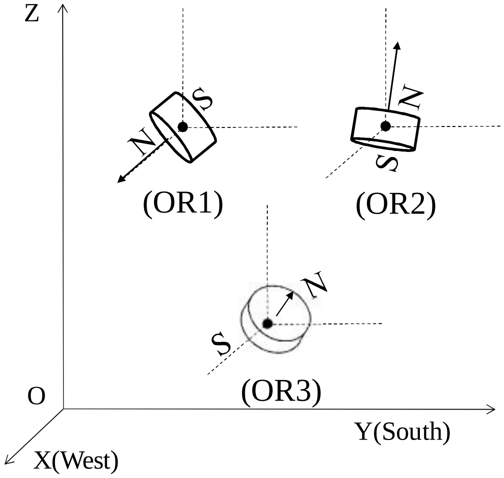

Figure 3.9. Three orientations of the AOS.

Table 3.3 summarizes the predicted and measured coordinates of the magnet in the AOS, named M_{AOS}, in three orientations (OR1, OR2, and OR3) as well as the SRSS prediction errors in $\mathrm{M_{AOS}}$ location estimation. Since the AOS in each of the three orientations (OR1, OR2 and OR3) was placed at the origin of the O-XYZ coordinate system, the ground truth coordinates of the AOS were zero. It can be observed from Table 3.3 that the SRSS prediction errors in three orientations location are 0.01 m, 0.01 m and 0.01 m, respectively. They are pretty small compared to the size of the magnet, which is about 0.1 m in diameter.

Table 3.2. Measured data for the AOS in three orientations

Sensor Head	X_i (m)	Y_i (m)	Z_i (m)	B_i^M (10^4 nT)		
				OR1	OR2	OR3
Q_1	0.64	2.57	0.65	5.265	5.305	5.001
Q_2	1.15	3.69	0.25	5.182	5.284	5.180
Q_3	1.02	1.58	0.68	5.189	5.486	4.593
Q_4	2.03	2.61	0.57	5.170	5.325	5.142
Q_5	2.45	1.19	0.74	5.058	5.416	5.153
Q_6	3.67	0.80	0.50	5.152	5.314	5.244
Q_7	2.29	0.02	0.88	4.918	5.517	5.253
Q_8	4.56	0.04	0.22	5.193	5.274	5.254
Q_9	3.31	-0.64	0.49	5.138	5.333	5.285
Q_{10}	1.71	-1.11	0.95	4.852	5.581	5.437
Q_{11}	2.28	-2.21	0.65	5.159	5.331	5.293
Q_{12}	2.16	-2.99	0.47	5.203	5.287	5.257
Q_{13}	0.71	-2.10	0.88	5.002	5.504	5.401
Q_{14}	0.48	-3.61	0.81	5.189	5.299	5.244
Q_{15}	-0.59	-2.62	0.95	5.093	5.398	5.312
Q_{16}	-1.83	-4.00	0.32	5.201	5.278	5.218
Q_{17}	-1.78	-2.67	0.59	5.135	5.352	5.249
Q_{18}	-1.06	-1.23	0.40	4.517	6.106	5.766
Q_{19}	-2.75	-1.63	0.66	5.134	5.341	5.297
Q_{20}	-2.46	-0.05	0.91	5.223	5.289	5.447
Q_{21}	-3.98	-0.06	0.14	5.180	5.286	5.269
Q_{22}	-1.34	0.74	0.74	6.129	4.959	5.619
Q_{23}	-3.07	0.94	0.13	5.181	5.317	5.319
Q_{24}	-3.99	2.22	0.22	5.223	5.254	5.257
Q_{25}	-2.35	2.01	0.39	5.264	5.265	5.277
Q_{26}	-0.79	1.99	0.77	5.597	5.111	4.979
Q_{27}	-1.64	3.31	0.32	5.254	5.255	5.217

Table 3.3. Predicted and measured coordinates of the magnet M_{AOS} in three orientations

	OR1			OR2			OR3		
	X (m)	Y (m)	Z (m)	X (m)	Y (m)	Z (m)	X (m)	Y (m)	Z (m)
Predicted Location	-0.01	0.00	0.01	0.00	0.00	-0.01	0.00	0.01	-0.01
Measured Location	0.00	0.00	0.00	0.00	0.00	0.00	0.00	0.00	0.00
Prediction Error	-0.01	0.00	0.01	0.00	0.00	-0.01	0.00	0.01	-0.01
SRSS Error	0.01			0.01			0.01		

Table 3.4 lists the predicted rotation angles *α*, *β* and *γ* and the directional cosines *l*, *m*, and *n* of the magnet in the AOS in the global coordinate system. The rotation angles (*α*, *β*, *γ*) adopted for the coordinate transformation are difficult to visualize in space while the directional cosines (*l*, *m*, *n*) of the magnet represent the angles between the local y-axis (south-to-north pole direction) and the global axis X (west), Y (south) and Z (up), respectively.

Table 3.4. Predicted orientations of the AOS in three cases

	OR1 (rad)			OR2 (rad)			OR3 (rad)		
	α	*β*	*γ*	*α*	*β*	*γ*	*α*	*β*	*γ*
Predicted	1.04	3.88	3.12	4.67	3.69	2.77	3.36	3.33	2.59
AOS Orientation	*l*	*m*	*n*	*l*	*m*	*n*	*l*	*m*	*n*
	0.56	-0.52	-0.64	-0.47	0.23	0.85	0.47	0.86	0.21

3.5.2. Localization of APSS. Similarly, Table 3.5 shows the measured coordinates (X, Y, Z) of 27 points and their corresponding total magnetic field intensities of the APSS as well as the SRSS error in location prediction. It can be observed from Table 3.5 that the SRSS prediction error in location is 0.07 m, which is quite small compared to the size of the APSS with 0.2 m in diameter of the outside plastic ball. It is noted that the orientation of magnet in the APSS is known *in prior* so that the process of locating the APSS is significantly simpler than that of the AOS. Therefore, the APSS is a preferable configuration of smart rocks in practical applications.

3.5.3. Analysis for the Selection of Measurement Points. As shown in Figure 3.5 (c), the measurement points were selected between 1.5 m and 5 m distances from the APSS or AOS placed at the origin of the coordinate system. They were well distributed around the APSS or AOS in near and far radial distances. Although a minimum of three measurement points are required for three unknown location parameters of the APSS and six measurement points for six unknown location parameters of the AOS, more measurement points lead to a more reliable and accurate estimation of the APSS or AOS location. Herein, 27 points were initially selected to ensure the convergence and high accuracy in the estimation of the unknown parameters.

Since the magnetic flux intensity of a permanent magnet decreases in cubic function with the measurement distance, effective measurements that allow the reverse estimation of the magnet location must be taken in a certain range of distance. On one hand, to simplify the permanent magnet as a dipole in Eq. (3.2), the distance from a field point to the magnet is at least ten times the size of the magnet or 0.1 m. Considering the presence of dead zones with the magnetometer used in this study, where the magnetometer cannot provide the correct magnetic field intensity, the lower limit of measurement distance is determined to be 1.5 m.

Table 3.5. Predicted and measured data for the APSS location M_{APSS}

Sensor Head	X_i (m)	Y_i (m)	Z_i (m)	$B_i^{(M)}$ (10^4 nT)
Q_1	0.64	2.57	0.63	5.450
Q_2	1.15	3.69	0.24	5.294
Q_3	1.02	1.58	0.67	5.861
Q_4	2.03	2.61	0.56	5.309
Q_5	2.45	1.19	0.73	5.254
Q_6	3.67	0.80	0.49	5.208
Q_7	2.29	0.02	0.87	5.116
Q_8	4.56	0.04	0.21	5.212
Q_9	3.31	-0.64	0.48	5.183
Q_{10}	1.71	-1.11	0.94	4.985
Q_{11}	2.28	-2.21	0.64	5.209
Q_{12}	2.16	-2.99	0.45	5.243
Q_{13}	0.71	-2.10	0.86	5.155
Q_{14}	0.48	-3.61	0.80	5.245
Q_{15}	-0.59	-2.62	0.94	5.199
Q_{16}	-1.83	-4.00	0.31	5.252
Q_{17}	-1.78	-2.67	0.58	5.234
Q_{18}	-1.06	-1.23	0.39	5.239
Q_{19}	-2.75	-1.63	0.65	5.185
Q_{20}	-2.46	-0.05	0.90	5.137
Q_{21}	-3.98	-0.06	0.12	5.200
Q_{22}	-1.34	0.74	0.72	5.629
Q_{23}	-3.07	0.94	0.12	5.200
Q_{24}	-3.99	2.22	0.21	5.229
Q_{25}	-2.35	2.01	0.38	5.281
Q_{26}	-0.79	1.99	0.76	5.730
Q_{27}	-1.64	3.31	0.31	5.297
Predicted Location $M^{(P)}_{APSS}$	0.02	0.01	0.07	N/A
Measured Location $M^{(M)}_{APSS}$	0.00	0.00	0.00	
Location Prediction Error for M_{APSS}	0.02	0.01	0.07	
SRSS Error in Coordinate			0.07 m	

On the other hand, the upper limit of measurement distance depends on the coefficient *k*, which represents the magnetic strength of the dipole. The larger the coefficient *k*, the stronger the magnetic flux intensity of the permanent magnet at a certain distance. Therefore, the larger the coefficient *k*, the further distance the magnetic flux intensity can be detected with confidence. For the magnets used in the open field tests, $k = 42542$ nT·m^3 or 41890 nT·m^3 determines the upper limit of measurement distance for effective localization of the magnets. Figure 3.10(a) presents the total magnetic field intensity as a function of distance along the symmetry axis (Y direction) of the dipole at five elevations in Z direction. That is, $x = 0$, $1.5 \text{ m} \leq y \leq 7.0 \text{ m}$, $z = 0.3$ m, 0.5 m, 0.7 m, 0.9 m and 1.0 m in Eq. (3.6). Obviously, the total intensity decreases rapidly from 1.5 m to 4.0 m and then slowly afterward. As shown in Figure 3.10(b) for the zoom-in view, at a low level of 0.3 m in Z direction, the attenuations of the magnetic intensity from 4.0 m to 5.0 m and from 5.0 m to 6.0 m are 330 nT and 123 nT, respectively. The decreases in magnetic intensity from 4.0 m to 5.0 m distance are 368 nT, 397 nT, 415 nT and 420 nT for Z = 0.5 m, 0.7 m, 0.9 m and 1.0 m, respectively; the decreases from 5.0 m to 6.0 m are 154 nT, 166 nT, 176 nT and 180 nT, respectively. In practical applications, the measured magnetic intensity can deviate from the calculated intensity by ±200 nT as a result of such combined experimental errors as the deviation of the sensor position for magnetic intensity measurement, the coordinate deviation of the measurement points, and the change of the Earth magnetic field because of the solar storm. Therefore, those attenuations from 5.0 m to 6.0 m at various Z levels, less than 200 nT, are not a sensitive and effective distance range for measurement points' selection compared to those attenuation from 4.0 m to 5.0 m larger than 300 nT.

Figure 3.11(a) displays the magnetic field changes along Z direction at three Y positions (4.0 m, 5.0 m, 6.0 m) in YOZ plane. The magnetic field intensity first increases from Z= 0 m to Z = 2.0 m and then decreases monotonically with the distance in Z direction. Figure 3.11(b) shows an amplified observation on the magnetic intensity over the distance in Z direction. It is also seen from Figure 3.11 (b) that the desirable distance in Z direction for the collection of sensitive magnetic intensities is less than 5.0 m as would be between 5 m and 6 m in Y direction for a magnetic field difference of less than 200 nT. The same idea is applicable to the magnetic intensity variation in X direction. Therefore, the upper limit of 5.0 m for the selection of measurement points was determined in XOY plane as shown in Figure 3.5 (c).

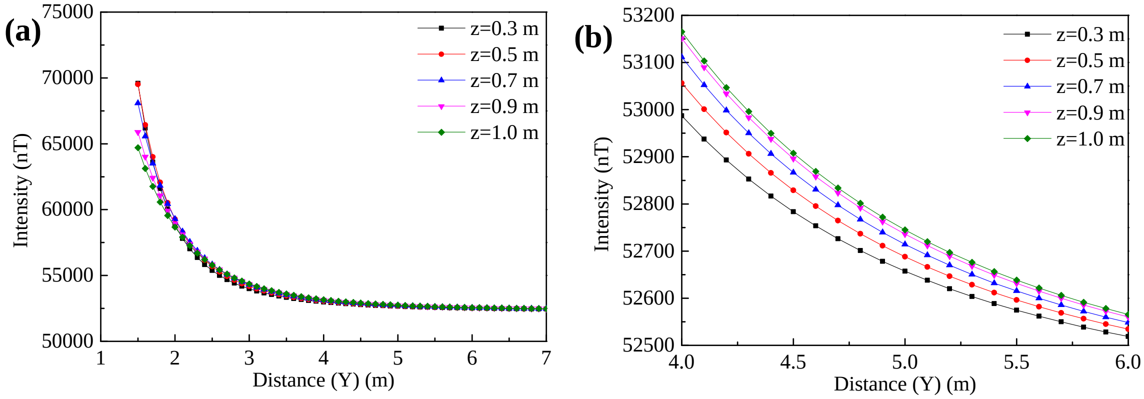

Figure 3.10. Magnetic field intensity vs. measurement distance in Y direction: (a) overall view and (b) zoom-in view.

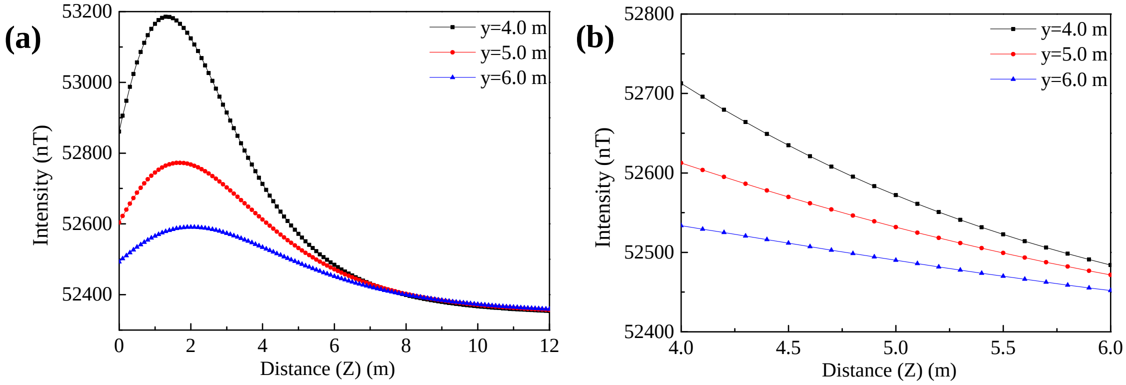

Figure 3.11. Magnetic field intensity vs. measurement distance in Z direction: (a) overall and (b) zoom-in view.

3.6. APPLICATION OF THE APSS

As stated previously, the smart rock technology is developed to mainly monitor the maximum depth of the scour hole around a bridge pier or abutment in real time. Thus, tracking the movement of a smart rock over time is highly desirable during a flood event. Another field test was conducted to demonstrate the movement characteristic of a smart rock with the APSS on a slope and validate the localization method developed in this study.

3.6.1. Experimental Layout. A natural slope located in the same open field at Ber Juan Park, Rolla, MO, was chosen as the test site as shown in Figure. 3.12(a). The natural slope from the top to bottom was used to simulate the movement of the smart rock in a scour hole. Along the slope eight stops of the APSS were marked as M1 to M8 in Figure 3.12(a). The eight APSS stops were surrounded by a total of 44 measurement points designated as S_1, S_2… S_{44}, as marked in Figure 3.12(b). A total station was set up at the origin of the O-XYZ coordinate system with the Y-axis approximately pointed to the geographic South, the X-axis perpendicular to Y-axis pointed to West, and the Z-axis pointed up according to the right hand rule. The total station was used to survey the coordinate of each measurement point and the ground truth coordinate of the APSS. Prior to the APSS deployment, the magnetometer G858 was employed to measure the uniform ambient magnetic field intensity. After the APSS had been deployed at each of the eight positions, the total magnetic field intensity was measured again. For each APSS deployment, 18 measurement points were selected from 44 points within a radial distance of *1.5 m* and *5.0 m*.

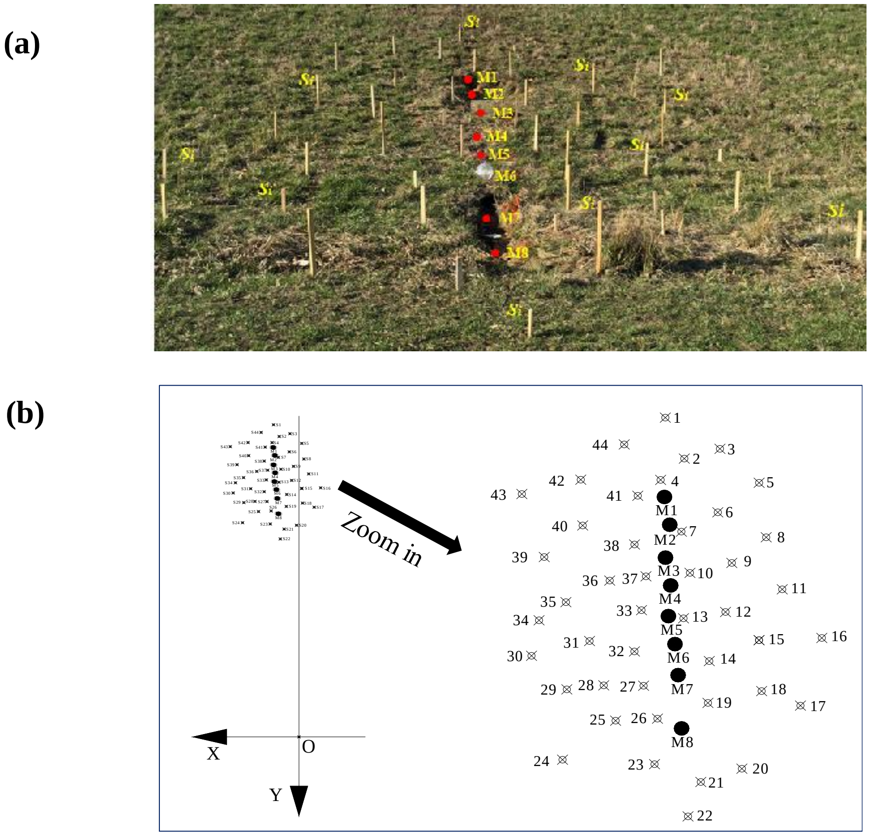

Figure 3.12. The APSS and measurement points: (a) test site and (b) schematic view.

When the APSS was placed at M1, each measurement includes the total magnetic field intensity and its corresponding coordinate in the O-XYZ Cartesian coordinate system. By minimizing the objective function in Eq. (3.7), the coordinate of M1 was predicted as designated as M1’ in Table 3.6. Similarly, the predicted location of the APSS at M2 to M8 can be determined; they are designated as M2’, M3’, M4’, M5’, M6’, M7’, and M8’ in Table 3.6.

3.6.2. Results. Table 3.6 shows the measured and predicted locations of the APSS in the O-XYZ system and the prediction error. It can be seen from Table 3.6 that the component and SRSS errors for eight locations of the APSS are all less than 13.6 mm, which is quite small compared to the size of the APSS. Therefore, the accuracy of the localization algorithm in Eq. (3.7) is sufficient in the uniform ambient magnetic field. Figure 3.13 shows a graphical presentation of the eight measured and predicted locations of the APSS on a three-dimensional slope surface. Each pair of the measured and predicted locations are nearly overlapped. In practical applications, such as monitoring of a bridge scour process, the APSS is initially deployed at the M1 location and the other locations from M2 to M8 represent the water flow induced movement of the APSS at various stops over time.

Table 3.6. Predicted and measured data for the APSS location

	Measured Coordinate				Predicted Coordinate			Prediction Error			
Stop	*X* (m)	*Y* (m)	*Z* (m)	Stop	*X'* (m)	*Y'* (m)	*Z'* (m)	(*X*-*X'*) (m)	(*Y*-*Y'*) (m)	(*Z*-*Z'*) (m)	SRSS (m)
M1	-2.31	-29.44	-0.17	M1’	-2.31	-29.44	-0.15	0.00	0.00	-0.01	0.01
M2	-2.16	-28.63	-0.39	M2’	-2.16	-28.64	-0.39	0.00	0.00	0.00	0.00
M3	-2.28	-27.67	-0.63	M3’	-2.28	-27.68	-0.64	0.00	0.01	0.01	0.01
M4	-2.14	-26.86	-0.84	M4’	-2.14	-26.86	-0.83	0.00	0.00	-0.01	0.01
M5	-2.20	-25.97	-1.09	M5’	-2.20	-25.97	-1.09	0.00	0.00	0.00	0.00
M6	-2.02	-25.15	-1.24	M6’	-2.02	-25.16	-1.24	-0.01	0.00	0.00	0.00
M7	-1.94	-24.25	-1.62	M7’	-1.93	-24.25	-1.63	0.00	0.00	0.01	0.01
M8	-1.84	-22.70	-1.62	M8’	-1.85	-22.70	-1.62	0.00	0.00	0.01	0.01

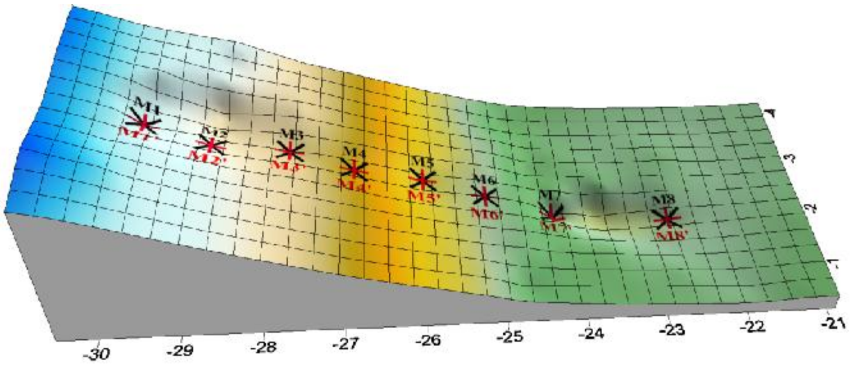

Figure 3.13. Comparison between the measured and predicted APSS locations.

3.7. SUMMARY

The smart rock technology offers an alternative to investigate the behavior of scour development around a bridge pier or abutment and the effectiveness of a riprap counter measurement. Proper designed smart rocks roll and fall into the scour hole around the pier or abutment. Their position is thus related to the depth of the scour hole. The permanent magnet embedded in a smart rock generates the magnetic field that can be detected by magnetic sensors or a magnetometer. The detected magnetic field intensities and given magnetometer's position can be utilized to locate the smart rock. In this section, smart rocks with the AOS and APSS have been demonstrated for the field evaluation of their localization. The AOS is simple in fabrication and high in localization accuracy. However, the localization algorithm is complex with six unknowns: three location coordinates and three orientations of the magnet. The APSS with fixed orientation reduces unknowns to three location coordinate only, which greatly simplifies the localization algorithm and improves the computational efficiency without sacrificing the localization accuracy. Therefore, the APSS is a preferred configuration in practical applications.

The localization tests in the open field have demonstrated that the magnetic dipole simplification of a permanent magnet is sufficiently accurate for the localization of smart rocks with the AOS and APSS. The Earth’s magnetic field in the form of parallel vectors at an open site cannot be separated from the magnetic field generated from a magnet in field measurements.

The APSS was applied to simulate the movement of a smart rock in a scour hole created under water flow in application by placing it at eight stops on a natural slope. This test further demonstrated the high accuracy and repeatability of the localization of the APSS at various locations in the same uniform ambient field.

4. LOCALIZATION OF A SINGLE SMART ROCK IN NON-UNIFORM AMBIENT MAGNETIC FIELD

4.1. INTRODUCTION

The total magnetic field around a bridge site is affected by a permanent magnet, the Earth, and any other ferromagnetic substances such as the reinforcement in bridge piers and deck. Since the magnetic field distribution of other substances is unknown, the combined effect of the Earth and other substances or the ambient magnetic field at the bridge site is non-uniform. To enable the localization of smart rocks, the non-uniform ambient magnetic field intensity must be evaluated accurately.

In this section, the localization algorithms of the AOS and APSS in non-uniform magnetic field at the bridge site are developed by modifying the algorithms presented in Section 3. Unlike the Earth's magnetic field with parallel magnetic lines, the non-uniform ambient magnetic field makes the direction and intensity of the magnetic field at each measurement point unknown. Therefore, a custom-built device is designed and built to detect the ambient magnetic field direction. This device is referred to as the Ambient Magnetic Field Orientation Device (AMFOD). It can determine inclination and declination angles of the ambient magnetic field at various measurement points. The experimental field tests were carried out at the bridge site of Highway 63 over Gasconade River to demonstrate the localization procedure and validate the localization algorithm using the AOS and APSS. The magnetometer G858 and the device AMFOD were used to collect the ambient, total magnetic field intensities and directions, respectively. The device AMFOD was used to detect the direction of the ambient magnetic field at each measurement point.

4.2. MATHEMATIC MODEL OF THE MAGNETIC FIELD AT BRIDGE SITE

The magnetic field at a bridge site is a combination of the Earth's magnetic field and the field produced by the steel rebar embedded in the bridge pier and deck or the steel girders. This combination at a local area such as bridge site is designated as the ambient magnetic field, which is a vector superstition of the Earth's magnetic field and the field from ferromagnetic substances such as steel objects. Although the ambient magnetic field cannot be simply expressed in a mathematical model, the magnitude and direction of the ambient magnetic field at any point can be measured by magnetometer G858 or the custom-built device, respectively.

The local magnetic field generated by a magnet is referred to as magnet's magnetic field (MMF). It can be expressed by a mathematic function. The vector summation of the AMF and MMF forms the total magnetic field as smart rocks are deployed at bridge sites.

As illustrated in Figure 4.1 in the O-XYZ Cartesian coordinate system, the center of a magnet is located at Point P (X_M, Y_M and Z_M), and an arbitrary measurement station around the magnet is located at Point Q_i (X_i, Y_i, and Z_i) (i =1 to n). The ambient magnetic field at Point Q_i (X_i, Y_i, Z_i), is represented by a vector $\boldsymbol{B_{Ai}}$, which is determined by a magnetic flux density B_{Ai} and two angles, θ and φ. The parameter φ in [0, 2π] is the angle spanned from the X axis to the projected vector of the ambient magnetic field vector $\boldsymbol{B_{Ai}}$ in XOY plane; the parameter θ in [0, π] represents the angle spanned from the projected vector to $\boldsymbol{B_{Ai}}$. Therefore, the three components (B_{AXi}, B_{AYi}, B_{AZi}) of the ambient magnetic field along X-, Y-, and Z-directions are:

$$B_{AXi} = B_{Ai} \cos ¯ \cos ¨ \tag{4.1a}$$

$$B_{AYi} = B_{Ai} \cos ¯ \sin ¨ \tag{4.1b}$$

$$B_{AZi} = B_{Ai} \sin ¯ \tag{4.1c}$$

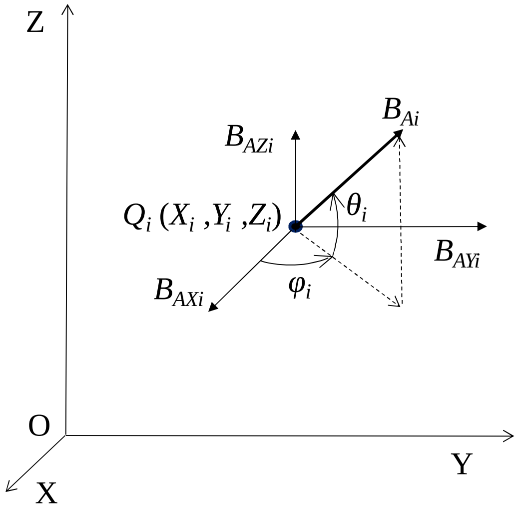

Figure 4.1. A magnet and measurement point Q_i in the global Cartesian coordinate system O-XYZ.

A permanent magnet with uniform magnetization can be modeled as a magnetic dipole when measurements are taken at a distance from the magnet that is significantly greater than the largest dimension of the magnet. The magnetic flux density of a magnetic dipole source is a high-order nonlinear function of the coordinates at a measurement point. As illustrated in Figure 4.2, the center of the magnet is located at Point *P* (X_M, Y_M, Z_M) in the global Cartesian coordinate system O-XYZ and *p* (0, 0, 0) in the local Cartesian coordinate system *p*-xyz. Point *q* (x_i, y_i, z_i) in the local coordinate system and point Q_i (X_i, Y_i, Z_i) in the global coordinate system represent an arbitrary measurement point. The magnetic field intensity vector at Point Q_i (X_i, Y_i, Z_i) (i =1 to n) is represented by $\boldsymbol{B_{Mi}}$ and the expressions for its three components (B_{MXi}, B_{MYi}, B_{MZi}) are written as (repeated for completeness):

$$\begin{pmatrix} B_{MXi} \\ B_{MYi} \\ B_{MZi} \end{pmatrix} = \mathbf{R}^{-1} \begin{pmatrix} k\dfrac{3x_i y_i}{r^5} \\ k\dfrac{2y_i^2 - x_i^2 - z_i^2}{r^5} \\ k\dfrac{3z_i y_i}{r^5} \end{pmatrix} \tag{4.2a}$$

$$\begin{pmatrix} x_i \\ y_i \\ z_i \end{pmatrix} = \mathbf{R} \cdot \begin{pmatrix} X_i - X_M \\ Y_i - Y_M \\ Z_i - Z_M \end{pmatrix} \tag{4.2b}$$

$$\mathbf{R} = \begin{bmatrix} \cos\beta\cos\gamma & \cos\beta\sin\gamma & -\sin\beta \\ \sin\alpha\sin\beta\cos\gamma - \cos\alpha\sin\gamma & \sin\alpha\sin\beta\sin\gamma + \cos\alpha\cos\gamma & \sin\alpha\cos\beta \\ \cos\alpha\sin\beta\cos\gamma + \sin\alpha\sin\gamma & \cos\alpha\sin\beta\sin\gamma - \sin\alpha\cos\gamma & \cos\alpha\cos\beta \end{bmatrix} \tag{4.2c}$$

$$r = \sqrt{x_i^2 + y_i^2 + z_i^2} \tag{4.2d}$$

$$B_{Mi} = \sqrt{B_{MXi}^2 + B_{MYi}^2 + B_{MZi}^2} \tag{4.2e}$$

where $k = \mu_0\mu / 4\pi$ is the a coefficient related to the magnet, μ_0 is the magnetic permeability of the air in *T·m/A*, μ is the magnetic moment of the dipole produced by the magnet in T, and $\alpha \in [0, 2\pi]$, $\beta \in [0, 2\pi]$, $\gamma \in [0, 2\pi]$ are Euler angles used to derive the rotation matrix. Let the unit vector of y-axis in the global coordinate system be $\mathbf{n}_y = (l, m, n)^T$, which points from South to North pole of the magnet. The vector defines the orientation of the magnet with the unity constraint represented by $l^2 + m^2 + n^2 = 1$. It is noted that the three components in the second column of the rotation matrix are equal to *l*, *m* and *n*, respectively.

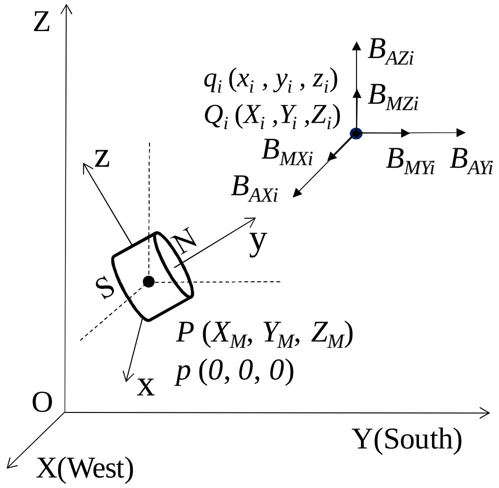

Figure 4.2. AOS in local and global coordinate systems and the ambient magnetic field.

The total magnetic field intensity $B_{//i}$ at Point Q_i from the magnet and the ambient magnetic field can be expressed into:

$$B_{//\mathrm{i}} = \sqrt{(B_{MXi} + B_{AXi})^2 + (B_{MYi} + B_{AYi})^2 + (B_{MZi} + B_{AZi})^2} \tag{4.3}$$

It depends upon the ambient magnetic field intensity B_{Ai}, the θ and φ angles of the ambient magnetic field, the coefficient k of the magnet, the location (X_M, Y_M, Z_M) and orientation (α, β, γ) of the magnet. That is, $B_{//i} = B_{//i}\,(B_{Ai}, \theta, \varphi, k, X_M, Y_M, Z_M, \alpha, \beta, \gamma, X_i, Y_i, Z_i)$. The ambient magnetic field intensity B_{Ai}, the θ and φ angles are measured using the 3-axis magnetometer and custom-built device prior to AOS deployment at a predetermined site. The coefficient k related to the magnetic moment of the magnet is obtained from the calibration test or from the properties of the magnet provided by the manufacturer. Given k, θ , φ and B_A at each measurement point (X_i, Y_i, Z_i) of a project site, the total magnetic field intensity of the ambient and magnet $B_{//i}$ is a function of (X_M, Y_M, Z_M) and (α, β, γ).

4.3. LOCALIZATION OF AOS

To solve the six parameters $(X_M, Y_M, Z_M, \alpha, \beta, \gamma)$ in the high-order nonlinear equations, an objective error function is formulated in the optimization algorithm.

Assume that N number of measurements, $B_{//i}^{(M)}$ (i=1, 2, …, n), are taken at N stations around the AOS (X_i, Y_i, and Z_i, i =1, 2, …, n) from the magnetometer. At each station, the theoretically predicted intensity $B_{//i}^{(P)} = B_{//i}$ can be calculated by combing Eq. (4.2) and Eq. (4.3). The square-root-of-the-sum-of-the-squared (SRSS) error between the calculated intensity $B_{//i}^{(P)}$ and the measured intensity $B_{//i}^{(M)}$, $J(X_M, Y_M, Z_M, \alpha, \beta, \gamma)$, can be expressed into:

$$J(X_M, Y_M, Z_M, \sim, \quad ,¥) = \sqrt{\sum_{i=1}^{n}[B_i^{(P)} - B_i^{(M)}]^2} \tag{4.4}$$

By minimizing the SRSS error in Eq. (4.4) through a numerical algorithm, the location and orientation parameters of the magnet can be determined.

4.4. LOCALIZTION OF APSS

As discussed in Section 3, the APSS can be represented by $\alpha = \pi$, $\beta = 0$, and $\gamma = 0$ in the global coordinate system as shown in Figure 4.3. The local xyz coordinate system with y-axis from the South to North pole of the magnet is identical to the XYZ coordinate system when rotated counter-clockwise by 180°. In this case, the three components (B_{MXi}, B_{MYi}, B_{MZi}) of the magnetic field generated from the magnet at the arbitrary point Q_i can be expressed into:

$$\begin{pmatrix} B_{MXi} \\ B_{MYi} \\ B_{MZi} \end{pmatrix} = \begin{pmatrix} -k\dfrac{3(X_i - X_M)(Y_i - Y_M)}{\left(\sqrt{(X_i - X_M)^2 + (Y_i - Y_M)^2 + (Z_i - Z_M)^2}\right)^5} \\ -k\dfrac{2(Y_i - Y_M)^2 - (X_i - X_M)^2 - (Z_i - Z_M)^2}{\left(\sqrt{(X_i - X_M)^2 + (Y_i - Y_M)^2 + (Z_i - Z_M)^2}\right)^5} \\ -k\dfrac{3(Z_i - Z_M)(Y_i - Y_M)}{\left(\sqrt{(X_i - X_M)^2 + (Y_i - Y_M)^2 + (Z_i - Z_M)^2}\right)^5} \end{pmatrix} \tag{4.5}$$

The total magnetic field intensity $B_{//i}$ at Point Q_i for the APSS model is then obtained by substituting Eq. (4.5) into Eq. (4.3). The SRSS error in Eq. (4.4) is also simplified into J (X_M, Y_M, Z_M) as indicated in Eq. (4.6), in which the theoretically predicted intensity $B_{//i}^{(P)} = B_{//i}$ can be evaluated by introducing Eq. (4.5) into Eq. (4.3) and $B_{//i}^{(M)}$ ($i=1, 2, \ldots, N$) are taken at N stations around the magnet.

$$J(X_M, Y_M, Z_M) = \sqrt{\sum_{i=1}^{n} [B_i^{(P)} - B_i^{(M)}]^2} \tag{4.6}$$

The sequential quadratic programming (SQP) algorithm implemented in the Fmincon code in MATLAB was used to find the solution for the minimization of the SRSS error function in Eq. (4.6).

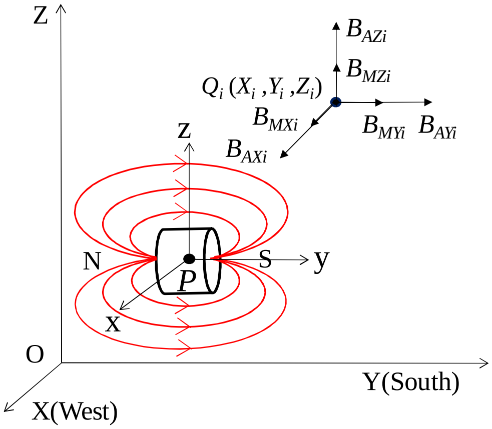

Figure 4.3. The magnetic field of the APSS and the ambient magnetic field.

4.5. DEVELOPMENT OF AMFOD

The Ambient Magnetic Field Orientation Device (AMFOD) was developed to determine the direction of the ambient magnetic field at a bridge site. The AMFOD is composed of an orientation detector (OD), an OD support, a data reading system, two laser pointers, a high-precision bubble level and a tripod to support the measurement setup. Figures 4.4(a) and 4.4(b) show a schematic view and a prototype of the AMFOD.

The OD was created based on the APSS model. It was utilized to capture the direction of the ambient magnetic field at each measurement point in a quite accurate way. The OD consists of an inside ball and an outside ball, two identical cylindrical hollow magnets, and liquid filled in between the two balls. The key to the design of the two balls is to keep the geometrical center of the inside ball aligned with that of the outside ball. The inside ball and the outside ball were produced by a 3D printer using the Polymeric Methyl Methacrylate due to their high precision requirement. The two cylindrical hollow magnets are 19 mm in diameter and 25.4 mm in height with a 2 mm diameter hole through its center line. The reserved space through the center line of the inside ball was designed to place the two cylindrical magnets. The liquid used to make the inside ball rotate freely is the propylene glycol with a mass density of 1040 kg/m^3 to satisfy both lubrication and nontoxicity requirements.

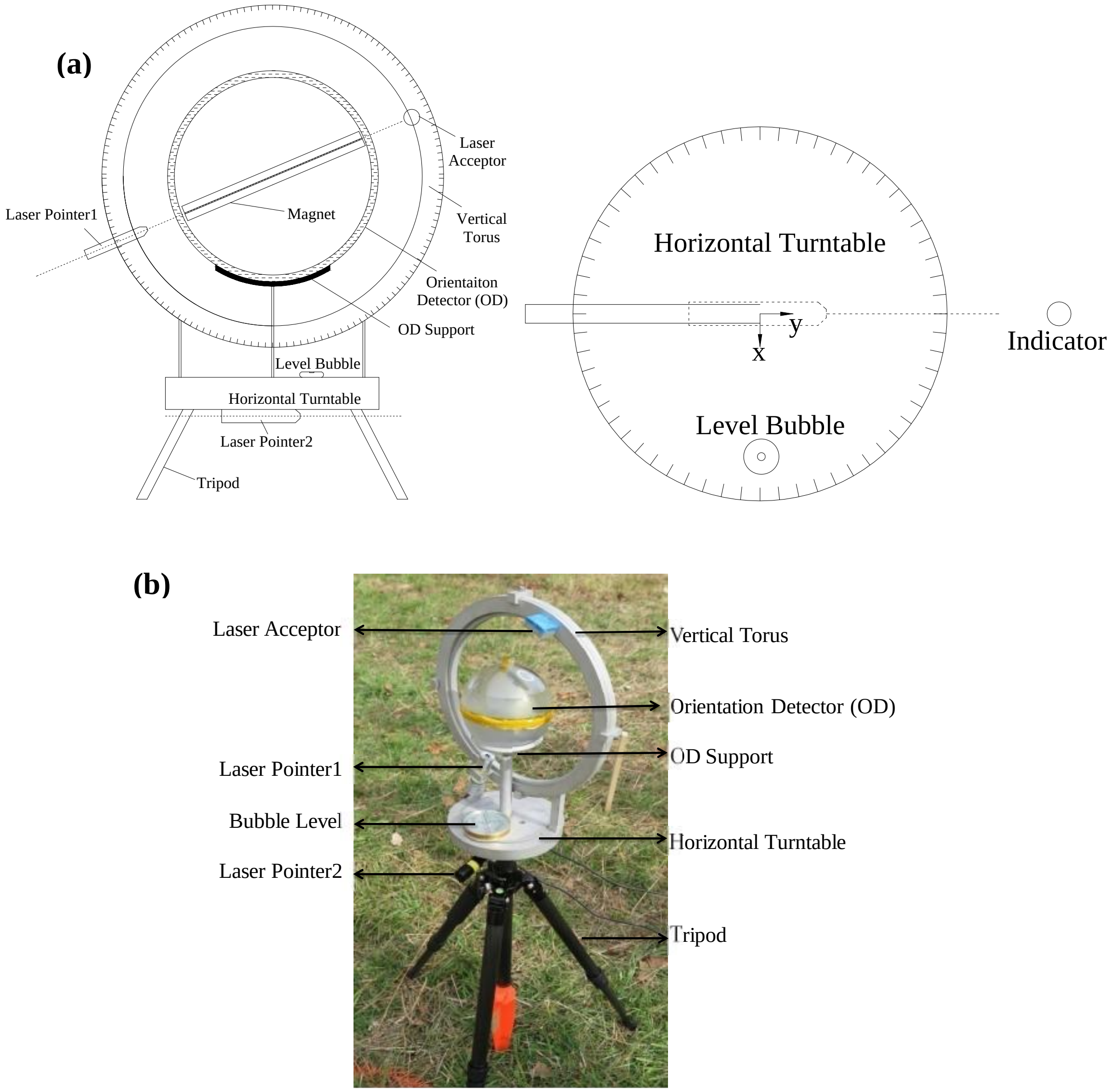

Figure 4.4. Overall design of AMFOD: (a) schematic view and (b) prototype.

The data reading system is composed of the OD support, the vertical torus for angle θ reading, and the horizontal turntable for angle φ reading. The accuracy of the data reading system is 0.1°. The data reading system was made of aluminum alloy without any ferromagnetic substance.

Two laser pointers were used in the design of the AMFOD. Laser pointer 1 was installed on vertical torus to shoot light on a laser acceptor through the hole along the centerline of the OD. The laser acceptor was fixed on the vertical torus. The light will go through the magnet, the geometric center of the OD, the center of the vertical torus and the center of the laser acceptor. Thus, the angle of θ is highlighted by the shooting light and read by the operator of the equipment. Laser pointer 2 is fixed at the bottom of the horizontal turntable and aligned with the diameter line of the turntable. The angle φ is obtained through this horizontal light shooting on a predefined point during a test. The two laser pointers are made of aluminum alloy and are charged by an external battery. Hence, the influence from the laser pointers on the magnetic field to be detected is negligible.

The bubble level made of plastic is placed on top of the horizontal turntable to ensure that it is indeed horizontal. The accuracy of the level bubble is 0.025°. The specially-designed tripod is made of carbon fiber that has no effect on the magnetic field to be measured. The connector between the tripod and the horizontal turntable is made for easy use for a large number of measurements in field conditions.

4.6. EXPERIMENTAL VALIDATION

In this section, one smart rock with Automatically Pointing to South System (APSS) and another smart rock Arbitrarily Oriented System (AOS) were tested at the Gasconade River Bridge site to validate the localization algorithms. The bridge pier for test was located on the river bank for easy operation.

4.6.1. Evaluation of *k*, B_A, *θ and φ*. The coefficient k was first evaluated in an open field (Ber Juan Park, Rolla, MO) before the smart rocks were tested at the bridge site. For the APSS and AOS, $k = 42542$ nT·m^3 and 41890 nT·m^3, respectively.

At the bridge site, the ambient magnetic field lines are no longer in parallel due to the combined effect of the Earth and other ferromagnetic substances, such as reinforcement in bridge piers and deck. The ambient magnetic field varies in space and can be uniquely defined by three parameters (B_A, θ and φ) at each measurement point. To evaluate these parameters, the AMFOD was used to measure the angles θ and φ at each measurement point in addition to a magnetometer for field intensity measurement.

4.6.2. Test Setup and Procedure. All tests were conducted near the bridge pier as shown in Figure 4.5. The bridge foundation was surrounded by a small scour hole created during previous flood events. As shown in Figure 4.6, three locations of the APSS or AOS, designated by M1, M2 and M3 in Figure 4.6(a), were selected to take into account a combination of horizontal positions and depths in bridge scour monitoring. M1, M2, and M3 were well spaced in horizontal plane. M3 was placed in the scour hole. To locate the APSS or AOS, a total of 34 measurement points (Q_1 to Q_{34}, marked by 34 wooden and plastic poles during actual tests), were selected around M1, M2, and M3. The sensor head of a G858 Magnetometer was placed on top of each wooden or plastic pole to measure the ambient and total magnetic intensities for each magnet location. A total station was used to survey the coordinates of three magnet's locations and 34 sensor positions as ground true data. A prism was placed at the same location of the sensor head on top of the wooden poles to ensure that the magnetic field intensity and the coordinates were collocated. In addition, the AMFOD was set at the 34 points to measure the angles of θ and φ before the smart rocks were deployed at each location.

Figure 4.5. The bridge pier with a scour hole as a field test site.

A step-by-step test procedure was developed and implemented systematically at the bridge site. The seven steps involved for the APSS or AOS are detailed below:

(1) *Set the XYZ Coordinate System.* As shown in Figure 4.6 (a), a point A marked by a wooden pole was selected far away from the bridge pier to avoid potential measurement interference by ferromagnetic substances of the bridge pier. Place a high-precision military compass on the wooden pole to survey the geographical South

direction, select a point B on the line of the south direction, and check that all of the measurement points were in the sight of point B. Select point B as the origin and the direction from A to B as the Y-axis. The X-axis is thus selected pointing to West and the Z-axis is perpendicular to the XOY plane as shown in Figure 4.6(a).

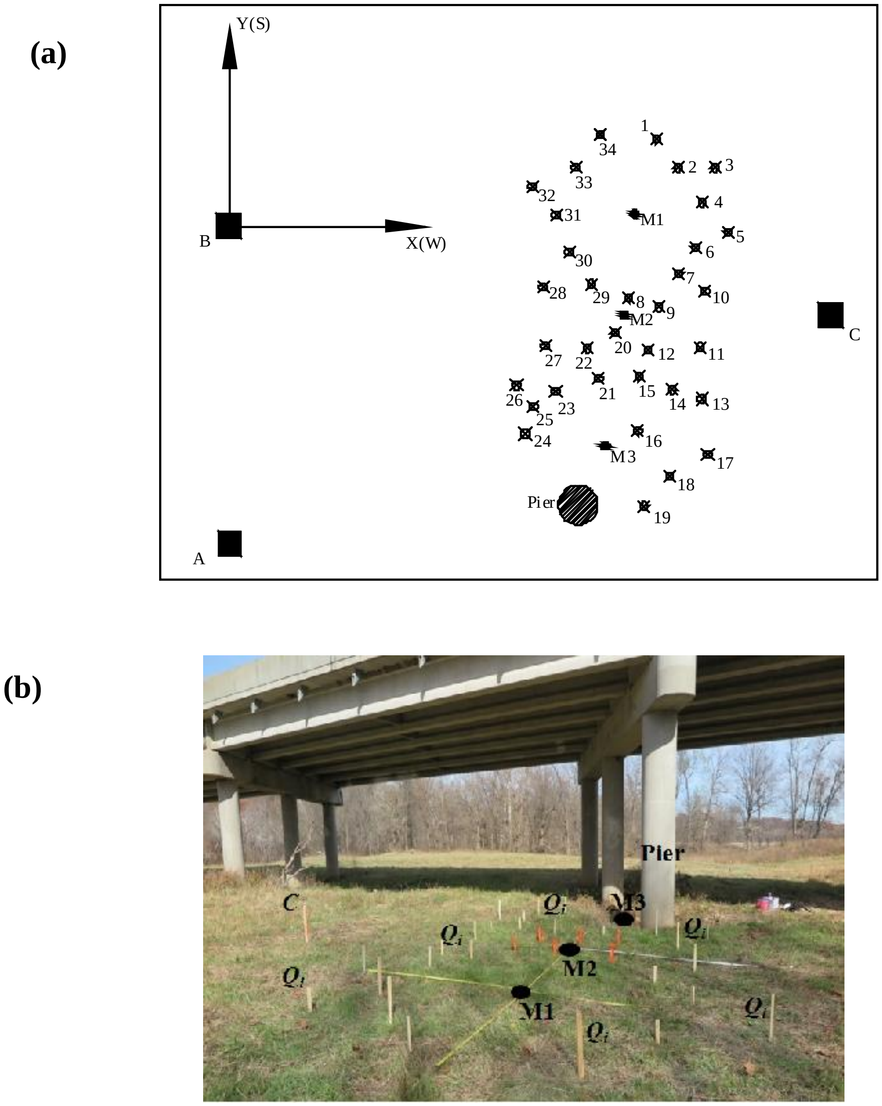

Figure 4.6. Test setup at the bridge site: (a) schematic view of smart rock and sensor locations in plane and (b) layout of smart rocks and sensor head.

(2) *Select the Locations of Smart Rocks and Sensor Head.* As shown in Figure 4.6(a, b), the smart rocks were located from far away to close to the bridge pier in order to understand the variation of the ambient magnetic field, the angles, and the total magnetic field. Magnet locations, M1, M2 and M3, were marked by inserting bottle caps

into the ground for easy placement of smart rocks on the ground and convenient collection of coordinates. The 34 wooden poles, Q_1 to Q_{34}, were distributed around the M1, M2 and M3 and bounded between the circles with diameter of 1.5 m and 5 m in order to avoid the dead zone of the magnetometer at each location of smart rocks. Three measurement tapes crossed at M1 and M2 were displayed to assist in the estimation of distance between a magnet and the sensor head.

(3) *Select a Calibration Point C for AMFOD*. A fixed object was needed to assist in the final determination of angle φ. As such, Point *C* indicated in Figure 4.6(a, b) marked by a tall wooden pole was selected out of the range of 34 measurement points. The selection of Point *C* was to ensure that the light from the horizontal laser pointer 2 can reach the wooden pole at Point C when the AMFOD was stationed at each sensor point.

(4) *Determine the Coordinates of Smart Rocks, Sensor Head and Calibration Point*. A total station was used to survey the coordinates of various points at the test site. Throughout the tests, one person operated the total station and another person held one prism as seen in Figure 4.7 to ensure the consistent accuracy of coordinate measurements. For each survey, the bottom center of the prism was aligned with the center of the top of the wooden pole and bottle caps since the magnetic field intensity is very sensitive to Z-coordinate.

Figure 4.7. Total station and prism for positioning.

(5) *Measure θ and φ*. As shown in Figure 4.8, the AMFOD was placed at one measurement point by aligning the center of its tripod to the top center of the plastic pole, in which the center of the high-precision APSS should be kept along the extension line of the plastic pole by adjusting the tripod with the high precision bubble level attached on the horizontal disk of the AMFOD. At each measurement point, the tripod was first adjusted horizontally without presence of the high-precision APSS. That is, after the horizontal Laser 2 was switched on, the tripod was rotated until the shooting light hit on the wooden pole at Point C and immediately locked at that position. The high-precision APSS was then put back to the tapered support. After the inside ball with a magnet was automatically aligned to the ambient magnetic field in several seconds, Laser 1 was switched on and its supporting ring was manually turned vertically, in combination with horizontal adjustment by the tunable disk, to facilitate the light going through the hole at the center line of the high-precision APSS and hit on the center of the laser acceptor. Finally, the two lasers were switched off and the two angles θ and φ can be read from the digital marks on the vertical ring and horizontal disk, respectively. The above process was repeated for all 34 points.

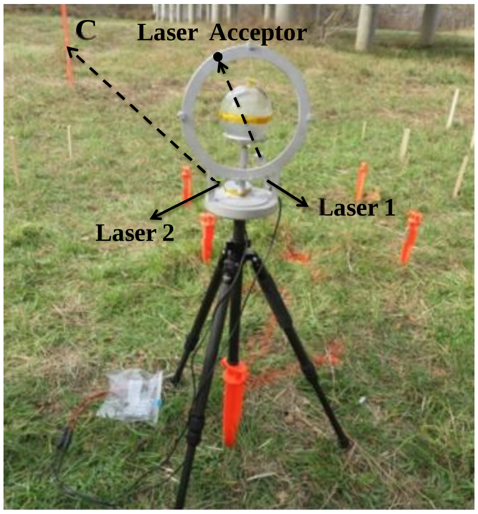

Figure 4.8. AMFOD setup and operational mechanism.

(6) *Measure the Ambient Magnetic Field Intensity*. One sensor head of the magnetometer was faced on the ground and ensured to be perpendicular to the ground by a bubble level attached onto the sensor head as shown in Figure 4.9. It is noted that a 57.7

cm wooden stick fastened onto the sensor head was to keep the center of the sensor head the same location at the center of the high-precision APSS in the AMFOD so that the magnetometer and the AMFOD provided the corresponding magnitude and direction of the ambient magnetic field vector, respectively. In addition, measurements should be made when there are no vehicles on the bridge deck to avoid any potential interference. At each point, at least three measurements were taken to ensure accuracy and repeatability.

Figure 4.9. Magnetometer setup and operation.

(7) *Measure the Total Magnetic Field Intensity of APSS at M1, M2 and M3*. The APSS smart rock was placed at each point M1, M2 or M3 as seen in the Figure 4.10. The center of the magnet was aligned with the center of the bottle cap at each point. The total magnetic field was generated by the magnet and the ambient magnetic field. The same setup of the magnetometer stated in Step (6) was applied and repeated to measure the total magnetic field intensity for the APSS at M1, M2 and M3, respectively.

Figure 4.10. APSS deployment: (a) M1$_{APSS}$ or M2$_{APSS}$ and (b) APSS at M3.

(8) *Measure the Total Magnetic Field Intensity of AOS at M1, M2 and M3.* In this final step, the AOS was placed at point M1, M2 and M3 as shown in Figure 4.11. The center of the plastic box with the centered magnet was kept in alignment with the center of the bottle cap at each point. The same setup of the magnetometer stated in Step (6) was applied and repeated to measure the total magnetic field intensity for all the AOS at M1, M2 and M3.

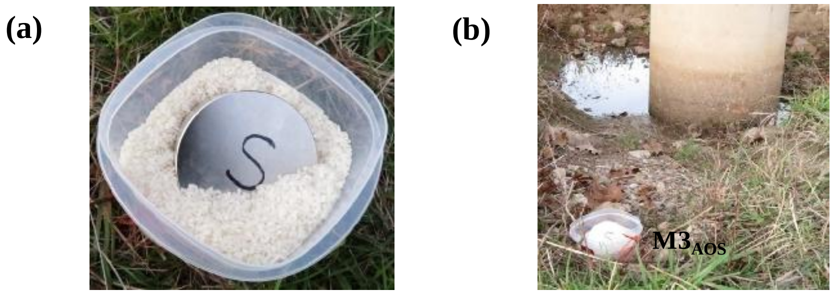

Figure 4.11. AOS deployment: (a) $M1_{AOS}$ or $M2_{AOS}$ and (b) AOS at M3.

4.7. TEST RESULTS AND DISCUSSION

In this section, the ambient magnetic field intensity at each measurement point was calculated through geometrical calculations based on collected data. Then the localization of AOS and APSS at three positions were evaluated and summarized.

4.7.1. Ambient Magnetic Field Intensity in XYZ Coordinate System.

The θ angle can be directly read from the digital marks on the vertical torus of the AMFOD. However, the φ angle must be transformed from the directly measured angle φ' read from the digital marks on the horizontal turntable of the AMFOD and the φ_0 angle from the test setup in XYZ coordinate system. As shown in Figure 4.12, $\boldsymbol{B}_{Ai}^{Qi}$ denotes the ambient magnetic field vector at measurement point Q_i in XOY plane, Q_iC represents the light of Laser 2 shooting to the wooden pole at Point C, the local coordinate system xQ_iy is parallel to the global coordinate system of XOY, and φ' in [0, π] is the angle spanned from the extension of vector $-\boldsymbol{B}_{Ai}^{Qi}$ to the line Q_iC in counterclockwise direction. Therefore, the direction of the ambient magnetic field φ in [0, 2π] in XOY plane is equal to $\pi-\varphi'+\varphi_0$, where φ_0 in [0, 2π] is the angle between line Q_iC and X-axis counterclockwise and equal to $\arctan[(Y_C-Y_{Qi})/(X_C-X_{Qi})]$.

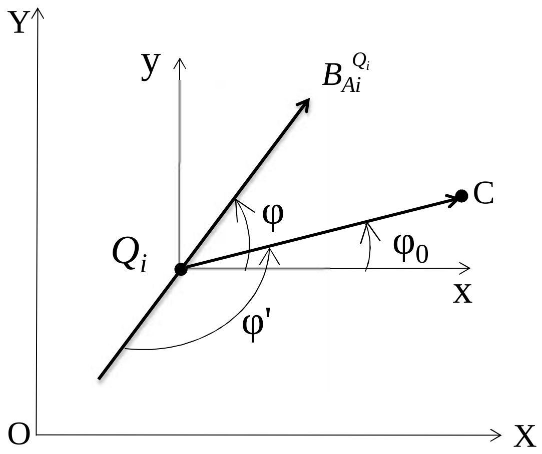

Figure 4.12. Angle adjustment.

Table 4.1 summarizes the coordinates of 34 sensor locations in the O-XYZ coordinate system, the direction of the ambient magnetic field vector, and the ambient magnetic field intensities at each measurement point.

Table 4.1. Sensor coordinates and ambient magnetic field intensities

Measurement Point	Sensor Coordinates (m)			Ambient Magnetic Field Direction (rad)		Ambient Magnetic Field Intensity (10^4 nT)			
	X_i	Y_i	Z_i	θ_i	φ_i	B_{Ai}	B_{AXi}	B_{AYi}	B_{AZi}
C	15.28	-2.26	N/A	N/A	N/A	N/A	N/A	N/A	N/A
Q_1	10.88	2.20	-0.55	1.21	1.50	5.080	0.121	1.775	5.080
Q_2	11.43	1.48	-0.45	1.22	1.53	5.142	0.081	1.757	5.142
Q_3	12.37	1.48	-0.58	1.22	1.48	5.136	0.164	1.749	5.136
Q_4	12.04	0.59	-0.48	1.20	1.49	5.137	0.160	1.867	5.137
Q_5	12.70	-0.16	-0.51	1.20	1.51	5.130	0.110	1.877	5.130
Q_6	11.87	-0.54	-0.59	1.19	1.45	5.136	0.230	1.893	5.136
Q_7	11.45	-1.21	-0.61	1.18	1.29	5.147	0.539	1.895	5.147
Q_8	10.17	-1.84	-0.71	1.15	1.28	5.195	0.616	2.021	5.195
Q_9	10.94	-2.07	-0.72	1.14	1.37	5.179	0.425	2.105	5.179
Q_{10}	12.12	-1.66	-0.70	1.15	1.34	5.135	0.486	2.048	5.135
Q_{11}	11.99	-3.08	-0.62	1.13	1.42	5.169	0.324	2.177	5.169
Q_{12}	10.67	-3.16	-0.73	1.13	1.50	5.256	0.169	2.248	5.256
Q_{13}	12.03	-4.40	-0.80	1.13	1.36	5.205	0.478	2.189	5.205
Q_{14}	11.28	-4.17	-0.70	1.12	1.29	5.274	0.643	2.195	5.274
Q_{15}	10.44	-3.83	-0.70	1.11	1.38	5.337	0.455	2.321	5.337
Q_{16}	11.40	-5.22	-0.72	1.16	1.34	5.332	0.487	2.070	5.332
Q_{17}	12.19	-5.82	-0.54	1.14	1.31	5.240	0.571	2.114	5.240
Q_{18}	11.22	-6.36	-0.56	1.15	1.14	5.414	0.937	2.012	5.414

Table 4.1. Sensor coordinates and ambient magnetic field intensities (cont.)

Q_{19}	10.57	-7.12	-0.60	1.16	1.13	5.592	0.959	2.043	5.592
Q_{20}	9.82	-2.72	-0.70	1.14	1.28	5.273	0.637	2.101	5.273
Q_{21}	9.41	-3.88	-0.81	1.13	1.29	5.462	0.662	2.256	5.462
Q_{22}	9.12	-3.12	-0.75	1.12	0.94	5.357	1.375	1.883	5.357
Q_{23}	8.31	-4.22	-0.56	1.11	1.33	5.565	0.585	2.387	5.565
Q_{24}	7.54	-5.29	-0.70	1.10	1.60	5.903	-0.075	2.661	5.903
Q_{25}	7.75	-4.59	-0.92	1.10	1.53	5.732	0.107	2.618	5.732
Q_{26}	7.32	-4.06	-0.79	1.13	1.41	5.530	0.381	2.341	5.530
Q_{27}	8.04	-3.05	-0.61	1.13	1.24	5.357	0.749	2.172	5.357
Q_{28}	7.99	-1.55	-0.69	1.14	1.33	5.205	0.521	2.095	5.205
Q_{29}	9.22	-1.48	-0.69	1.19	1.27	5.194	0.577	1.841	5.194
Q_{30}	8.65	-0.66	-0.79	1.19	1.30	5.160	0.516	1.854	5.160
Q_{31}	8.32	0.28	-0.76	1.16	1.43	5.136	0.296	2.035	5.136
Q_{32}	7.71	1.01	-0.63	1.14	1.46	5.133	0.237	2.123	5.133
Q_{33}	8.81	1.49	-0.72	1.14	1.51	5.133	0.126	2.125	5.133
Q_{34}	9.46	2.32	-0.44	1.16	1.41	5.142	0.326	2.016	5.142

4.7.2. AOS Localization. Table 4.2 gives the measured coordinates (X, Y, Z) and measured total magnetic field intensities ($B_i^{(M)}$) at 18 sensor points when the AOS is located at M1, which was compared with the predicted location using the measured coordinates of sensor points. Table 4.3 and Table 4.4 provide similar results when the AOS is located at M2 and M3. Overall, it can be observed from the test results at M1, M2, and M3 that the SRSS prediction error ranges from 9.3 cm to 15.4 cm, which is quite small in comparison with the diameter of smart rocks (approximately 30 cm).

Table 4.2. Predicted and measured location of the AOS: $M1_{AOS}$

Location of Sensor Head	X_i (m)	Y_i (m)	Z_i (m)	$B_i^{(M)}$ (10^4 nT)
Q_1	10.88	2.20	-0.52	5.356
Q_2	11.43	1.48	-0.42	5.277
Q_3	12.37	1.48	-0.55	4.975
Q_4	12.04	0.59	-0.45	4.790
Q_5	12.70	-0.16	-0.48	4.890
Q_6	11.87	-0.54	-0.56	4.590
Q_7	11.45	-1.21	-0.58	4.686
Q_8	10.17	-1.84	-0.68	4.863
Q_9	10.94	-2.07	-0.69	4.967
Q_{10}	12.12	-1.66	-0.67	4.957
Q_{20}	9.82	-2.72	-0.67	5.154

Table 4.2. Predicted and measured location of the AOS: M1$_{\text{AOS}}$ (cont.)

Q_{29}	9.22	-1.48	-0.66	4.815
Q_{30}	8.65	-0.66	-0.76	4.770
Q_{31}	8.32	0.28	-0.73	5.050
Q_{32}	7.71	1.01	-0.60	5.134
Q_{33}	8.81	1.49	-0.69	5.491
Q_{34}	9.46	2.32	-0.41	5.454
Predicted Location M1$_{\text{AOS}}$	10.26	0.24	-1.46	N/A
Measured Location M1$_{\text{AOS}}$	10.33	0.30	-1.42	
Location Prediction Error for M1$_{\text{AOS}}$	-0.06	-0.07	-0.03	
SRSS Error in Coordinate	0.10 m			

Table 4.3. Predicted and measured location of the AOS: M2$_{\text{AOS}}$

Location of Sensor Head	X_i (m)	Y_i (m)	Z_i (m)	$B_i^{(M)}$ (10^4 nT)
Q_4	12.04	0.59	-0.45	5.158
Q_5	12.70	-0.16	-0.48	5.104
Q_6	11.87	-0.54	-0.56	5.135
Q_7	11.45	-1.21	-0.58	5.129
Q_{10}	12.12	-1.66	-0.67	4.882
Q_{11}	11.99	-3.08	-0.59	4.817
Q_{13}	12.03	-4.40	-0.77	5.137
Q_{14}	11.28	-4.17	-0.67	5.116
Q_{15}	10.44	-3.83	-0.67	4.926
Q_{16}	11.40	-5.22	-0.69	5.306
Q_{21}	9.41	-3.88	-0.78	5.112
Q_{23}	8.31	-4.22	-0.53	5.425
Q_{25}	7.75	-4.59	-0.89	5.654
Q_{26}	7.32	-4.06	-0.76	5.445
Q_{27}	8.04	-3.05	-0.58	5.178
Q_{28}	7.99	-1.55	-0.66	5.371
Q_{30}	8.65	-0.66	-0.76	5.635
Q_{31}	8.32	0.28	-0.73	5.284
Predicted Location M2$_{\text{AOS}}$	9.93	-2.21	-1.56	N/A
Measured Location M2$_{\text{AOS}}$	10.05	-2.28	-1.48	
Location Prediction Error for M2$_{\text{AOS}}$	-0.12	0.06	-0.08	
SRSS Error in Coordinate	0.15 m			

Table 4.4. Predicted and measured location of the AOS: M3$_{\text{AOS}}$

Location of Sensor Head	X_i (m)	Y_i (m)	Z_i (m)	$B_i^{(M)}$ (10^4 nT)
Q_9	10.94	-2.07	-0.67	5.265
Q_{12}	10.67	-3.16	-0.68	5.466
Q_{13}	12.03	-4.40	-0.75	5.210
Q_{14}	11.28	-4.17	-0.65	5.381
Q_{15}	10.44	-3.83	-0.65	5.715
Q_{17}	12.19	-5.82	-0.49	5.139
Q_{18}	11.22	-6.36	-0.51	5.075
Q_{19}	10.57	-7.12	-0.55	5.299
Q_{20}	9.82	-2.72	-0.65	5.493
Q_{21}	9.41	-3.88	-0.76	6.251
Q_{23}	8.31	-4.22	-0.51	5.936
Q_{25}	7.75	-4.59	-0.87	5.952
Q_{26}	7.32	-4.06	-0.74	5.664
Q_{27}	8.04	-3.05	-0.56	5.540
Predicted Location M3$_{\text{AOS}}$	9.51	-5.52	-1.86	N/A
Measured Location M3$_{\text{AOS}}$	9.58	-5.58	-1.84	
Location Prediction Error for M3$_{\text{AOS}}$	-0.06	0.06	-0.02	
SRSS Error in Coordinate	0.09 m			

4.7.3. APSS Localization. Table 4.5 gives the measured coordinate (X, Y. Z) and total magnetic field intensities ($B_i^{(M)}$) at 18 sensor points when the APSS is located at M1, which was compared with the predicted location using the measured coordinates of sensor points. Table 4.6 and Table 4.7 provide similar results when the APSS is located at M2 and M3. Similar to the AOS case, the prediction location error of the magnet ranges from 8.5 cm to 18 cm. Once again, this range of errors is small compared with the size of smart rocks, demonstrating satisfactory accuracy in smart rock localization for bridge scour monitoring.

Table 4.5. Predicted and measured location of the APSS: M1$_{\text{APSS}}$

Location of Sensor Head	X_i (m)	Y_i (m)	Z_i (m)	$B_i^{(M)}$ (10^4 nT)
Q_1	10.88	2.20	-0.52	5.812
Q_2	11.43	1.48	-0.42	5.695

Table 4.5. Predicted and measured location of the APSS: $\mathrm{M1}_{\mathrm{APSS}}$ (cont.)

Q_3	12.37	1.48	-0.55	5.181
Q_4	12.04	0.59	-0.45	4.972
Q_5	12.70	-0.16	-0.48	4.989
Q_6	11.87	-0.54	-0.56	4.797
Q_7	11.45	-1.21	-0.58	4.973
Q_8	10.17	-1.84	-0.68	5.213
Q_9	10.94	-2.07	-0.69	5.206
Q_{10}	12.12	-1.66	-0.67	5.094
Q_{20}	9.82	-2.72	-0.67	5.300
Q_{28}	7.99	-1.55	-0.66	5.146
Q_{29}	9.22	-1.48	-0.66	5.103
Q_{30}	8.65	-0.66	-0.76	4.891
Q_{31}	8.32	0.28	-0.73	4.949
Q_{32}	7.71	1.01	-0.60	5.119
Q_{33}	8.81	1.49	-0.69	5.524
Q_{34}	9.46	2.32	-0.41	5.642
Predicted Location $\mathrm{M1}_{\mathrm{APSS}}$	10.25	0.45	-1.35	N/A
Measured Location $\mathrm{M1}_{\mathrm{APSS}}$	10.33	0.30	-1.41	
Location Prediction	-0.08	0.15	0.06	
SRSS Error in Coordinate	0.18 m			

Table 4.6. Predicted and measured location of the APSS: $\mathrm{M2}_{\mathrm{APSS}}$

Location of Sensor Head	X_i (m)	Y_i (m)	Z_i (m)	$B_i^{(M)}$ (10^4 nT)
Q_4	12.04	0.59	-0.45	5.218
Q_5	12.70	-0.16	-0.48	5.173
Q_6	11.87	-0.54	-0.56	5.289
Q_7	11.45	-1.21	-0.58	5.485
Q_{10}	12.12	-1.66	-0.67	5.097
Q_{11}	11.99	-3.08	-0.59	4.924
Q_{13}	12.03	-4.40	-0.77	5.171
Q_{14}	11.28	-4.17	-0.67	5.188
Q_{15}	10.44	-3.83	-0.67	5.137
Q_{16}	11.40	-5.22	-0.69	5.332
Q_{21}	9.41	-3.88	-0.78	5.382
Q_{23}	8.31	-4.22	-0.53	5.475

Table 4.6. Predicted and measured location of the APSS: M2$_{\text{APSS}}$ (cont.)

Q_{25}	7.75	-4.59	-0.89	5.707
Q_{26}	7.32	-4.06	-0.76	5.473
Q_{27}	8.04	-3.05	-0.58	5.134
Q_{28}	7.99	-1.55	-0.66	5.233
Q_{30}	8.65	-0.66	-0.76	5.535
Q_{31}	8.32	0.28	-0.73	5.277
Predicted Location M2$_{\text{APSS}}$	9.96	-2.20	-1.43	N/A
Measured Location M2$_{\text{APSS}}$	10.05	-2.28	-1.47	
Location Prediction Error for M2$_{\text{APSS}}$	-0.09	0.08	0.04	
SRSS Error in Coordinate	0.13 m			

Table 4.7. Predicted and measured location of the APSS: M3$_{\text{APSS}}$

Location of Sensor Head	X_i (m)	Y_i (m)	Z_i (m)	$B_i^{(M)}$ (10^4 nT)
Q_9	10.94	-2.07	-0.66	5.277
Q_{11}	11.99	-3.08	-0.56	5.242
Q_{12}	10.67	-3.16	-0.67	5.520
Q_{13}	12.03	-4.40	-0.74	5.253
Q_{14}	11.28	-4.17	-0.64	5.493
Q_{15}	10.44	-3.83	-0.64	5.879
Q_{16}	11.40	-5.22	-0.66	5.311
Q_{17}	12.19	-5.82	-0.48	5.161
Q_{18}	11.22	-6.36	-0.50	5.117
Q_{19}	10.57	-7.12	-0.54	5.245
Q_{20}	9.82	-2.72	-0.64	5.516
Q_{21}	9.41	-3.88	-0.75	6.373
Q_{23}	8.31	-4.22	-0.50	5.920
Q_{25}	7.75	-4.59	-0.86	5.835
Q_{26}	7.32	-4.06	-0.73	5.609
P_{27}	8.04	-3.05	-0.55	5.520
Predicted Location M3$_{\text{APSS}}$	9.53	-5.52	-1.85	N/A
Measured Location M3$_{\text{APSS}}$	9.58	-5.58	-1.82	
Location Prediction Error for M3$_{\text{APSS}}$	-0.05	0.06	-0.03	
SRSS Error in Coordinate	0.08 m			

4.8. SUMMARY

In this section, efforts were made to develop the localization mechanism for a single smart rock with the APSS and AOS deployed at the bridge site of US Highway 63 over the Gasconade River. The localization mechanism is to establish a function between the location of the smart rock and the total magnetic field intensity. The location of the smart rock can then be determined through an optimization algorithm by comparing the total magnetic field intensity calculated from the function with the actual total magnetic field intensity directly measured by the G858 magnetometer.

The total magnetic field consists of the magnetic field generated by a permanent magnet inside the smart rock, the Earth and any other ferromagnetic substances such as the reinforcement in bridge piers and deck. The mathematic model of the magnetic field for the magnet is known. However, the distribution of the combined Earth and other ferromagnetic substances referred as the non-uniform ambient magnetic field is unknown. Therefore, a custom-built device named AMFOD was developed to detect the orientation and the G858 magnetometer was used to collect the intensity of the ambient magnetic field.

Finally, the experimental field test at the bridge site of US Highway 63 over the Gasconade River was designed and carried out to demonstrate the localization procedure and validate the localization algorithm for the AOS and APSS. The results show that the localization errors were small compared to the size of smart rocks and the achieved accuracy for smart rock localization satisfactorily met the design requirements. The known orientation of the APSS made the localization mechanism and procedure greatly simpler than the AOS, thus a better choice for practical applications.

5. FIELD IMPLEMENTATION AT THREE BRIDGE SITES

5.1. INTRODUCTION

In this section, the smart rock technology proposed and developed in Sections 2-4 is further validated at three bridge sites for real-time monitoring of scour depth or riprap effectiveness. The three bridge sites tested are Highway 1 over the Waddell Creek (Br. No. 36-0065) in California, I-44W Highway over the Roubidoux Creek (Br. No. L0093) and US Highway 63 over the Gasconade River (Br. No. A3760) in Missouri.

In Section 4, the localization algorithm was validated with field measurements from a river bank. The three components of the ambient magnetic field due to the effect of the Earth and bridge pier/deck at all measurement points were obtained from the specially-designed Ambient Magnetic Field Orientation Device (AMFOD). In this section, all measurements are taken from the bridge deck considering the high potential for flooding at the river bank during a flood event, making the use of the AMFOD impractical. In this case, the smart rocks with automatically pointing upward system (APUS) finalized for the three bridges in Section 2 are deployed around the scour critical piers in order to generate strong magnetic fields in vertical direction for remote measurement. The three components of the ambient magnetic field and the total magnetic field are measured using a newly-acquired digital 3-axis magnetometer instead of the G858 magnetometer and AMFOD used in Section 4. A direct measurement of the three components of a magnetic field with the new magnetometer increases the operation efficiency and the accuracy of localization in bridge applications. As they are measured, the magnetic field intensities can be graphically viewed in real time on a computer with the special software to go with the new magnetometer. This capability allows a real time check on the quality of measured data during tests at bridge sites. In addition, a test crane that can be installed on a truck and is moved on the bridge deck was designed and manufactured to support the magnetometer sensor for measurements as close to the deployed smart rock as possible above water. The stronger the measured magnetic field intensity, the more accurate the identified location of the smart rock.

5.1.1. The 3-Axis Flux Magnetometer. A digital 3-axis magnetometer system as shown in Figure 5.1, manufactured by STL Systemtechnik Ludwig GmBH in

Konstanz, Germany, was used for this study. It is composed of a digital sensor DM050, a three-channel coax Ethernet hub, a 50 m coax cable for power and data transmission, and a notebook with STL GradMag software installed for full control of measurement, data acquisition and graphical display. The DM050 is a precision magnetometer with 0.002 nT resolution, less than 0.06 nT/ √ Hz noise and a field range of ±1 mT. It measures three orthogonal field components at a maximum sample rate of 10 kHz. The software also offers the total field as an extra virtual channel. Typical sources of errors due to axis misalignment, scaling, offset and phase are eliminated to the greatest extent possible with a digital signal conditioning strategy. The software offering full control over all system features, real-time monitoring of data and data documentation greatly improves the efficiency of field data analysis and display.

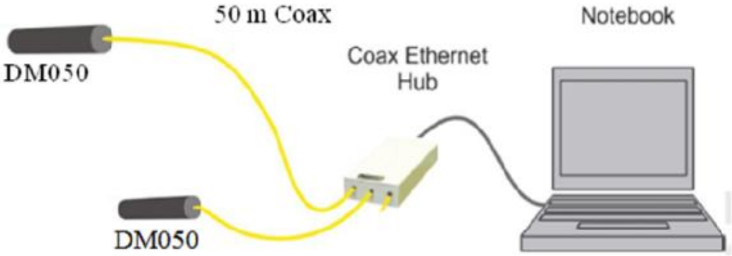

Figure 5.1. The STL digital 3-axis flux magnetometer system.

5.1.2. The Lightweight Test Crane. In the design of a new frame to facilitate field tests, the following factors were taken into account: stiffness, lightweight, ease in installation, rapid assembling, and cost effectiveness. The frame must be sufficiently stiff to minimize the wind induced disturbance on measurement during field tests. As shown in Figure 5.2, the frame mainly consists of four components: 1 to 4. Comp.1 is a lower horizontal beam that supports a sensor head for magnetic field intensity measurement and two non-magnetic prisms for the coordinate determination of the sensor. Comp. 2 is a vertical column that allows the access to the measurement points as close to the water surface as possible in field application. Comp. 3 is an upper horizontal beam that functions as an outrigger and support for the column. Comp. 4 is a forklift that allows the three directional movement of the sensor head. In addition, Figure 5.2 includes balanced weights (Comp. 5) as needed.

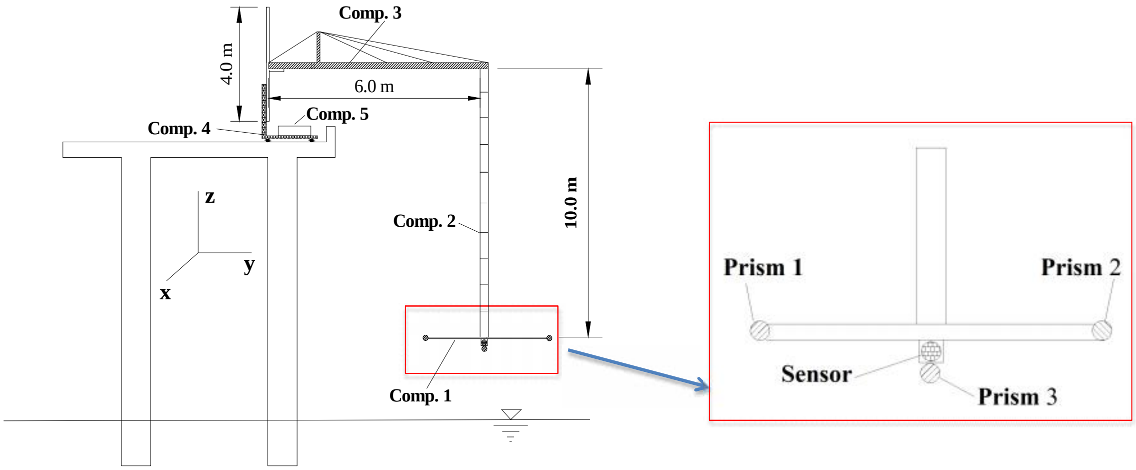

Figure 5.2. Schematic view of test crane.

Comp.1 is made of carbon fibers that have a low density of 1800 kg/m^3 and a high modulus of elasticity of 240 GPa compared to other non-magnetic materials. Comp. 2 is made of modular carbon fiber tubes (1 m in length) that are designed to minimize flexural deformation and resist potential vibration caused by the wind load. The standard tubes can be connected to any required length in field application. Comp. 3 is made of aluminum alloy with a density of 2700-2810 kg/m^3 and a modulus of elasticity of 71 GPa. A balanced weight is applied as needed to ensure that Comp.3 remains horizontal during tests. All the components can be rapidly assembled at a test site. The forklift can be installed on a trailer and pulled by a truck. It is operated manually in this study but could be automatically controlled as needed from a remote site in the future. The test crane is most appropriate for a bridge deck that is less than 10 m above water. The outrigger can laterally extend up to 5 m from the bridge deck. The forklift allows a vertical movement of up to 4 m. The test crane can move any distance as needed along the traffic direction.

5.2. I-44W ROUBIDOUX CREEK BRIDGE

In this section, the I-44W Roubidoux Creek Bridge (No. L0039) in Waynesville, MO, was used as the first test site to validate the performance of a smart rock. The bridge is a ten-span, steel-girder structure to support two lanes of westbound traffic on Interstate 44. As shown in Figure 5.3, Pier 7 is located in the main flow of the channel and its downstream side is scour critical. Three series of field tests were carried out in different seasons to validate the localization and accumulated movement of the smart rock between flood events or during normal water flow.

The overall setup for three field tests is the same. One smart rock with two stacked magnets in the APUS was deployed around the downstream side of Pier 7 during the first field test and remain in place during the second and third field tests. The test crane was applied to facilitate the three-dimensional movement of a 3-axis flux magnetometer around the deployed smart rock. The magnetometer sensor head mounted on the test crane was used to measure the magnetic field. Meanwhile, a prism mounted on the crane in proximity to the magnetometer sensor head was surveyed from a total station to collect the coordinate of each measurement point. In addition, a sonar instrument was installed on the side of a small boat and employed to map the river bed profile around Pier 7. Finally, the smart rock was located and compared based on the magnetic field data and measurement point coordinates.

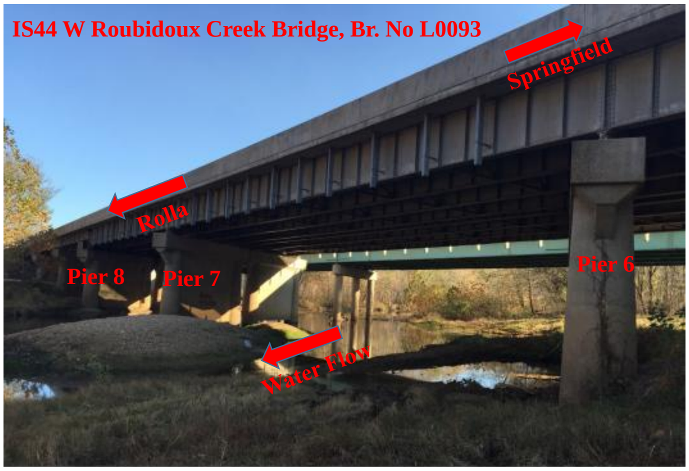

Figure 5.3. The overview of I-44 W Roubidoux Creek Bridge.

5.2.1. Test Setup and Layout. As shown in Figure 5.4(a, b), the test crane and the magnetic field measurement system were set up on the bridge shoulder near Bent 7. A total station was set on ground near Bent 8 to survey the smart rock and the magnetometer sensor head as ground true coordinate data. Its position was used as the origin of a Cartesian coordinate system O-XYZ with X-, Y-, and Z-axles oriented in transverse, longitudinal (traffic direction), and vertical (upward) directions, respectively, following the right-hand rule. The smart rock, SR1, was deployed around Bent 7. The test crane was fixed on a trailer towed by a truck. The magnetometer sensor mounted on the test crane was extended down from the bridge deck to measure the total magnetic field near the smart rock. Prism 3 mounted below the sensor as shown in Figure 5.4(d) was used to represent the coordinate of each measurement point. Prisms 1 and 2 were fixed at two ends of the horizontal bar of the test crane to ensure that the bar was in parallel with X axis. The measurement points in XOY plane were selected as the cross points in Mesh 1 as shown in Figure 5.4(a). They were translated to the corresponding forklift locations on the bridge deck as illustrated in Figure 5.4(c). Through the test crane, the longitudinal, transverse and vertical positions of the measurement points corresponded to Stop (S1-S3) and Path (P1 and P2) of a flatbed trailer on the bridge deck as well as Elevation (E1-E7). Therefore, each truck stop and forklift elevation is uniquely defined by a designation of SrPsEt where r, s, and t are three integers. For each SrPsEt, the coordinate of the magnetometer sensor and the magnetic field were measured simultaneously.

5.2.2. Test Procedure. (1) *Set the XYZ coordinate system*. As shown in Figure 5.5, a proper location for the total station was selected near Bent 8 for its line of sight to the magnetometer sensor, which is designated as Point O or the origin of the coordinate system. The Y-axis pointing to Springfield was selected to be the longitudinal (traffic) direction of the straight bridge deck, passing through Point O. The X-axis is perpendicular to the Y-axis and pointing to downstream in the horizontal plane, and the Z-axis is pointing up. A permanent point A (Benchmark) on Pier 9 was surveyed at each field test for reference and translation from the measurement points in O-XYZ to the coordinates selected during the first series of field tests.

(2) *Assemble the test crane*. As shown in Figures 5.4(b), the forklift was first set and tied to an open flat trailer. The horizontal aluminum arm was then installed and followed by an assembling of nine segments of carbon fiber tubes with 1.0 m each to lower down the measurement points from the bridge deck. Finally, the horizontal bar was connected at the bottom of the carbon tube to support the magnetometer sensor and prisms for coordinate measurement.

(3) *Set up the STL digital magnetometer*. As shown in Figure 5.4(b), the laptop installed with special software for the sensor control and measurement of magnetic fields. An Ethernet cable was used to transmit the signal from the sensor to the laptop by an

interface called mini Ethernet box. Two batteries were used to power the sensor and laptop, respectively.

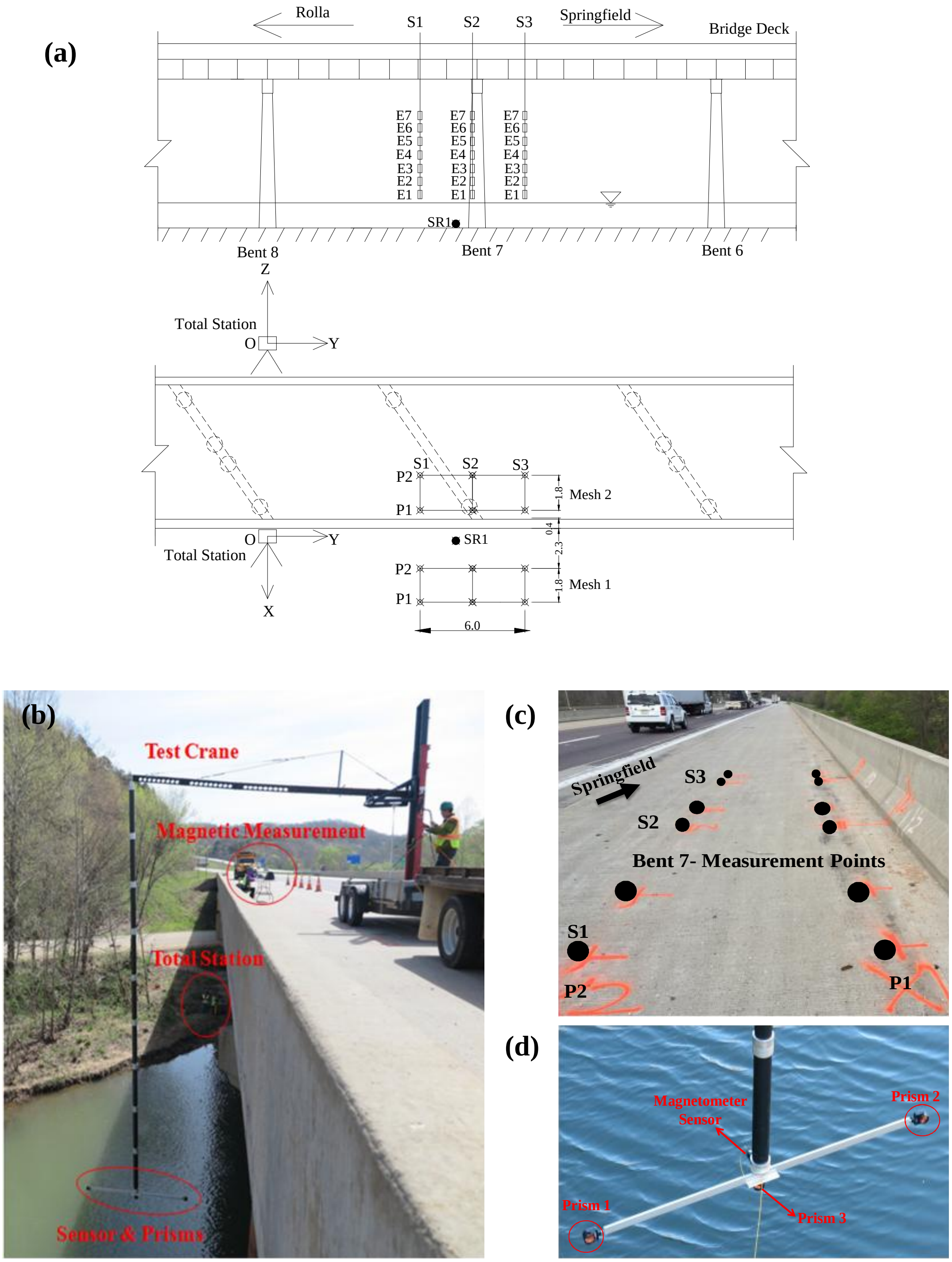

Figure 5.4. I-44W Roubidoux Creek bridge: (a) planning (unit: m), (b) test setup, (c) forklift positions, and (d) sensor and prisms locations.

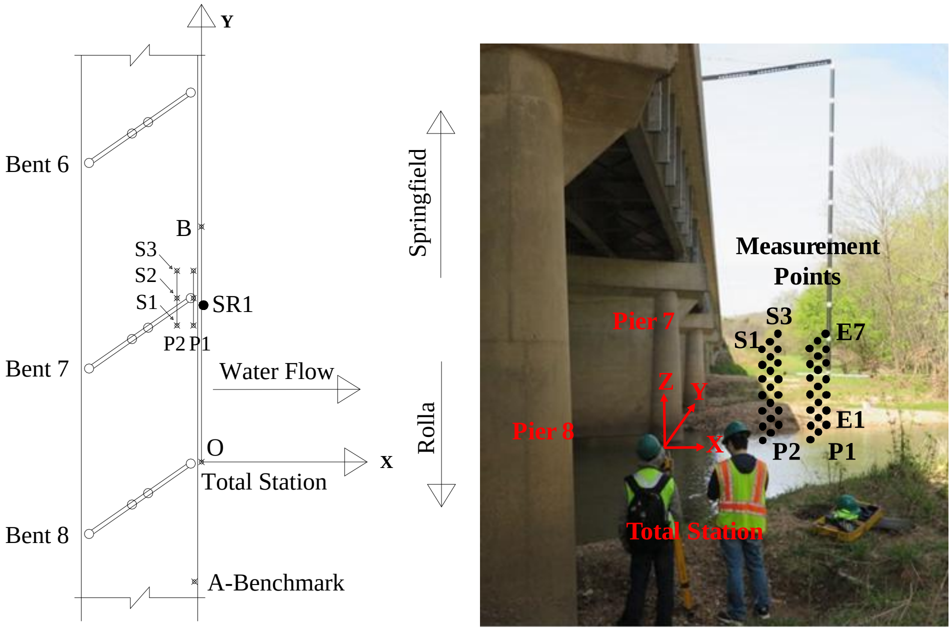

Figure 5.5. Selection of the Cartesian coordinate system.

(4) *Measure the ambient magnetic field*. The ambient magnetic field is generated by the Earth and nearby ferromagnetic objects. It was measured prior to the deployment of smart rock during the first field test. As indicated in Figure 5.4(a, b, d), the trailer ran two paths (X coordinates) on the bridge deck and three stops (Y coordinates). At each stop, seven elevations (Z coordinates) were selected by moving up and down the horizontal beam of the test crane by 0.3 m. Figure 5.5(b) illustrates all the measurement points in space. Figure 5.6 (a) illustrates one stop when the two rear tires of the trailer were parked at the marked location and the forklift was positioned at P2S3. At each stop, measurements (both coordinate and magnetic field intensity) were taken at seven elevations in Z direction. Therefore, a total of 42 measurements were taken following the measurement sequence as indicated in Figure 5.6(b).

(5) *Deploy or inspect the smart rock and measure its coordinates***.** In the first series of field tests, a smart rock (SR1) with two stacked N42 magnets in the APUS configuration as shown in Figure 5.7 was deployed around the downstream side of Pier 7 as indicated in Figure 5.8(a). The smart rock was transported in a boat from the river bank and deployed at the predetermined site shown in Figure 5.8(b). The smart rock can be observed near Pier 7 with a connection rope floated on the water surface.

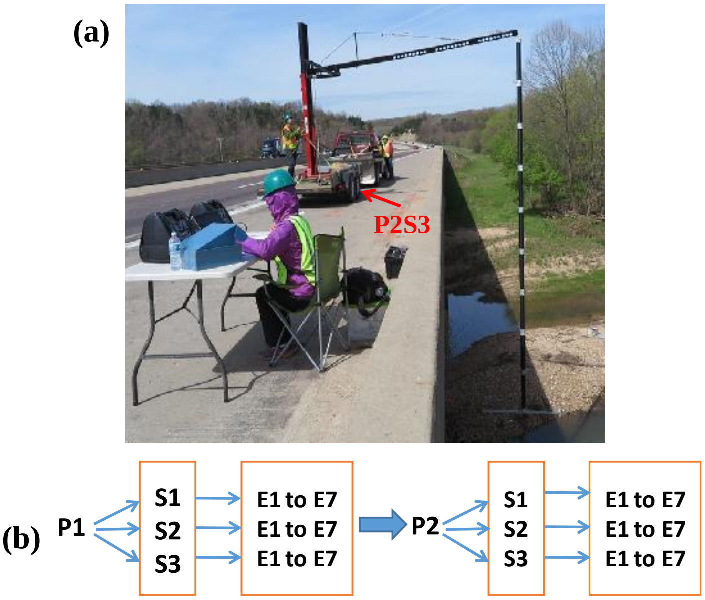

Figure 5.6. A snapshot of field measurement: (a) test crane located at P2S3 and (b) measurement point sequence.

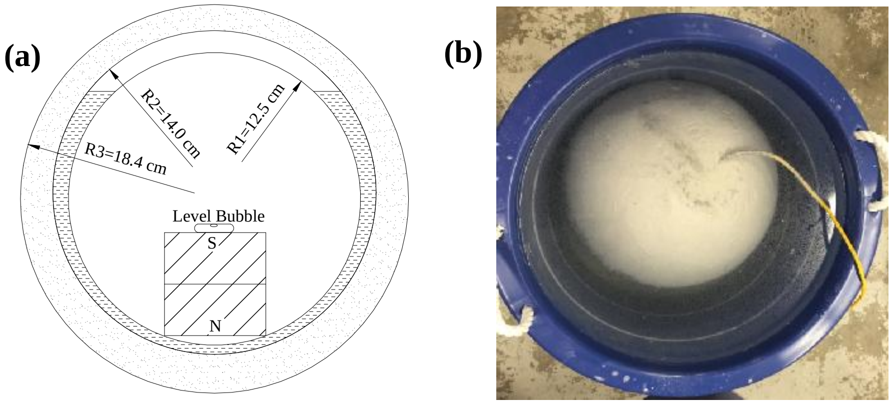

Figure 5.7. The APUS: (a) schematic view and (b) cast in smart rock.

During the second series of field tests, the smart rock, SR1, was inspected to ensure that it was rolled to the bottom of the scour hole around Pier 7. Indeed, it was found to have slightly moved from the original position when deployed during the first series of field tests.

During the third series of field tests, the smart rock, SR1, continued to be inspected to ensure that it remained in the scour hole around Pier 7. It was found to have slightly moved back to the original position during the first series of field tests.

The coordinates of the smart rock in its original and new positions during all three series of field tests were measured with a total station through the prism placed on top of the smart tock, as illustrated in Figure 5.8(c). These measured coordinates served as ground truth data in smart rock localization and validation.

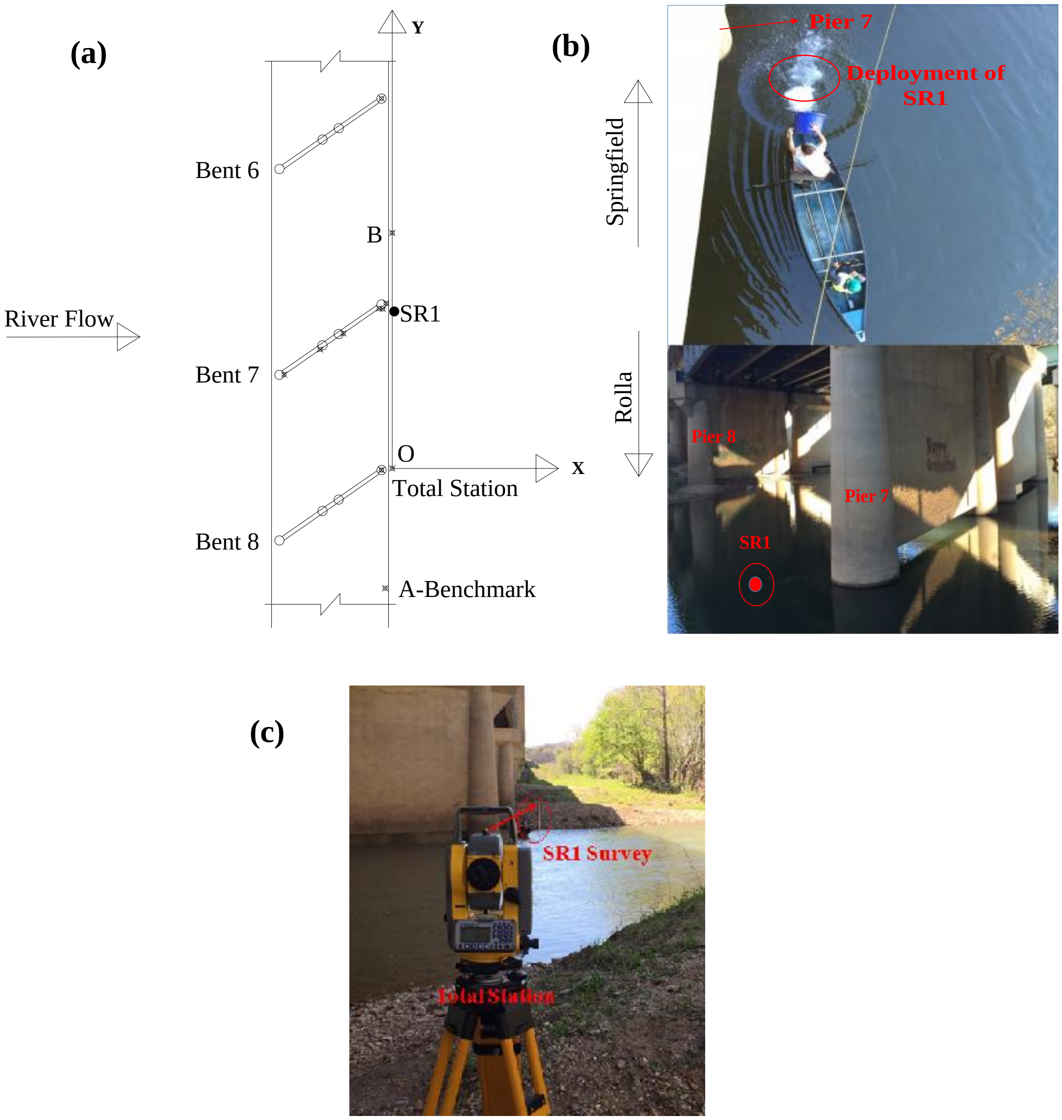

Figure 5.8. Applicaton of smart rock SR1: (a) location, (b) deployment, and (c) survey.

(6) *Measure the total magnetic field*. After the deployment of smart rock during the first series of field tests, the total magnetic field combining the effects of the smart rock and the ambient magnetic field was measured following the same procedure as used for the ambient magnetic field measurement. During the second and third series of field

tests, the total magnetic field was measured at 42 points around Pier 7 with the same measurement sequence as shown in Figure 5.6(b).

(7) *Measure the time-varying ambient magnetic field for reference.* The Earth's magnetic field and the magnetization of nearby ferromagnetic substances may change over time. To take this factor into account in the localization process of the smart rock, the time-varying property of the ambient magnetic field was characterized. Bent 5 is over 60 m away from Bent 7 and its surrounding magnetic field is not affected by the presence of the smart rock. Thus, Pier 5 (identical to Pier 7) was selected as a reference site for a study of potential change of the ambient magnetic field over time. One permanent point, P_5 represented by *(-1.02, 85.22, 0.44*) coordinates, was marked on Pier 5 as a reference for other nearby measurement points. To further separate the Earth's and others' magnetic fields, six measurement points, $P_{5\text{-}1}$, $P_{5\text{-}2}$, $P_{5\text{-}3}$, $P_{5\text{-}4}$, $P_{5\text{-}5}$, and $P_{5\text{-}6}$, were selected at the top of orange markers as shown in Figure 5.9. The magnitude of the ambient magnetic field for each point was measured by a scalar magnetometer G858. Note that Point $P_{5\text{-}6}$ represented by (*15.43, 88.55, 0.53*) coordinates is far away from Pier 5 and its magnetic field is affected by the presence of Pier 5. It was selected during the first series of field tests as a reference location for the Earth magnetic field intensity since the magnetic field intensities within 1 m of Point $P_{5\text{-}6}$ changed little. These measurements indicated little influence from the bridge pier or deck. Therefore, the measurement at Point $P_{5\text{-}6}$ represents the Earth's magnetic field only. Continuing measurements at Point $P_{5\text{-}6}$ shed light on any potential change of the Earth magnetic field between various field visits.

(8) *Map the riverbed profile***.** The 999ci HD KVD SI Combo/900 Series - Side sonar imaging instrument from Humminbird^{TM} Sonar as shown in Figure 5.10(a) was used to map the riverbed profile in the studied area. The instrument is based on the sonar mechanism to complete the HD side and down imaging. The side imaging can visualize any structures, timbers, wrecks, falling logs and fishes in the covered underwater area. The included GPS chart plotting with built-in Humminbrid ContourXD map and Ethernet networking capabilities provides the altitude and latitude coordinates corresponding to each mapping.

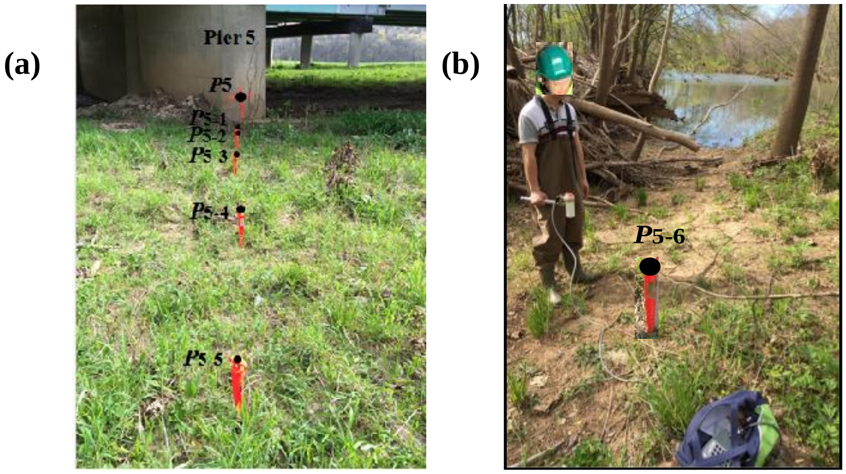

Figure 5.9. Time-varying ambient magnetic field measurement near Pier 5.

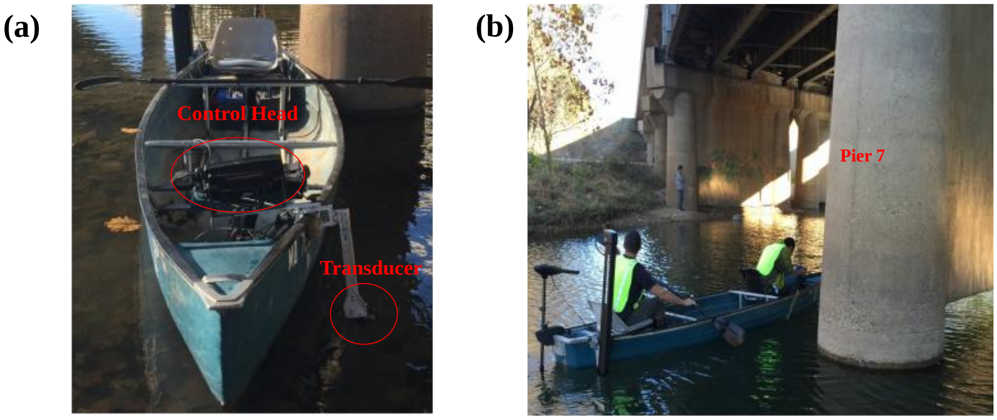

Figure 5.10. Sonar installed on a boat for rivebed profiling: (a) setup and (b) operation.

As shown in Figure 5.10(a), the sonar transducer was fixed on one side of the boat and adjusted to ensure it was below the boat. The control head of the sonar connected to the transducer was operated to map the riverbed profile and the location of the smart rock. Along the water flow, the boat first passed as close to the studied pier as possible, as shown in Figure 5.10(b), to collect clear information about the pier, and then made additional parallel runs gradually moving far away from the pier to map the riverbed.

5.2.3. Localization Algorithm. Let the two magnets in a smart rock centered at Point P (X_M, Y_M, Z_M) and measurements taken at Point Q_i (X_i, Y_i, Z_i) ($i=1, 2, \ldots, n$) near the smart rock. The ambient magnetic field of the Earth and other ferromagnetic substances (e.g. steel reinforcement), $\boldsymbol{B}_{Ai}^{(M)}$ $(B_{AXi}^{(M)}, B_{AYi}^{(M)}, B_{AZi}^{(M)})$, and the total magnetic field of the Earth, the smart rock, and other ferromagnetic substances, $\boldsymbol{B}_{Ti}^{(M)}$

$(B_{TXi}^{(M)}, B_{TYi}^{(M)}, B_{TZi}^{(M)})$, are measured at an particular point Q_i. The total magnetic field can also be expressed into a summation of the effect of the magnets and the measured ambient magnetic field. That is, $B_{TXi}^{(P)} = B_{MXi} + B_{AXi}^{(M)}$, $B_{TYi}^{(P)} = B_{MYi} + B_{AYi}^{(M)}$, $B_{TZi}^{(P)} = B_{MZi} + B_{AZi}^{(M)}$, and $B_{Ti}^{(P)} = \sqrt{(B_{TXi}^{(P)})^2 + (B_{TYi}^{(P)})^2 + (B_{TZi}^{(P)})^2}$ in which the magnetic field of the magnets, $\mathbf{B}_{Mi}(B_{MXi}, B_{MYi}, B_{MZi})$, at any point Q_i (X_i, Y_i, Z_i) can be evaluated by:

$$\begin{pmatrix} B_{MXi} \\ B_{MYi} \\ B_{MZi} \end{pmatrix} = \mathbf{R}^{-1} \begin{pmatrix} k\dfrac{3x_i y_i}{r^5} \\ k\dfrac{2{y_i}^2 - {x_i}^2 - {z_i}^2}{r^5} \\ k\dfrac{3z_i y_i}{r^5} \end{pmatrix} \tag{5.1a}$$

$$\begin{pmatrix} x_i \\ y_i \\ z_i \end{pmatrix} = \mathbf{R} \cdot \begin{pmatrix} X_i - X_M \\ Y_i - Y_M \\ Z_i - Z_M \end{pmatrix} \tag{5.1b}$$

$$\mathbf{R} = \begin{bmatrix} \cos\ \cos\text{¥} & \cos\ \sin\text{¥} & -\sin \\ \sin\sim\sin\ \cos\text{¥} - \cos\sim\sin\text{¥} & \sin\sim\sin\ \sin\text{¥} + \cos\sim\cos\text{¥} & \sin\sim\cos \\ \cos\sim\sin\ \cos\text{¥} + \sin\sim\sin\text{¥} & \cos\sim\sin\ \sin\text{¥} - \sin\sim\cos\text{¥} & \cos\sim\cos \end{bmatrix} \tag{5.1c}$$

$$r = \sqrt{x_i^2 + y_i^2 + z_i^2} \tag{5.1d}$$

$$B_{Mi} = \sqrt{B_{MXi}^2 + B_{MYi}^2 + B_{MZi}^2} \tag{5.1e}$$

In an APUS, the y-axis from South to North pole of the magnet(s) is controlled by the gravity effect and has nothing to do with the geographical south of the Earth. In addition, the cylinder magnet is axis-symmetric about the y-axis. Therefore, the local x-axis and z-axis perpendicular to the y-axis can be selected for convenience so long as they follow the right-hand rule. In this section, the local x-axis is selected to be in parallel with the global X-axis as defined in Figure 5.4. In this case, the local y-axis is pointing down, which is opposite to the global Z-axis. Thus, the orientation of the magnet(s) corresponds to Euler angles $\alpha = 3\pi/2$, $\beta = 0$, and $\gamma = 0$ in the global coordinate system. Eq. (5.1) then becomes

$$\begin{pmatrix} B_{MXi} \\ B_{MYi} \\ B_{MZi} \end{pmatrix} = \begin{pmatrix} -k\dfrac{3\left(Z_i - Z_M\right)\left(X_i - X_M\right)}{\left(\sqrt{\left(X_i - X_M\right)^2 + \left(Y_i - Y_M\right)^2 + \left(Z_i - Z_M\right)^2}\right)^5} \\ -k\dfrac{3\left(Z_i - Z_M\right)\left(Y_i - Y_M\right)}{\left(\sqrt{\left(X_i - X_M\right)^2 + \left(Y_i - Y_M\right)^2 + \left(Z_i - Z_M\right)^2}\right)^5} \\ -k\dfrac{2\left(Z_i - Z_M\right)^2 - \left(X_i - X_M\right)^2 - \left(Y_i - Y_M\right)^2}{\left(\sqrt{\left(X_i - X_M\right)^2 + \left(Y_i - Y_M\right)^2 + \left(Z_i - Z_M\right)^2}\right)^5} \end{pmatrix} \tag{5.2}$$

Here, k represents a strength factor of the magnets in nT·m^3, which is calculated from the maximum residual flux density (or Br) of the magnets.

To locate the smart rock, an objective error function is defined as a SRSS difference of the predicted and the measured magnetic field intensity at all measurement points Q_i (X_i, Y_i, Z_i) $(i=1, 2, \ldots, n)$. That is,

$$J(X_M, Y_M, Z_M) = \sqrt{\sum_{i=1}^{n} [B_{Ti}^{(P)} - B_{Ti}^{(M)}]^2} \tag{5.3}$$

The objective error function in Eq. (5.3) is minimized to derive the coordinate of the smart rock, P (X_M, Y_M, Z_M).

5.2.4. Test Results and Discussion. To date, three series of field tests have been completed at this bridge site. Both rock positioning accuracy and movement trend are discussed below.

5.2.4.1 First series of field tests. The first series of tests were carried out on November 6, 2015. Table 5.1 summarizes the coordinates of 42 measurement points, the ambient magnetic field (AMF) intensities prior to smart rock deployment, and the total intensities after deployment of the smart rock SR1. The coefficient $k = 86521$ $nT.m^3$ for two stacked N42 magnets was calculated from the maximum residual flux density. The three components of the magnetic field were measured using the 3-axis digital magnetometer sensor oriented in parallel with the X-, Y-, and Z-axis.

Table 5.1. Coordinates and intensities from the first series of field tests

Measurement Point		Measurement Point Coordinate (m)			AMF Intensity (10^4 nT)			Total Intensity (10^4 nT)
		X_i	Y_i	Z_i	$B_{XA}^{(M)}$	$B_{YA}^{(M)}$	$B_{ZA}^{(M)}$	$B_T^{(M)}$
S_1P_1	E_1	3.85	21.79	-1.00	2.278	0.102	-4.891	5.322
	E_2	3.82	21.61	-0.70	2.241	0.174	-4.900	5.335
	E_3	3.81	21.63	-0.41	2.242	0.223	-4.895	5.345
	E_4	3.81	21.67	-0.12	2.244	0.237	-4.891	5.354
	E_5	3.79	21.56	0.19	2.241	0.232	-4.891	5.362
	E_6	3.79	21.51	0.49	2.287	0.335	-4.867	5.369
	E_7	3.83	21.55	0.80	2.263	0.240	-4.878	5.370
S_1P_2	E_1	2.07	21.87	-0.99	2.278	0.167	-4.893	5.327
	E_2	2.06	21.78	-0.72	2.278	0.167	-4.893	5.372
	E_3	2.06	21.81	-0.40	2.246	0.280	-4.911	5.407
	E_4	2.00	21.67	-0.10	2.245	0.286	-4.918	5.437
	E_5	2.07	21.70	0.19	2.240	0.271	-4.929	5.458
	E_6	2.08	21.63	0.47	2.246	0.293	-4.938	5.470
	E_7	2.08	21.61	0.78	2.250	0.324	-4.948	5.490
S_2P_1	E_1	3.84	24.51	-1.00	2.247	0.216	-4.873	5.288
	E_2	3.83	24.50	-0.74	2.256	0.248	-4.861	5.296
	E_3	3.81	24.42	-0.39	2.241	0.254	-4.862	5.307
	E_4	3.79	24.32	-0.11	2.288	0.279	-4.835	5.318
	E_5	3.80	24.39	0.18	2.237	0.280	-4.855	5.327
	E_6	3.80	24.37	0.47	2.248	0.271	-4.848	5.334
	E_7	3.79	24.29	0.78	2.235	0.279	-4.851	5.342
S_2P_2	E_1	2.07	24.57	-1.00	2.295	0.441	-4.798	5.258
	E_2	2.01	24.45	-0.71	2.285	0.493	-4.785	5.323
	E_3	2.04	24.49	-0.40	2.268	0.568	-4.781	5.359
	E_4	2.04	24.48	-0.11	2.233	0.524	-4.819	5.387
	E_5	2.03	24.40	0.19	2.233	0.496	-4.837	5.417
	E_6	1.96	24.20	0.50	2.224	0.519	-4.856	5.438
	E_7	2.08	24.30	0.80	2.230	0.555	-4.866	5.445
S_3P_1	E_1	3.84	27.69	-1.03	2.149	0.225	-4.899	5.320
	E_2	3.84	27.67	-0.74	2.154	0.240	-4.895	5.323
	E_3	3.79	27.59	-0.41	2.158	0.269	-4.891	5.326
	E_4	3.84	27.58	-0.12	2.175	0.253	-4.884	5.327
	E_5	3.84	27.55	0.19	2.186	0.274	-4.873	5.331
	E_6	3.85	27.52	0.47	2.178	0.258	-4.878	5.334
	E_7	3.84	27.45	0.76	2.176	0.339	-4.869	5.334

Table 5.1. Coordinates and intensities from the first series of field tests (cont.)

S_3P_2	E_1	2.13	27.59	-1.02	2.084	0.523	-4.928	5.326
	E_2	2.11	27.30	-0.72	2.089	0.529	-4.927	5.336
	E_3	2.04	27.21	-0.41	2.108	0.545	-4.920	5.345
	E_4	2.04	27.31	-0.12	2.105	0.537	-4.927	5.359
	E_5	2.03	27.26	0.19	2.128	0.536	-4.925	5.375
	E_6	2.09	27.36	0.47	2.153	0.579	-4.912	5.388
	E_7	2.08	27.30	0.76	2.170	0.688	-4.898	5.400

Given the coordinates, AMF intensities, and total intensities at various measurement points in Table 5.1, the minimization of Eq. (5.3) yielded the predicted coordinate of the smart rock as presented in Table 5.2. By comparing the predicted coordinate with the measured from the total station, also listed in Table 5.2, a prediction error of *0.26 m* was determined. The prediction error mainly occurred in Y coordinate likely because the measurement bar was inaccurately placed on top of the smart rock with *0.368 m* in diameter. Overall, the prediction error of *0.26 m* is much less than *0.5 m*, a target rock positioning accuracy set forth for engineering applications.

Table 5.2. Predicted and measured location of the smart rock

Test date	Predicted coordinate			Measured coordinate			Prediction error (m)
	X_M (m)	Y_M (m)	Z_M (m)	X_M (m)	Y_M (m)	Z_M (m)	
11/06/15 (1st)	0.06	23.49	-3.03	0.09	23.24	-3.04	0.26
04/14/16 (2nd)	0.55	24.38	-3.21	0.37	24.60	-3.38	0.33
10/20/16 (3rd)	0.00	22.73	-2.59	0.00	22.63	-2.87	0.30

5.2.4.2 Second series of field tests. The second series of field tests were carried out on April 14, 2016. These tests followed the same test protocol as established during the first series of field tests. The coordinate system set up during these tests was slightly translated from that used during the first series of tests. It was transformed to the first coordinate system through the benchmark A on Pier 9.

The Earth's magnetic field intensity was measured using a magnetometer G858 at Point $P_{5\text{-}6}$ near Pier 5. It was *51,760 nT* during the first series of tests and *52,120 nT* during the second series of tests, which indicates a *0.7%* increase in magnetic field intensity of the Earth. By comparing the Earth's magnetic field intensity from the first series of tests with that of the AMF intensity in Table 5.1, the magnetic field resulting from the steel reinforcement near Bent 7 is less than *2,700 nT* or *5.3%* of the Earth's field intensity. The steel reinforcement is magnetized in the Earth's magnetic field. The secondary magnetic field generated by the reinforcement is approximately correlated with the Earth's magnetic field, both varying over time as a result of the direct or indirect effect of solar wind. Therefore, the AMF during the second series of tests was approximated by increasing the AMF during the first series of tests by *0.7%*. Table 5.3 summarizes the coordinates, the adjusted AMF intensities, and the total intensities at various measurement points from the second series of field tests.

Table 5.3. Coordinates and intensities from the second series of field tests

Measurement Point		Measurement Point Coordinate (m)			AMF Intensity (10^4 nT)			Total Intensity (10^4 nT)
		X_i	Y_i	Z_i	$B_{XA}^{(M)}$	$B_{YA}^{(M)}$	$B_{ZA}^{(M)}$	$B_T^{(M)}$
S_1P_1	E_1	3.83	21.77	-1.00	2.294	0.102	-4.925	5.375
	E_2	3.82	21.66	-0.71	2.256	0.175	-4.935	5.385
	E_3	3.80	21.61	-0.41	2.258	0.225	-4.929	5.395
	E_4	3.80	21.65	-0.12	2.260	0.239	-4.926	5.404
	E_5	3.76	21.51	0.18	2.257	0.234	-4.925	5.409
	E_6	3.79	21.56	0.47	2.303	0.337	-4.901	5.416
	E_7	3.81	21.53	0.79	2.279	0.242	-4.912	5.419
S_1P_2	E_1	3.83	24.54	-1.00	2.263	0.218	-4.908	5.318
	E_2	3.87	24.42	-0.74	2.271	0.250	-4.895	5.342
	E_3	3.80	24.40	-0.40	2.257	0.256	-4.896	5.361
	E_4	3.75	24.34	-0.13	2.304	0.281	-4.869	5.375
	E_5	3.82	24.37	0.19	2.252	0.282	-4.889	5.385
	E_6	3.78	24.34	0.47	2.264	0.273	-4.882	5.393
	E_7	3.75	24.23	0.77	2.251	0.281	-4.885	5.396
S_2P_1	E_1	3.85	27.66	-1.02	2.164	0.227	-4.933	5.339
	E_2	3.84	27.62	-0.73	2.169	0.242	-4.929	5.347
	E_3	3.75	27.57	-0.42	2.173	0.271	-4.925	5.355
	E_4	3.84	27.50	-0.12	2.190	0.254	-4.918	5.362
	E_5	3.85	27.58	0.19	2.201	0.276	-4.907	5.367
	E_6	3.83	27.54	0.47	2.193	0.260	-4.912	5.372
	E_7	3.85	27.49	0.77	2.191	0.342	-4.903	5.374

Table 5.3. Coordinates and intensities from the second series of field tests (cont.)

S_2P_2	E_1	2.05	21.86	-1.00	2.294	0.168	-4.928	5.405
	E_2	2.07	21.72	-0.72	2.294	0.168	-4.928	5.433
	E_3	2.06	21.88	-0.42	2.261	0.281	-4.945	5.456
	E_4	2.08	21.68	-0.11	2.261	0.288	-4.953	5.476
	E_5	2.07	21.62	0.19	2.256	0.273	-4.964	5.493
	E_6	2.06	21.61	0.47	2.261	0.296	-4.973	5.509
	E_7	2.07	21.62	0.78	2.265	0.326	-4.982	5.522
S_3P_1	E_1	2.07	24.55	-0.99	2.311	0.444	-4.832	5.590
	E_2	2.01	24.41	-0.71	2.301	0.497	-4.818	5.580
	E_3	2.07	24.43	-0.41	2.284	0.572	-4.814	5.571
	E_4	2.08	24.46	-0.11	2.249	0.527	-4.853	5.560
	E_5	2.09	24.47	0.20	2.249	0.499	-4.871	5.547
	E_6	2.09	24.20	0.49	2.239	0.523	-4.890	5.544
	E_7	2.09	24.32	0.79	2.245	0.559	-4.900	5.539
S_3P_2	E_1	2.14	27.57	-1.01	2.099	0.526	-4.963	5.372
	E_2	2.13	27.32	-0.72	2.104	0.532	-4.962	5.392
	E_3	2.06	27.23	-0.40	2.123	0.549	-4.955	5.411
	E_4	2.04	27.37	-0.12	2.120	0.541	-4.962	5.427
	E_5	2.05	27.25	0.18	2.143	0.540	-4.959	5.442
	E_6	2.11	27.31	0.47	2.168	0.583	-4.947	5.455
	E_7	2.04	27.28	0.76	2.185	0.693	-4.932	5.467

As shown in Table 5.2, the prediction error in rock positioning during the second series of tests was *0.33 m*, which is nearly 30% higher than that during the first series of tests. The higher level of prediction error was likely attributed to the less accurate AMF. Nevertheless, a prediction error of *0.33 m* is still much less than *0.5 m*, which is acceptable in engineering application.

5.2.4.3 Third series of field tests. The third series of tests were carried out on October 20, 2016. These tests also followed the same test protocol as established during the first series of field tests. The coordinate system set up during the third series of tests was also transformed to the first coordinate system through the benchmark A on Pier 9. Similarly, the Earth's magnetic field intensity was measured using a magnetometer G858 at Point $P_{5\text{-}6}$ near Pier 5. It was *51,761 nT* during the first series of tests and *52,021 nT* during the third series of tests, which indicates a *0.5%* increase in magnetic field intensity. Following the same analysis mechanism as used during the second series of field tests, the AMF during the third series of tests was adjusted by increasing the AMF during the first series of tests by *0.5%*. Table 5.4 summarizes the coordinates, the adjusted AMF intensities, and the total intensities at various measurement points for the third series of field tests.

As shown in Table 5.2, the prediction error in rock positioning during the third series of tests was *0.30 m*, which is nearly 16% higher than that during the first series of tests. The higher level of prediction error was also attributed to the less accurate AMF. Nevertheless, a prediction error of *0.30 m* is still acceptable in engineering application.

Table 5.4. Coordinates and intensities from the third series of field tests

Measurement Point		Measurement Point Coordinate (m)			AMF Intensity (10^4 nT)			Total Intensity (10^4 nT)
		X_i	Y_i	Z_i	$B_{XA}^{(M)}$	$B_{YA}^{(M)}$	$B_{ZA}^{(M)}$	$B_T^{(M)}$
S_1P_1	E1	3.81	21.77	-0.93	2.290	0.102	-4.915	5.350
	E_2	3.82	21.63	-0.68	2.252	0.175	-4.925	5.365
	E_3	3.78	21.37	-0.32	2.253	0.224	-4.920	5.381
	E_4	3.81	21.35	-0.10	2.256	0.238	-4.916	5.395
	E_5	3.74	21.23	0.28	2.252	0.233	-4.915	5.403
	E_6	3.79	21.36	0.50	2.298	0.336	-4.892	5.408
	E_7	3.81	21.35	0.88	2.274	0.241	-4.902	5.413
S_1P_2	E_1	3.76	24.09	-0.94	2.258	0.217	-4.898	5.308
	E_2	3.78	24.09	-0.72	2.267	0.249	-4.886	5.327
	E_3	3.76	24.05	-0.33	2.253	0.256	-4.886	5.343
	E_4	3.77	24.08	-0.01	2.300	0.281	-4.859	5.358
	E_5	3.77	24.07	0.20	2.248	0.281	-4.879	5.369
	E_6	3.77	24.06	0.49	2.259	0.272	-4.872	5.379
	E_7	3.76	23.97	0.87	2.246	0.280	-4.875	5.386
S_2P_1	E_1	3.73	27.21	-0.94	2.160	0.226	-4.924	5.358
	E_2	3.77	27.20	-0.71	2.165	0.241	-4.919	5.362
	E_3	3.79	27.17	-0.33	2.168	0.270	-4.915	5.366
	E_4	3.78	27.20	-0.12	2.186	0.254	-4.908	5.370
	E_5	3.78	27.21	0.27	2.197	0.276	-4.898	5.374
	E_6	3.76	27.14	0.48	2.189	0.260	-4.903	5.378
	E_7	3.69	27.05	0.78	2.187	0.341	-4.893	5.380
S_2P_2	E_1	2.06	21.14	-0.93	2.289	0.167	-4.918	5.400
	E_2	2.08	21.16	-0.71	2.289	0.167	-4.918	5.437
	E_3	2.06	21.14	-0.32	2.257	0.281	-4.936	5.469
	E_4	2.02	20.91	-0.01	2.256	0.288	-4.943	5.497

Table 5.4. Coordinates and intensities from the third series of field tests (cont.)

S_2P_2	E_5	2.04	21.09	0.28	2.251	0.272	-4.954	5.519
	E_6	2.06	21.06	0.48	2.257	0.295	-4.963	5.535
	E_7	2.12	21.12	0.87	2.261	0.325	-4.972	5.540
S_3P_1	E_1	2.09	23.91	-0.92	2.306	0.443	-4.822	5.349
	E_2	2.09	23.83	-0.70	2.296	0.496	-4.809	5.428
	E_3	2.14	23.90	-0.32	2.279	0.571	-4.805	5.445
	E_4	2.14	23.89	-0.11	2.244	0.526	-4.843	5.471
	E_5	2.15	23.88	0.28	2.244	0.498	-4.862	5.487
	E_6	2.11	23.85	0.50	2.235	0.522	-4.880	5.510
	E_7	2.14	23.88	0.88	2.241	0.558	-4.890	5.515
S_3P_2	E_1	2.07	27.03	-0.94	2.095	0.525	-4.953	5.376
	E_2	2.14	27.06	-0.71	2.100	0.531	-4.952	5.390
	E_3	2.10	26.96	-0.33	2.118	0.548	-4.945	5.402
	E_4	2.16	27.08	-0.02	2.116	0.540	-4.952	5.417
	E_5	2.13	27.07	0.27	2.139	0.539	-4.950	5.430
	E_6	2.10	27.01	0.50	2.164	0.582	-4.937	5.448
	E_7	2.08	26.83	0.77	2.181	0.691	-4.922	5.457

5.2.4.4 Smart rock movement and scour depth. The predicted and measured coordinates of the smart rock obtained from the first, second and third series of tests, as listed in Table 5.2, were used to calculate the displacement of the smart rock between the three tests both numerically and experimentally. The three displacement components (ΔX_M, ΔY_M, ΔZ_M) and the total displacement as well as the difference between the predicted and measured displacements are presented in Table 5.5.

Table 5.5. Prediction accuracy of smart rock movement

Displacement	From first to second series of tests				From second to third series of tests			
	ΔX_M (m)	ΔY_M (m)	ΔZ_M (m)	Total (m)	ΔX_M (m)	ΔY_M (m)	ΔZ_M (m)	Total (m)
Predicted	0.49	0.89	-0.18	1.04	-0.55	-1.65	0.62	1.85
Measured	0.28	1.37	-0.34	1.44	-0.37	-1.97	0.51	2.06
Difference	0.21	-0.47	0.16	-0.40	-0.19	0.32	0.11	-0.21

Figure 5.11 illustrates the measured position and movement of the smart rock in the scour hole around Pier 7 during the three site visits. The movement is displayed on a

three-dimensional contour map created in ArcGIS based on the riverbed survey data collected with the sonar and total station in the Cartesian coordinate system O-XYZ established during the second and third series of field tests.

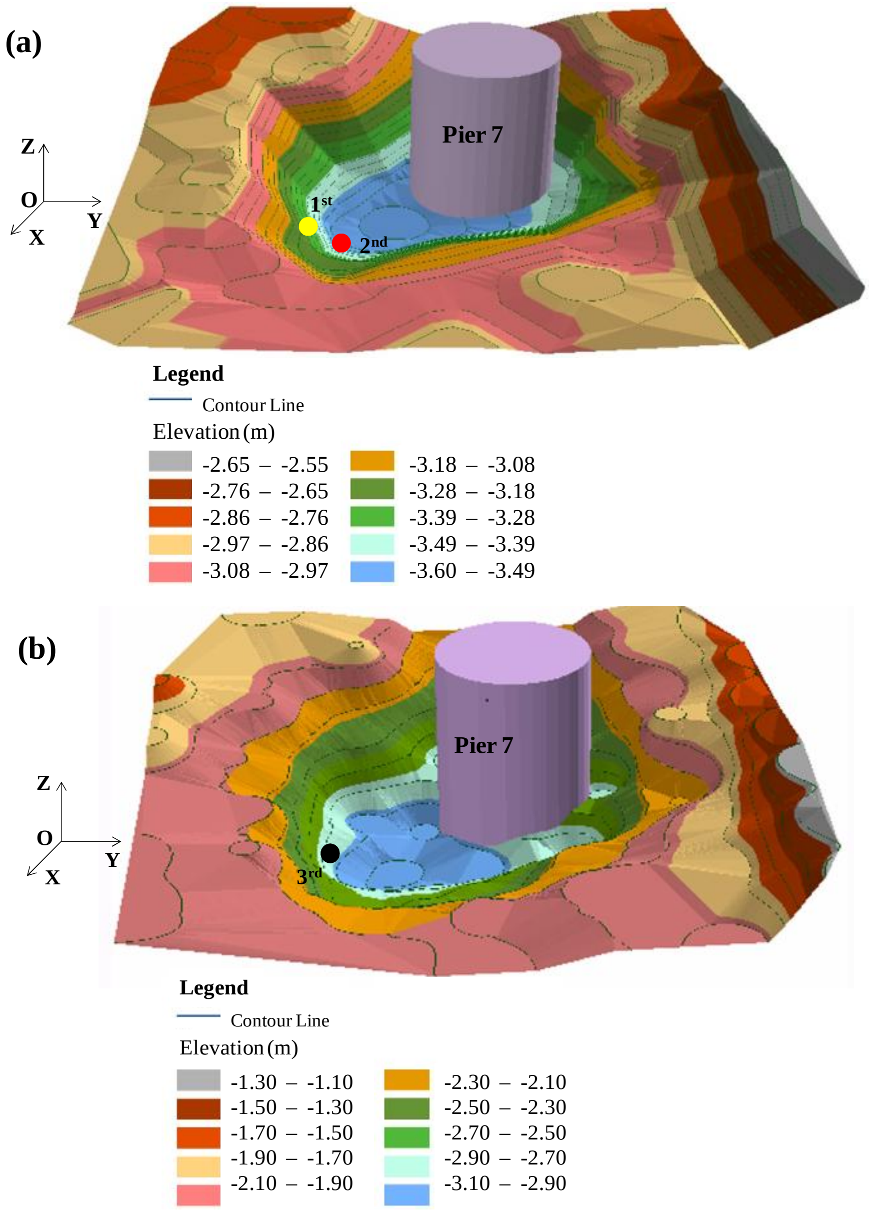

Figure 5.11. The smart rock movement in the scour hole around Pier 7: (a) the second field test and (b) the third field test.

From the first to second series of tests, the predicted and measured total displacements are *1.04 m* and *1.44 m*, respectively. They are differed by *0.4 m*. The maximum component displacement error of *0.47 m* occurred in Y-direction or traffic direction. As explained previously, this error is likely attributed to the potentially misplaced measurement bar in the process of measuring the location of the smart rock. Nevertheless, both the component and total displacement errors are less than *0.5 m*, a level of accuracy acceptable in engineering application. It is also important to note that the predicted and measured movement directions of the smart rock are all consistent. In particular, the smart rock was settled down by *0.18 m* (prediction) or *0.34 m* (measurement) during the December 27, 2015 flood.

From the second to third series of tests, the predicted and measured total displacements are *1.85 m* and *2.06 m*, respectively. They are differed by *0.21 m*. The maximum component displacement error of *0.32 m* also came from Y-direction because of the main error from actual location measurement and other factors discussed in the prediction error of localization. Nevertheless, both the component and total displacement errors are within the acceptable range in application. Between the second and third series of tests, the smart rock moved upward in Z direction by *0.51 m* and away from Pier 7 in Y direction by *1.97 m*. These movements may result from the change of the scour hole in shape and deposits refilling between the two series of tests.

5.3. STATE HIGHWAY 1 WADDELL CREEK BRIDGE

In this section, the State Highway 1 Bridge (No. 36-0065) over the Waddell Creek, approximately 27 km north of the City of Santa Cruz in California, was used as the second test site to validate the performance of the smart rock. As shown in Figure 5.12, the bridge is a four-span, continuous reinforced concrete T-girder structure, supporting two lanes of two way traffic on California Highway 1. The upstream of the bridge is a small creek formed between low mountains while the downstream of the bridge is only a few hundreds of meters from the Pacific Ocean. The bridge site is exposed to a complex hydraulic condition, combining the strong water flow from the mountains during flood events and the strong current from the Pacific Ocean during high tides. As a result, the embankment around South Abutment 1 (closer to Santa Cruz) experienced severe erosion extending from the channel bank from the upstream. Since Caltrans already protected the Abutment 1 with rocks, Abutment 1 was used as a validation site of monitoring the riprap effectiveness with a smart rock. Similarly, the pier at Bent 2 was considered by Caltrans as scour critical and thus used as a validation site for scour depth monitoring with the smart rock technology. To date, two series of field tests were carried out to validate the localization and movement of the smart rock driven by flood events or normal water flow.

Figure 5.12. State Highway 1 Bridge over Waddell Creek, CA.

During the first series of field tests, one smart rock with two stacked magnets in the APUS configuration was placed among a few widely spaced natural rocks at the toe of riprap measures around Abutment 1 for riprap effectiveness monitoring. Two additional smart rocks were placed on the surface of the riverbed near Bent 2 for bridge scour monitoring. The test crane was placed on the bridge deck with a mounted magnetometer sensor to facilitate measurements of the intensity and direction of the ambient magnetic field and the total field after the smart rocks had been deployed.

During the second series of field tests, the three smart rocks deployed previously were found to have been washed away likely due to the strong tide waves from the Pacific Ocean occurred in March 2016. Therefore, two new smart rocks were deployed again near Bent 2 to validate the localization algorithms for one or two smart rocks. This time, however, the smart rocks were buried into the riverbed such that the top of the smart rocks was flush with the riverbed with the intent of making them difficult to be washed away. The test crane was mounted on a flatbed trailer for easy maneuver.

5.3.1. Planning for the First Series of Field Tests. All tests were conducted near South Abutment 1 on the Santa Cruz side and the pier at Bent 2 of the 4-span bridge as shown in Figure 5.13(a, b). A total station was set near North Abutment 5 on the San

Francisco side to measure the coordinates (location) of three smart rocks and the magnetometer sensor as ground truth data. The center of the total station was used as the origin of a Cartesian coordinate system O-XYZ with X-, Y-, and Z- axles oriented transversely (upstream to downstream direction), longitudinally (south bound traffic direction), and vertically (upward direction). Two smart rocks, designated as SR1 and SR2, were deployed on two sides of the Bent 2 in far and near distances, respectively. The third smart rock, SR3, placed in the gap of riprap rocks around South Abutment 1. The magnetometer sensor mounted on the test crane was extended down from the bridge deck for measurement of the ambient magnetic field and the total magnetic field with the smart rocks placed at three locations. Prism 3 mounted below the sensor was used to represent the location of each measurement point. The measurement points in XOY plane are shown in Figure 5.13(a) as the cross points of Mesh 1 for Abutment 1 and Mesh 3 for Bent 2. The sensor points in Mesh 1 and Mesh 3 were translated to Mesh 2 and Mesh 4 on the bride deck for representation positions of the forklift as displayed in Figure 5.13(c). These forklift points were represented as four Paths (P1, P2, P3 and P4) and three Stops (S1, S2 and S3) on each path. For each stop on one path, seven elevations denoted as E1, E2, E3, E4, E5, E6 and E7 with equal spacing of 0.3 m were positioned for field measurements. Therefore, a total of 84 measurements were taken for SR3 around Abutment 1 and for SR1 & SR2 around Bent 2.

As used for the I-44W Roubidoux Creek Bridge in Missouri, the seven-step test procedure was adopted for the Waddell Creek Bridge in California as follows in detail:

(1) *Set the XYZ coordinate system*. As shown in Figure 5.14, a permanent Point A on concrete pedestal at the top and upstream/east side of south abutment was selected as the benchmark for this bridge site. The total station was set at Point O on the north end of the bridge such that Y-axis along the traffic (longitudinal) direction to Santa Cruz is parallel to the tangential line of bridge railing closest to Point A, X-axis is perpendicular to the Y-axis and pointing to downstream/west in the horizontal plane, and Z-axis is pointing up according to the right hand rule.

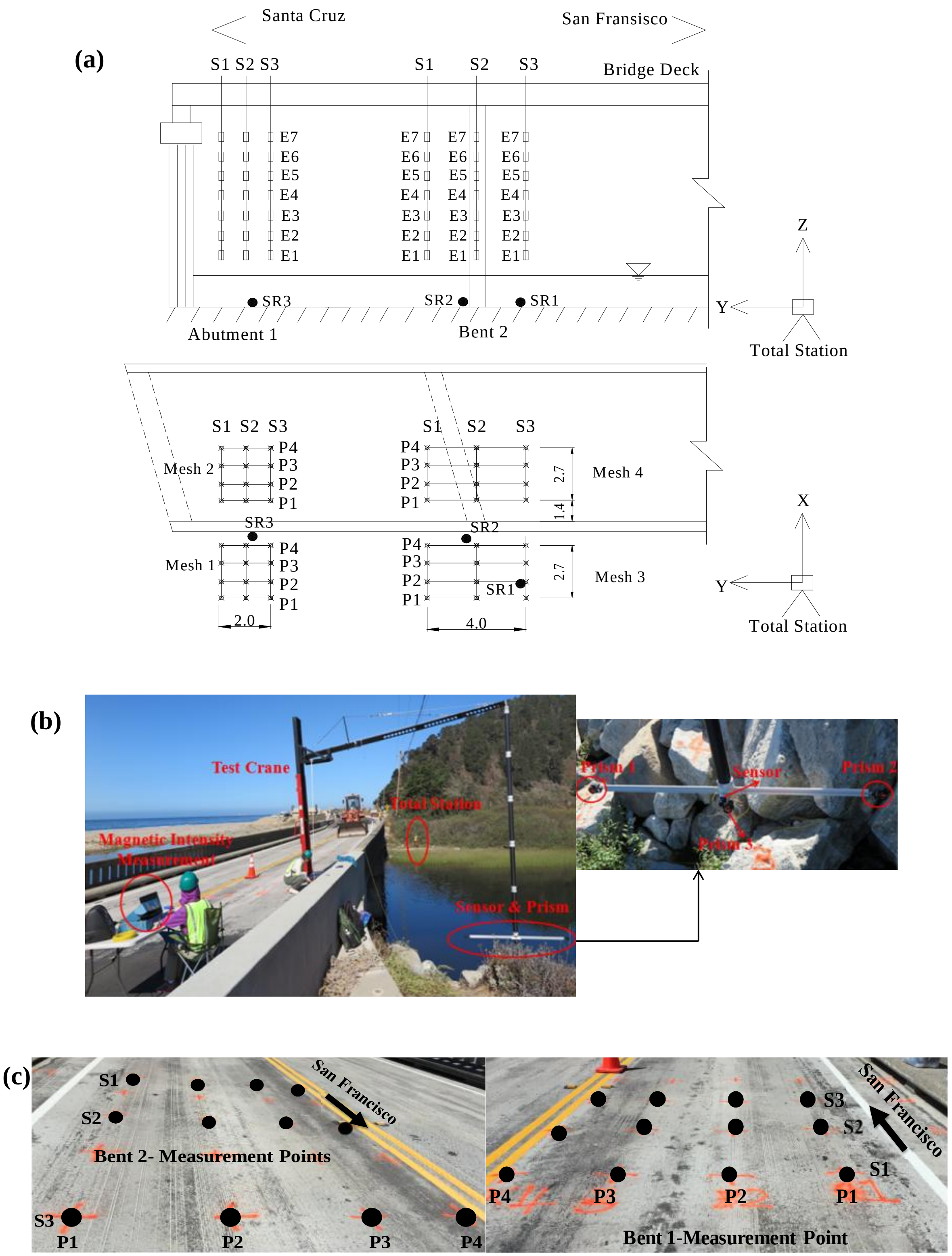

Figure 5.13. Waddell Creek bridge – first series of tests: (a) planning (unit: m), (b) test setup, and (c) forklift positions.

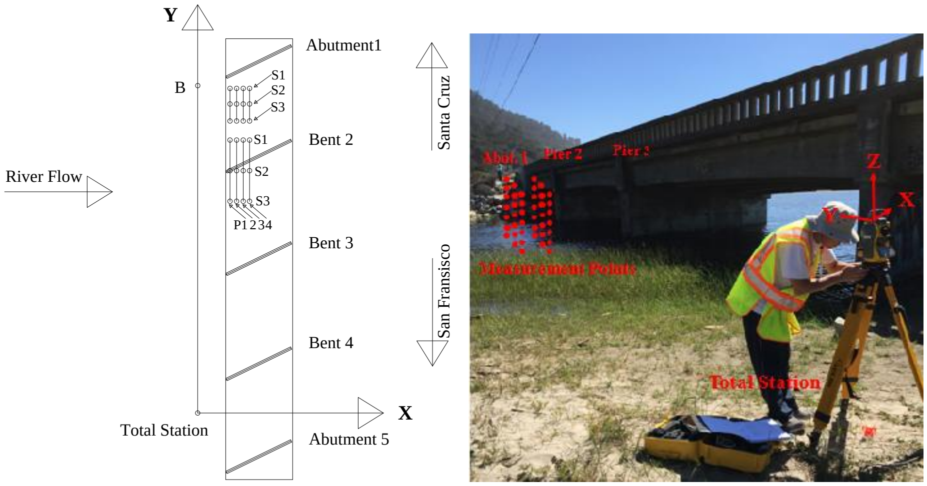

Figure 5.14. Selection of the coordinate system.

(2) *Assemble the test crane*. The test crane as shown in Figure 5.13 (b) was directly set on the bridge deck. The forklift was first placed on the bridge deck. The horizontal aluminum arm was then installed and five segments of carbon fiber tubes with 1.0 m each were assembled. Finally, the horizontal bar with three prisms and sensor attached was connected to the bottom tube.

(3) *Set up the STL digital magnetometer*. The magnetometer was set up in exactly the same way as used at the I-44W Roubidoux Creek bridge site.

(4) *Measure the ambient magnetic field.* The ambient magnetic field was measured prior to deployment of the smart rocks. The forklift was first parked at S1P1 and the horizontal arm was moved up or down between E1 and E7 for simultaneous measurements of the coordinate and intensity at each elevation. The forklift was then moved to S1P2, S1P3 and S1P4 for successive measurements along X axis. It was further moved to S2 and S3 lines along Y axis to repeat the same measurements as those along S1 line in X direction. The same sequence and steps were followed near Bent 2 to complete the measurements along S1, S2 and S3 lines, respectively, as illustrated in Figure 5.15.

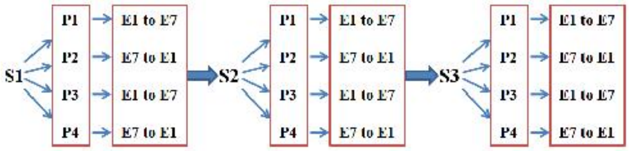

Figure 5.15. Sequence for ambient magnetic field measurements.

(5) *Deploy the smart rocks and measure their coordinates.* Three smart rocks with the APUS, as shown in Figure 5.7, were deployed as indicated in Figure 5.16 before the total magnetic field was measured. As shown in Figure 5.16(a), SR1 and SR2 were located on the north and south sides of Bent 2 for scour monitoring and SR3 between two rocks near the south abutment for riprap effectiveness monitoring. The three smart rocks were individually transported in a boat and dropped at the predetermined sites as indicated in Figure 5.16(b). As illustrated in Figure 5.16(c), SR3 in shallow water can be clearly seen from the bridge deck, SR2 close to the bottom of the scour hole can be barely seen when the water is calm, and SR1 farther away from Bent 2 with a connection rope floated on the water surface can be located as well. The deployed smart rocks were surveyed for their coordinates from the total station through the placement of a prism on top of each smart rock.

(6) *Measure the total magnetic field.* After the deployment of smart rocks, the total magnetic field from the smart rocks, the Earth, and the nearby ferromagnetic objects was measured following the same procedure as used for the ambient magnetic field measurements except that only six elevations were considered in Z direction for all points near the south abutment. Therefore, a total of 72 and 84 measurements were taken around the south abutment for SR3 and around Bent 2 for SR1 and SR2, respectively.

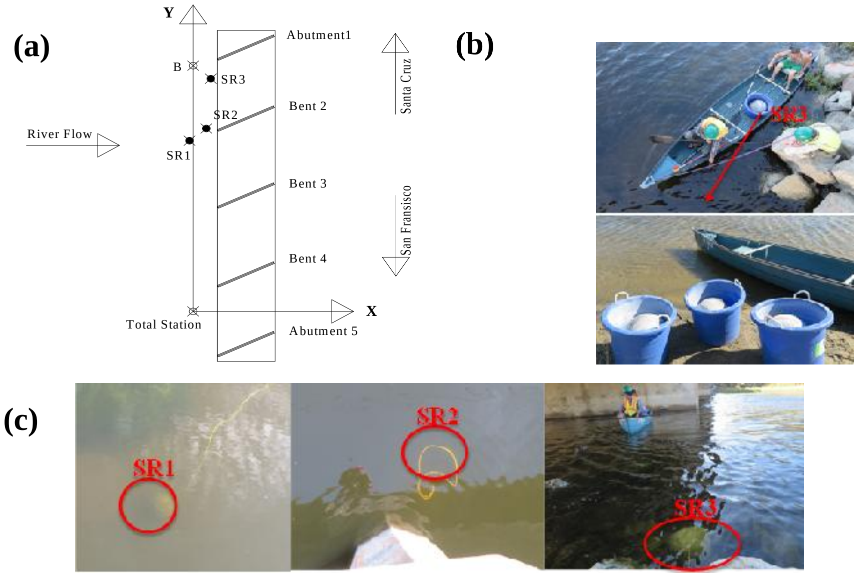

Figure 5.16. Application of three smart rocks: (a) locations, (b) SR3 deployment, and (c) top views.

5.3.2. Planning for the Second Series of Field Tests. The spherical smart rock SR3 deployed previously had no interlock with nearby natural rocks. It was witnessed by a Caltrans engineer to have been washed away due to strong tide waves. Heavier and polyhedral smart rocks are recommended for riprap effectiveness monitoring in the future.

Therefore, the second series of field tests were focused on the localization of smart rocks near Bent 2. Since the previously deployed smart rocks SR1 and SR2 cannot be located near the bridge, they were assumed to have also been washed away. As a result, two same smart rocks, also named SR1 and SR2, were deployed near Bent 2 again. This time, however, the smart rocks were buried in the riverbed to increase their resistance to strong water current. The test layout was also changed and simplified based on the experience gained from the first series of field tests, as shown in Figure 5.17. The test crane as shown in Figure 5.17(c) was fixed on a flatbed trailer towed by a truck. Through the test crane, the measurement points at the location of the sensor (cross points of Mesh 1) were translated to the corresponding forklift locations (cross points of Mesh 2) represented by two paths (P1 and P2) and seven stops (S1, S2, S3, S4, S5, S6, and S7) on the bridge deck, as depicted in Figure 5.17(d). For each stop on two path of the trailer, seven elevations denoted as E1, E2, E3, E4, E5, E6 and E7 with equal spacing of 0.3 m were considered for magnetic field measurements. Therefore, a total of 98 measurements were taken around Bent 2 in order to locate the two smart rocks.

The second series of field tests followed the same procedure as used during the first series of tests except that the two smart rocks, SR1 and SR2 on the north and south side of Bent 2, were deployed at different times with the total magnetic field measurements taken in between. The ambient magnetic field was first measured following the sequence as shown in Figure 5.18. After the deployment of SR1, the total magnetic field with one smart rock was then measured along two paths P1 and P2 with three stops S4, S5 and S7 at 39 points. After the deployment of SR2, the total magnetic field with two smart rocks as depicted in Figure 5.19 was next measured along the two paths with seven stops at 91 points. Finally, SR2 was moved to a new position represented by SR2' and the total magnetic field was measured again at points P1S2, P1S3, P1S5, P1S6, P2S1, P2S3, P2S5, and P2S7 for a total of 52 measurements.

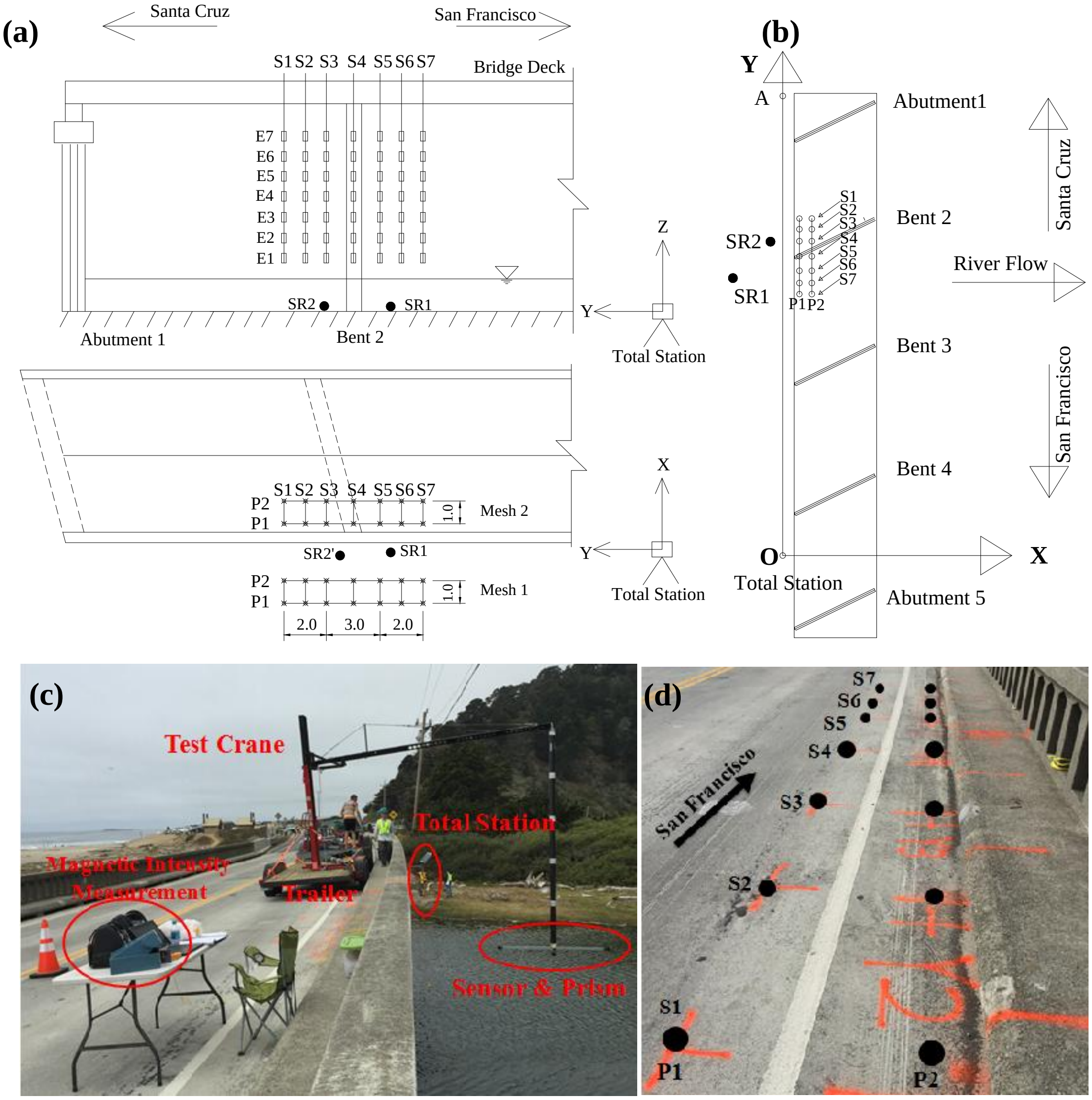

Figure 5.17. Waddell Creek bridge - second series of tests: US63 Bridge site: (a) planning (unit: m), (b) test setup, and (c) forklift positions.

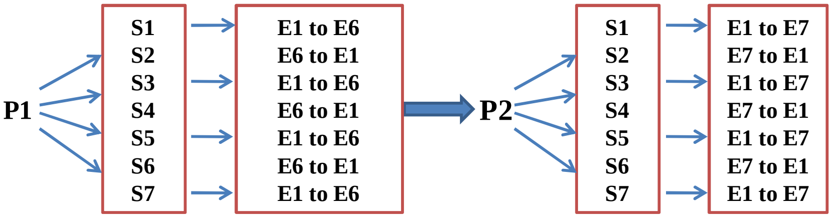

Figure 5.18. Sequence for ambient magnetic field measurement during the second series of field tests.

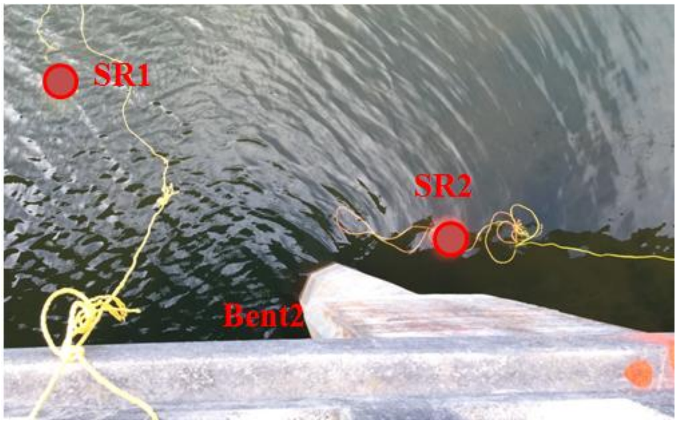

Figure 5.19. Deployed smart rocks: SR1 and SR2 during the second series of test.

5.3.3. Localization Algorithm of One Smart Rock. The localization algorithm for the APUS with two stacked magnets is exactly the same as that used at the I-44W Roubidoux Creek Bridge site.

5.3.4. Localization Algorithm of Two Smart Rocks. Let two magnets be centered at Point P_1 (X_{M1}, Y_{M1}, Z_{M1}) and P_2 (X_{M2}, Y_{M2}, Z_{M2}), respectively, in the Cartesian coordinate system O-XYZ as shown in Figure 5.20. The ambient magnetic field of the Earth and other ferromagnetic substances (e.g. steel reinforcement), $\boldsymbol{B}_{Ai}^{(M)}$ $(B_{AXi}^{(M)}, B_{AYi}^{(M)}, B_{AZi}^{(M)})$, and the total magnetic field of the Earth, the smart rocks, and the other ferromagnetic substances, $\boldsymbol{B}_{Ti}^{(M)}$ $(B_{TXi}^{(M)}, B_{TYi}^{(M)}, B_{TZi}^{(M)})$, are measured at any Point Q_i (X_i, Y_i, Z_i) ($i=1, 2, \ldots, n$) near the two smart rocks. The total magnetic field can also be expressed into a summation of the effect of the two magnets and the experimental ambient magnetic field. That is,

$$B_{TXi}^{(P)} = B_{M1Xi} + B_{M2Xi} + B_{AXi}^{(M)} \tag{5.4a}$$

$$B_{TYi}^{(P)} = B_{M1Yi} + B_{M2Yi} + B_{AYi}^{(M)} \tag{5.4b}$$

$$B_{TZi}^{(P)} = B_{M1Zi} + B_{M2Zi} + B_{AZi}^{(M)} \tag{5.4c}$$

$$B_{Ti}^{(P)} = \sqrt{(B_{TXi}^{(P)})^2 + (B_{TYi}^{(P)})^2 + (B_{TZi}^{(P)})^2} \tag{5.4d}$$

in which the magnetic field of the magnets, $\boldsymbol{B}_{M1i}$ (B_{M1Xi}, B_{M1Yi}, B_{M1Zi}) and $\boldsymbol{B}_{M2i}$ (B_{M2Xi}, B_{M2Yi}, B_{M2Zi}), at any point (X_i, Y_i, Z_i) can be derived in the same way as for Eq. (5.2) and evaluated by:

$$\begin{pmatrix} B_{M1Xi} \\ B_{M1Yi} \\ B_{M1Zi} \end{pmatrix} = \begin{pmatrix} -k_1 \dfrac{3\left(Z_i - Z_{M1}\right)\left(X_i - X_{M1}\right)}{\left(\sqrt{\left(X_i - X_{M1}\right)^2 + \left(Y_i - Y_{M1}\right)^2 + \left(Z_i - Z_{M1}\right)^2}\right)^5} \\ -k_1 \dfrac{3\left(Z_i - Z_{M1}\right)\left(Y_i - Y_{M1}\right)}{\left(\sqrt{\left(X_i - X_{M1}\right)^2 + \left(Y_i - Y_{M1}\right)^2 + \left(Z_i - Z_{M1}\right)^2}\right)^5} \\ -k_1 \dfrac{2\left(Z_i - Z_{M1}\right)^2 - \left(X_i - X_{M1}\right)^2 - \left(Y_i - Y_{M1}\right)^2}{\left(\sqrt{\left(X_i - X_{M1}\right)^2 + \left(Y_i - Y_{M1}\right)^2 + \left(Z_i - Z_{M1}\right)^2}\right)^5} \end{pmatrix} \tag{5.5a}$$

$$\begin{pmatrix} B_{M2Xi} \\ B_{M2Yi} \\ B_{M2Zi} \end{pmatrix} = \begin{pmatrix} -k_2 \dfrac{3\left(Z_i - Z_{M2}\right)\left(X_i - X_{M2}\right)}{\left(\sqrt{\left(X_i - X_{M2}\right)^2 + \left(Y_i - Y_{M2}\right)^2 + \left(Z_i - Z_{M2}\right)^2}\right)^5} \\ -k_2 \dfrac{3\left(Z_i - Z_{M2}\right)\left(Y_i - Y_{M2}\right)}{\left(\sqrt{\left(X_i - X_{M2}\right)^2 + \left(Y_i - Y_{M2}\right)^2 + \left(Z_i - Z_{M2}\right)^2}\right)^5} \\ -k_2 \dfrac{2\left(Z_i - Z_{M}\right)^2 - \left(X_i - X_{M}\right)^2 - \left(Y_i - Y_{M}\right)^2}{\left(\sqrt{\left(X_i - X_{M2}\right)^2 + \left(Y_i - Y_{M2}\right)^2 + \left(Z_i - Z_{M2}\right)^2}\right)^5} \end{pmatrix} \tag{5.5b}$$

Here, k_1 and k_2 represent the strength factors of the two magnets in nT·m^3. They can be calculated from the maximum residual flux density (or Br) of the magnets.

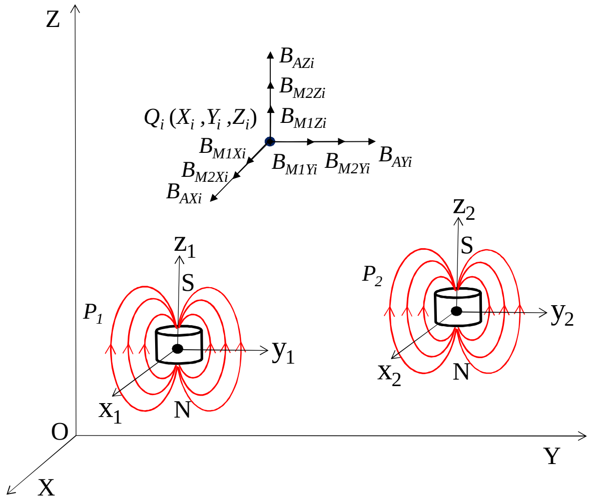

Figure 5.20. Two magnets and various magnetic field measurements in O-XYZ system.

To locate the two smart rocks, an objective error function is defined as a SRSS difference between the predicted and the measured magnetic field intensities at all measurement points $Q_i\,(X_i, Y_i, Z_i)$ ($i=1, 2, \dots, n$). That is,

$$J(X_{M1}, Y_{M1}, Z_{M1}; X_{M2}, Y_{M2}, Z_{M2}) = \sqrt{\sum_{i=1}^{n}[B_{Ti}^{(P)} - B_{Ti}^{(M)}]^2} \tag{5.6}$$

The objective error function in Eq. (5.6) is minimized to derive the coordinates of the two smart rocks, $P_1\,(X_{M1}, Y_{M1}, Z_{M1})$ and $P_2\,(X_{M2}, Y_{M2}, Z_{M2})$.

5.3.5. Test Results and Discussion. In this section, the localization of the SR3 deployed near the south abutment at the first series field test was conducted. For the second series field test, the location of single smart rock SR1 deployed near Bent 2 was firstly predicted and then the localization of two smart rocks was evaluated.

5.3.5.1 Field tests near the south abutment. Table 5.6 summarizes the coordinates of 18 measurement points near the south abutment, the AMF intensities, and the total intensities after deployment of the smart rock SR3. The coefficient $k = 86521\ nT.m^3$ for two stacked N42 magnets is calculated from the maximum residual flux density. The three components of the AMF ($B^{(M)}_{Ax}$, $B^{(M)}_{Ay}$, $B^{(M)}_{Az}$) and the total magnetic field $B_T^{(M)}$ were directly measured from the 3-axis flux magnetometer in which three directions marked on the sensor were placed in parallel with the three axles of the O-XYZ coordinate system. Therefore, the magnitude of the total magnetic field and the three components of the AMF were substituted into the localization algorithm of one smart rock to determine the coordinates of the smart rock SR3.

Table 5.6. Coordinates and intensities for SR3 location

Measurement Point		Measurement Point Coordinate (m)			AMF Intensity (10^4 nT)			SR3&AMF Intensity (10^4 nT)
		X_i	Y_i	Z_i	$B_{AX}^{(M)}$	$B_{AY}^{(M)}$	$B_{AZ}^{(M)}$	$B_T^{(M)}$
P2S1	E1	0.66	42.26	-0.94	-1.868	-0.982	-4.001	4.583
	E2	0.69	42.29	-0.64	-1.867	-0.974	-4.012	4.600
	E3	0.70	42.30	-0.32	-1.865	-0.980	-4.017	4.607
	E4	0.70	42.25	-0.03	-1.866	-0.975	-4.024	4.606
	E5	0.75	42.25	0.28	-1.872	-0.974	-4.024	4.604
	E6	0.77	42.35	0.57	-1.866	-0.989	-4.023	4.599

Table 5.6. Coordinates and intensities for SR3 location (cont.)

P3S1	E1	1.69	42.29	-1.14	-1.824	-0.971	-3.997	5.139
	E2	1.75	42.30	-0.84	-1.828	-0.966	-4.018	5.019
	E3	1.68	42.25	-0.54	-1.840	-0.969	-4.031	4.871
	E4	1.69	42.27	-0.25	-1.851	-0.969	-4.044	4.804
	E5	1.71	42.28	0.06	-1.871	-0.959	-4.052	4.758
	E6	1.74	42.28	0.37	-1.888	-0.968	-4.051	4.726
P4S1	E1	2.34	42.39	-1.09	-1.641	-1.080	-4.026	5.758
	E2	2.34	42.37	-0.89	-1.656	-1.063	-4.059	5.490
	E3	2.38	42.34	-0.59	-1.676	-1.055	-4.084	5.219
	E4	2.38	42.29	-0.28	-1.697	-1.062	-4.105	5.043
	E5	2.42	42.34	0.02	-1.732	-1.059	-4.121	4.940
	E6	2.44	42.33	0.32	-1.771	-1.078	-4.123	4.888

Table 5.7 compares the predicted and measured coordinates (X_M, Y_M, Z_M) of the smart rock SR3. It can be observed that the largest error in Z coordinate is 29 cm as a result of significant swing of the sensor caused by the strong wind during the tests. The SRSS prediction error of three components is 36 cm, which is small in comparison with the error limit of half a meter.

Table 5.7. Predicted and measured location of smart rock SR3

	X_M (m)	Y_M (m)	Z_M (m)
Predicted SR3 coordinate	2.79	41.30	-2.82
Measured SR3 coordinate	2.71	41.10	-2.53
Location Prediction Error	0.08	0.20	-0.29
SRSS Error in Coordinate		0.36 m	

5.3.5.2 Field tests near Bent 2. Table 5.8 summarizes the coordinates of 39 measurement points near Bent 2, the AMF intensities prior to any smart rock deployment, and the total intensities after deployment of the smart rock SR1. The three components of the AMF and the total magnetic field were directly measured from the 3-axis magnetometer sensor oriented in parallel with the X-, Y-, and Z-axis.

Table 5.8. Coordinates and intensities for SR1 location

		Measurement Point Coordinate (m)			AMF Intensity (10^4 nT)			SR1&AMF intensity (10^4 nT)
		X_i	Y_i	Z_i	$B_{XA}^{(M)}$	$B_{YA}^{(M)}$	$B_{ZA}^{(M)}$	$B_T^{(M)}$
P1S4	E1	-2.88	29.26	-1.50	-2.087	-0.956	-4.032	4.597
	E2	-2.87	29.29	-1.21	-2.085	-0.955	-4.045	4.619
	E3	-2.85	29.33	-0.91	-2.096	-0.962	-4.050	4.639
	E4	-2.82	29.37	-0.61	-2.093	-0.967	-4.057	4.655
	E5	-2.81	29.40	-0.32	-2.097	-0.971	-4.061	4.668
	E6	-2.80	29.41	0.00	-2.102	-1.006	-4.053	4.677
P1S5	E1	-2.89	27.66	-1.51	-2.095	-0.909	-4.030	4.486
	E2	-2.87	27.68	-1.21	-2.091	-0.928	-4.042	4.506
	E3	-2.84	27.72	-0.92	-2.100	-0.940	-4.047	4.532
	E4	-2.82	27.74	-0.60	-2.100	-0.958	-4.053	4.561
	E5	-2.80	27.76	-0.31	-2.107	-0.948	-4.061	4.586
	E6	-2.78	27.78	0.00	-2.106	-0.969	-4.062	4.611
P1S7	E1	-2.84	25.29	-1.50	-2.110	-0.868	-4.029	4.581
	E2	-2.81	25.34	-1.19	-2.104	-0.880	-4.043	4.564
	E3	-2.79	25.39	-0.90	-2.112	-0.890	-4.050	4.558
	E4	-2.77	25.41	-0.59	-2.110	-0.914	-4.056	4.563
	E5	-2.75	25.46	-0.31	-2.116	-0.909	-4.064	4.574
	E6	-2.74	25.46	0.01	-2.115	-0.937	-4.065	4.588
P2S4	E1	-1.94	29.14	-1.51	-2.196	-0.946	-3.993	4.615
	E2	-1.92	29.22	-1.21	-2.207	-0.981	-4.002	4.654
	E3	-1.91	29.28	-0.91	-2.224	-1.004	-4.007	4.685
	E4	-1.89	29.30	-0.62	-2.240	-1.005	-4.014	4.707
	E5	-1.86	29.32	-0.31	-2.255	-0.998	-4.019	4.722
	E6	-1.86	29.34	-0.02	-2.267	-0.997	-4.018	4.731
	E7	-1.83	29.37	0.28	-2.278	-1.002	-4.010	4.735
P2S5	E1	-1.93	27.64	-1.52	-2.164	-0.903	-4.006	4.203
	E2	-1.91	27.66	-1.21	-2.185	-0.898	-4.023	4.318
	E3	-1.89	27.70	-0.91	-2.199	-0.927	-4.032	4.437
	E4	-1.88	27.73	-0.62	-2.215	-0.924	-4.043	4.437
	E5	-1.84	27.76	-0.32	-2.243	-0.924	-4.043	4.579
	E6	-1.84	27.78	-0.01	-2.259	-0.912	-4.046	4.626
	E7	-1.82	27.85	0.27	-2.275	-0.948	-4.033	4.660
P2S7	E1	-1.86	25.19	-1.50	-2.193	-0.854	-3.985	4.408
	E2	-1.83	25.19	-1.20	-2.212	-0.849	-4.004	4.408
	E3	-1.81	25.24	-0.91	-2.224	-0.851	-4.021	4.431
	E4	-1.79	25.26	-0.60	-2.237	-0.857	-4.033	4.471
	E5	-1.77	25.30	-0.31	-2.255	-0.860	-4.039	4.507
	E6	-1.77	25.31	-0.01	-2.270	-0.872	-4.041	4.546
	E7	-1.74	25.39	0.27	-2.282	-0.903	-4.035	4.575

Given the coordinates, AMF intensities, and total intensities at various measurement points in Table 5.8, the minimization of Eq. (5.3) yielded the predicted coordinate of the smart rock as presented in Table 5.9. By comparing the predicted coordinate with that measured from the total station, also listed in Table 5.9, a SRSS coordinate error of *0.27 m* was determined. The prediction error mainly occurred in *X* coordinate likely because the measurement points on two close paths were not distributed well and the measurement bar was inaccurately placed on top of the smart rock with *0.368 m* in diameter. Nevertheless, the prediction error of *0.27 m* is less than *0.5 m*, a target rock positioning accuracy set forth for engineering application.

Table 5.9. Predicted and measured location of smart rock SR1

Designation	X_{M1} (m)	Y_{M1} (m)	Z_{M1} (m)
Predicted SR1coordinate	-0.43	27.21	-3.13
Measured SR1coordinate	-0.20	27.17	-3.26
Prediction Error	-0.23	0.05	0.13
SRSS Error in Coordinate	0.27 m		

Table 5.10 summarizes the coordinates, the AMF intensities, and the total intensities after deployment of the two smart rocks SR1 and SR2 at 91measurement points near Bent 2 and the 52 total intensities after the smart rock SR2 was moved to a new position, designated as smart rock SR2'. The 52 measurement points were selected from the 91 points due to the limited time limit available to cover the area of two smart rocks.

Given $k = 86521\ nT.m^3$ for the two stacked N42 magnets and the coordinates, the AMF intensities, and the total intensities at various measurement points in Table 5.10, the minimization of Eq. (5.6) yielded the predicted coordinates of the two smart rocks SR1 and SR2 as presented in Table 5.11. Similarly, the predicted locations of the two smart rock of SR1 and SR2' were also evaluated as listed in Table 5.12. The predicted coordinates were compared with their corresponding ground truth data obtained from the total station. The prediction errors in component and SRSS total are also included in Tables 5.11 and 5.12 accordingly.

Table 5.10. Coordinates and intensities for SR1 and SR2 or SR2' locations

Measurement Point		Measurement Point Coordinate (m)			AMF Intensity (10^4 nT)			SR1&SR2& AMF Intensity (10^4 nT)	SR1&SR2'& AMF Intensity (10^4 nT)
		X_i	Y_i	Z_i	$B_{XA}^{(M)}$	$B_{YA}^{(M)}$	$B_{ZA}^{(M)}$	$B_T^{(M)}$	$B_T^{(M)}$
P1S1	E1	-2.92	33.04	-1.52	-2.114	-0.954	-4.036	4.545	NA
	E2	-2.90	33.06	-1.21	-2.112	-0.967	-4.042	4.576	
	E3	-2.88	33.09	-0.91	-2.112	-0.994	-4.043	4.605	
	E4	-2.86	33.11	-0.60	-2.116	-0.994	-4.046	4.629	
	E5	-2.84	33.17	-0.32	-2.121	-1.013	-4.043	4.648	
	E6	-2.83	33.20	-0.01	-2.122	-1.011	-4.045	4.662	
P1S2	E1	-2.90	31.97	-1.52	-2.105	-0.992	-4.029	4.471	4.493
	E2	-2.88	32.00	-1.21	-2.099	-0.991	-4.042	4.527	4.519
	E3	-2.86	32.06	-0.91	-2.105	-0.982	-4.049	4.577	4.544
	E4	-2.84	32.08	-0.61	-2.106	-0.992	-4.053	4.617	4.566
	E5	-2.82	32.11	-0.32	-2.108	-1.012	-4.052	4.645	4.584
	E6	-2.80	32.10	0.00	-2.109	-1.037	-4.047	4.666	4.593
P1S3	E1	-2.86	30.70	-1.51	-2.088	-0.965	-4.037	4.361	4.442
	E2	-2.85	30.70	-1.21	-2.087	-1.000	-4.040	4.451	4.478
	E3	-2.83	30.74	-0.92	-2.089	-1.027	-4.041	4.525	4.512
	E4	-2.81	30.77	-0.61	-2.092	-1.025	-4.048	4.585	4.541
	E5	-2.79	30.80	-0.32	-2.097	-1.026	-4.051	4.628	4.565
	E6	-2.77	30.83	-0.02	-2.101	-1.045	-4.043	4.655	4.583
P1S4	E1	-2.82	29.15	-1.53	-2.087	-0.956	-4.032	4.321	NA
	E2	-2.82	29.13	-1.22	-2.085	-0.955	-4.045	4.391	
	E3	-2.79	29.17	-0.93	-2.096	-0.962	-4.050	4.455	
	E4	-2.78	29.19	-0.60	-2.093	-0.967	-4.057	4.516	
	E5	-2.75	29.23	-0.32	-2.097	-0.971	-4.061	4.562	
	E6	-2.74	29.23	-0.01	-2.102	-1.006	-4.053	4.597	
P1S5	E1	-2.78	27.46	-1.52	-2.095	-0.909	-4.030	4.305	4.295
	E2	-2.76	27.47	-1.22	-2.091	-0.928	-4.042	4.336	4.333
	E3	-2.73	27.50	-0.92	-2.100	-0.940	-4.047	4.379	4.373
	E4	-2.72	27.52	-0.62	-2.100	-0.958	-4.053	4.429	4.418
	E5	-2.71	27.57	-0.32	-2.107	-0.948	-4.061	4.474	4.457
	E6	-2.69	27.61	-0.02	-2.106	-0.969	-4.062	4.518	4.495
P1S6	E1	-2.73	26.33	-1.51	-2.097	-0.854	-4.038	4.378	4.337
	E2	-2.71	26.37	-1.21	-2.088	-0.872	-4.053	4.371	4.338
	E3	-2.69	26.42	-0.91	-2.097	-0.876	-4.060	4.389	4.359
	E4	-2.67	26.45	-0.61	-2.106	-0.893	-4.063	4.420	4.391
	E5	-2.64	26.48	-0.33	-2.109	-0.912	-4.067	4.454	4.425
	E6	-2.64	26.48	-0.01	-2.106	-0.931	-4.070	4.494	4.461

Table 5.10. Coordinates and intensities for SR1 and SR2 or SR2' locations (cont.)

P1S7	E1	-2.84	25.29	-1.50	-2.110	-0.868	-4.029	4.505	NA
	E2	-2.81	25.34	-1.19	-2.104	-0.880	-4.043	4.490	
	E3	-2.79	25.39	-0.90	-2.112	-0.890	-4.050	4.490	
	E4	-2.77	25.41	-0.59	-2.110	-0.914	-4.056	4.498	
	E5	-2.75	25.46	-0.31	-2.116	-0.909	-4.064	4.511	
	E6	-2.74	25.46	0.01	-2.115	-0.937	-4.065	4.530	
P2S1	E1	-1.94	33.08	-1.52	-2.167	-0.951	-4.024	4.561	4.535
	E2	-1.94	33.14	-1.23	-2.176	-0.973	-4.033	4.622	4.573
	E3	-1.92	33.20	-0.92	-2.190	-0.994	-4.038	4.672	4.608
	E4	-1.89	33.21	-0.62	-2.203	-0.995	-4.045	4.710	4.637
	E5	-1.88	33.25	-0.33	-2.224	-0.996	-4.044	4.736	4.661
	E6	-1.86	33.25	-0.02	-2.236	-0.984	-4.046	4.753	4.674
	E7	-1.84	33.30	0.26	-2.253	-0.984	-4.036	4.758	4.679
P2S2	E1	-1.93	32.04	-1.51	-2.232	-0.976	-3.980	4.525	NA
	E2	-1.91	32.05	-1.22	-2.247	-0.997	-3.990	4.645	
	E3	-1.89	32.08	-0.92	-2.260	-1.000	-4.001	4.725	
	E4	-1.87	32.10	-0.62	-2.278	-1.010	-4.005	4.775	
	E5	-1.85	32.15	-0.33	-2.293	-1.006	-4.007	4.801	
	E6	-1.84	32.16	-0.02	-2.310	-0.998	-4.004	4.810	
	E7	-1.81	32.25	0.27	-2.319	-1.005	-3.994	4.805	
P2S3	E1	-1.93	30.96	-1.51	-2.209	-0.966	-3.983	4.506	4.400
	E2	-1.91	31.00	-1.20	-2.219	-0.963	-4.001	4.696	4.491
	E3	-1.89	31.05	-0.92	-2.234	-0.967	-4.012	4.799	4.565
	E4	-1.86	31.07	-0.61	-2.248	-0.970	-4.019	4.850	4.620
	E5	-1.85	31.11	-0.33	-2.267	-0.978	-4.018	4.865	4.657
	E6	-1.83	31.12	-0.01	-2.278	-0.988	-4.014	4.860	4.679
	E7	-1.80	31.16	0.28	-2.291	-0.991	-4.003	4.845	4.686
P2S4	E1	-1.95	29.27	-1.51	-2.186	-0.946	-3.993	4.283	NA
	E2	-1.93	29.27	-1.21	-2.197	-0.981	-4.002	4.451	
	E3	-1.92	29.32	-0.92	-2.214	-1.004	-4.007	4.576	
	E4	-1.90	29.34	-0.61	-2.230	-1.005	-4.014	4.660	
	E5	-1.87	29.38	-0.32	-2.245	-0.998	-4.019	4.716	
	E6	-1.86	29.39	-0.02	-2.257	-0.997	-4.018	4.744	
	E7	-1.85	29.43	0.28	-2.268	-1.002	-4.010	4.758	
P2S5	E1	-1.94	27.66	-1.52	-2.154	-0.903	-4.006	4.022	4.107
	E2	-1.93	27.70	-1.21	-2.175	-0.898	-4.023	4.176	4.229
	E3	-1.91	27.75	-0.92	-2.189	-0.927	-4.032	4.308	4.335

Table 5.10. Coordinates and intensities for SR1 and SR2 or SR2' locations (cont.)

P2S5	E4	-1.89	27.77	-0.61	-2.205	-0.924	-4.043	4.414	4.421
	E5	-1.87	27.79	-0.33	-2.233	-0.924	-4.043	4.498	4.492
	E6	-1.84	27.80	-0.01	-2.249	-0.912	-4.046	4.564	4.542
	E7	-1.82	27.85	0.27	-2.265	-0.948	-4.033	4.613	4.587
P2S6	E1	-1.91	26.42	-1.51	-2.158	-0.877	-3.999	3.979	NA
	E2	-1.88	26.43	-1.21	-2.177	-0.885	-4.015	4.065	
	E3	-1.86	26.46	-0.92	-2.194	-0.917	-4.023	4.177	
	E4	-1.85	26.49	-0.62	-2.215	-0.927	-4.031	4.289	
	E5	-1.82	26.54	-0.33	-2.231	-0.924	-4.038	4.383	
	E6	-1.81	26.52	-0.01	-2.248	-0.913	-4.044	4.464	
	E7	-1.78	26.57	0.27	-2.268	-0.926	-4.037	4.522	
P2S7	E1	-1.86	25.12	-1.51	-2.183	-0.854	-3.985	4.344	4.288
	E2	-1.84	25.18	-1.21	-2.202	-0.849	-4.004	4.342	4.280
	E3	-1.82	25.22	-0.91	-2.214	-0.851	-4.021	4.369	4.313
	E4	-1.80	25.25	-0.61	-2.227	-0.857	-4.033	4.408	4.357
	E5	-1.77	25.27	-0.32	-2.245	-0.860	-4.039	4.452	4.402
	E6	-1.75	25.28	-0.01	-2.260	-0.872	-4.041	4.496	4.447
	E7	-1.73	25.32	0.28	-2.272	-0.903	-4.035	4.529	4.483

Table 5.11. Predicted and measured locations of two smart rocks SR1 & SR2

	SR1			SR2		
	X_{M1} (m)	Y_{M1} (m)	Z_{M1} (m)	X_{M2} (m)	Y_{M2} (m)	Z_{M2} (m)
Predicted coordinate	0.50	26.85	-2.54	-0.90	30.28	-3.78
Measured coordinate	-0.20	27.17	-3.26	-0.40	30.55	-3.07
Prediction Error	0.70	-0.32	0.72	-0.51	-0.22	-0.71
SRSS Error	1.05 m			0.90 m		

Table 5.12. Predicted and measured locations of two smart rocks SR1 & SR2'

	SR1			SR2'		
	X_{M1} (m)	Y_{M1} (m)	Z_{M1} (m)	X_{M2} (m)	Y_{M2} (m)	Z_{M2} (m)
Predicted coordinate	0.36	26.78	-2.44	0.19	31.64	-4.05
Measured coordinate	-0.20	27.17	-3.26	0.59	30.41	-3.21
Prediction Error	0.56	-0.39	0.82	-0.40	1.23	-0.84
SRSS Error	1.07 m			1.54 m		

It can be calculated from the measured coordinates of SR1 and SR2 as listed in Table 5.11 that SR1 and SR2 were spaced by *3.40 m*. The SRSS prediction errors were determined to be *1.05 m* and *1.18 m* for the predication of SR1 and SR2 locations, respectively. The errors in *Y* coordinate were smaller than those in X and Z coordinate. likely because the measurement points covered a large area of the two smart rocks in Y direction (7 m) and a small area in X direction (1 m) and Z direction (1.5 m). In addition, most measurement points were positioned on one side of the smart rocks in X and Z directions. As discussed in Sections 3 and 4, the more uniformly distributed the measurement points are around a smart rock, the more accurate the localization of the smart rock.

The smart rock SR2 was moved to SR2' by *1.01 m* towards the pier based on the measured coordinates in Tables 5.11 and 5.12. It can also be calculated from the measured coordinates of SR1 and SR2' in Table 5.12 that SR1 and SR2' were spaced by *3.34 m*. In terms of location predication, the SRSS prediction errors were determined to be *1.07 m* and *1.54 m* for SR1 and SR2', respectively. While the location prediction error for SR1 together with smart rock SR2 versus SR2' is close, the location error for SR2' is significantly higher than that for SR2 mainly because the number of measurement points was reduced from 91 to 52. Indeed, by comparing Table 5.12 with Table 5.11, it can be found that the increase in prediction error from SR2 to SR2' location mainly occurred in Y direction, which is from *-0.22 m* to *1.23 m*. In addition, SR2' was closer to the bridge pier than SR2, and its APUS mechanism may be slightly more affected by the steel reinforcement in the pier.

Figure 5.21 displays the measured locations of smart rocks SR1, SR2, and SR2' on the upstream riverbed profile near Bent 2. The three-dimensional contour map was created in ArcGIS based on the riverbed survey data collected with the sonar and the total station in the Cartesian coordinate system O-XYZ. It can be seen that the smart rock SR2' was moved closer to the pier and settled down to the scour hole around the pier. It is noted that one smart rock SR1 alone can be tracked as it moves over time as demonstrated at the I-44W Roubidoux Creek Bridge site in Missouri.

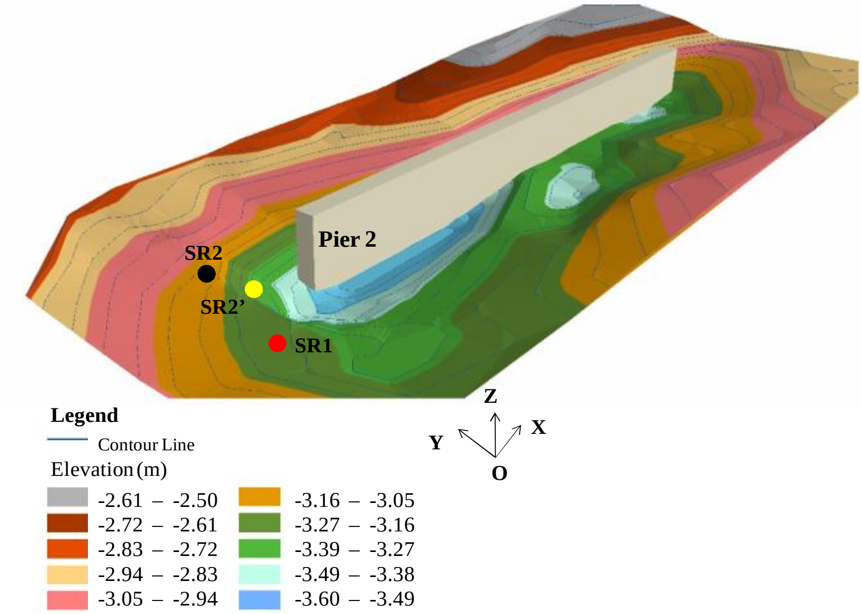

Figure 5.21. Two smart rock locations near the scour hole around Bent 2.

5.4. US HIGHWAY 63 GASCONADE RIVER BRIDGE

In this section, the US Highway 63 Bridge (No. A3760) over the Gasconade River located approximately 9 km southeast of Vienna in Maries County, MO, was used as the third test site to validate the performance of a smart rock. As shown in Figure 5.22, the bridge is a 12-span continuous reinforced concrete-girder structure to support two lanes of two-way traffic on US Highway 63. Pier 4 is located in the main channel of water flow and potentially subjected to severe contraction scour and local scour, threatening the safety of the bridge during a flood season.

Figure 5.22. The US Highway 63 Gasconade River Bridge.

5.4.1. Test Setup and Layout. To date, two field tests were carried out in different seasons to validate the localization of one smart rock. Both were conducted near Bent 4 with one lane of the roadway closed for safety. Figure 5.23 shows the overall test plan and setup at the US63 bridge site. The center of a total station set on the Jefferson City side of the bridge was used as the origin of a Cartesian coordinate system O-XYZ. The test crane with an attached magnetometer sensor was mounted on a flatbed trailer towed by a truck. The trailer was parked on the bridge deck at three stops (S1, S2 and S3 with *4.5 m* equal spacing) along each of the two paths (P1 and P2 with *2 m* spacing). For each stop, seven elevations (E1, E2, E3, E4, E5, E6 and E7 with *0.3 m* equal spacing) were considered for magnetic field measurements. Therefore, a total of 42 measurements were taken near Bent 4 in order to locate the smart rock SR1. The total station was used to survey the smart rock and the magnetometer sensor for ground truth coordinate data.

5.4.2. Test Procedure. (1) *Set the XYZ Coordinate System*. As shown in Figure 5.24, the total station was set near Bent 1 for its line of sight to the magnetometer sensor, which is referred to as Point O at the origin of the global coordinate system O-XYZ. The Y-axis was set along the south-bound traffic direction towards Rolla, MO. The X-axis was set to be perpendicular to the Y-axis in horizontal plane, pointing to the upstream of the river. The Z-axis points upward according to the right-hand rule. A permanent point A on the bridge railing was surveyed for future reference.

(2) *Assemble the Test Crane*. As indicated in Figures 5.23(b), the forklift was first set and tied to a flatbed trailer. The horizontal aluminum arm was then installed and ten segments of carbon fiber tubes with *1.0 m* each were assembled to lower down the measurement points from the bridge deck. Finally, the horizontal bar was connected to the bottom tube to support the magnetometer sensor and prisms for coordinate measurement.

(3) *Set up the STL Digital Magnetometer*. As shown in Figure 5.23(b), the magnetometer sensor was connected with an Ethernet cable to the laptop computer through a mini Ethernet box set on a table. The computer included special software for sensor control and the measurement of magnetic fields. The sensor and computer were charged by two portable batteries.

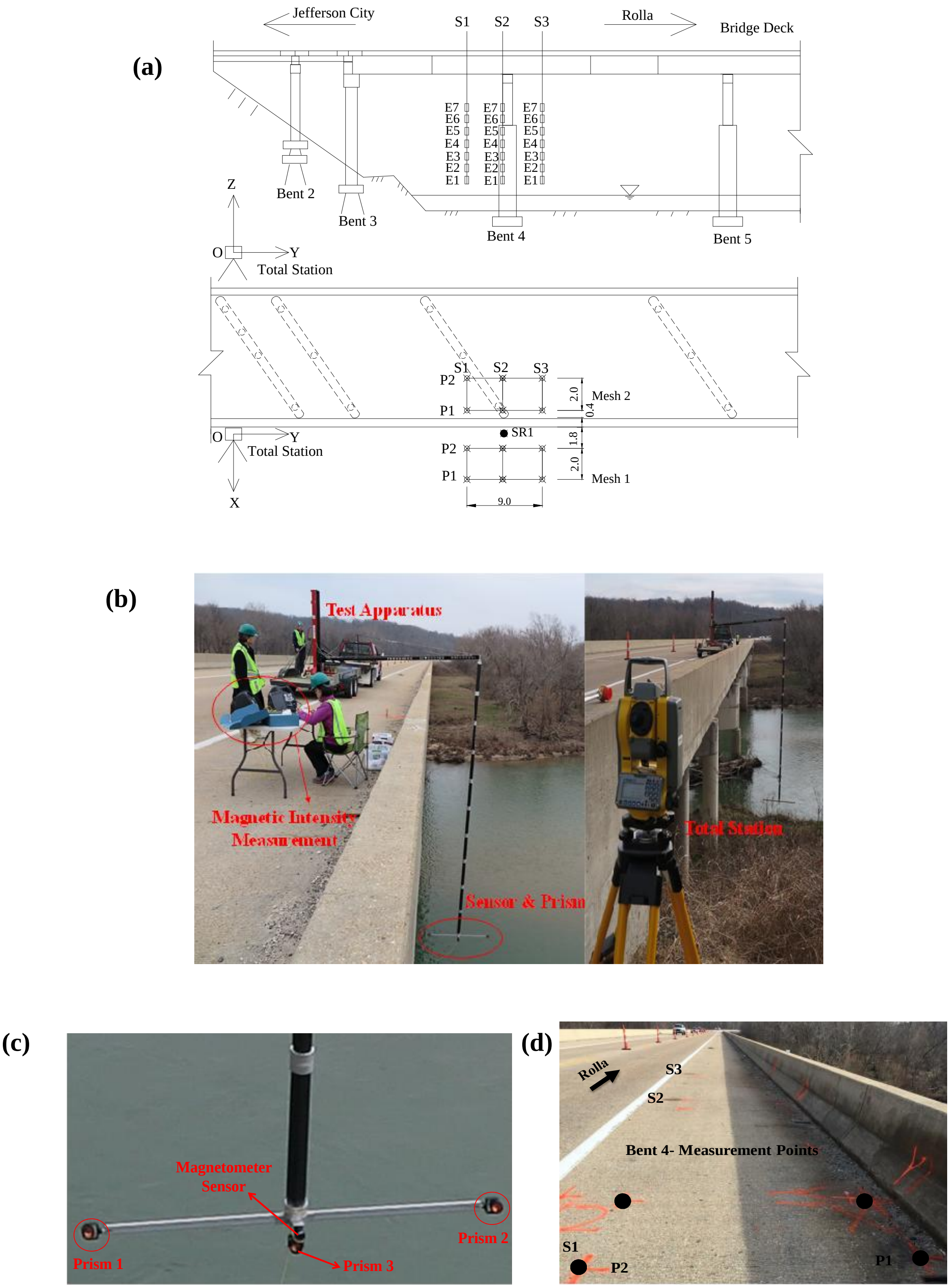

Figure 5.23. US63 Bridge site: (a) planning (unit: m), (b) test setup, (c) sensor and prisms positions, and (d) forklift positions.

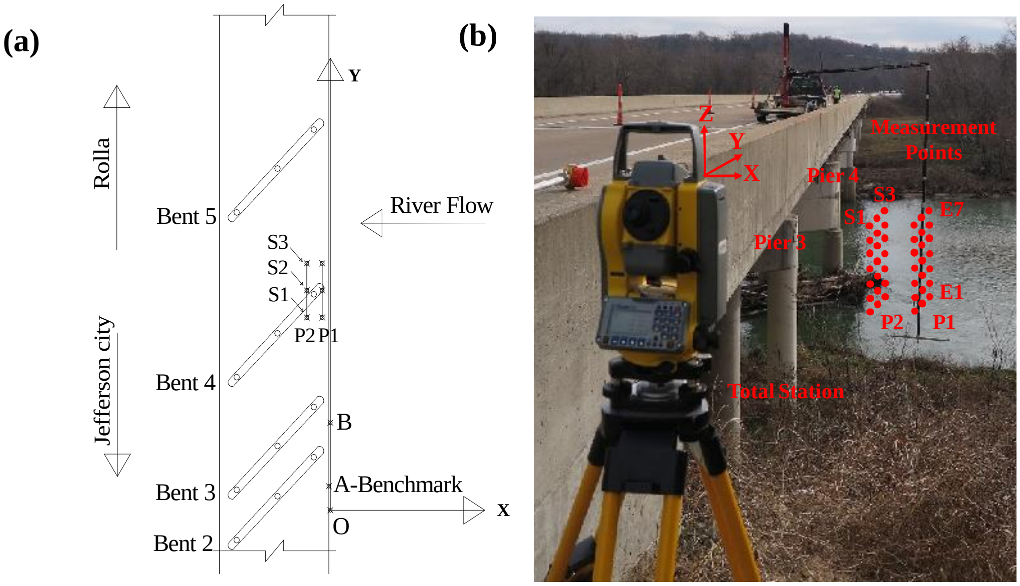

Figure 5.24. Selection of the global coordinate system.

(4) *Measure the Ambient Magnetic Field*. The ambient magnetic field is generated by the Earth and nearby ferromagnetic objects. It was measured prior to the deployment of the smart rock, following the (path, stop, elevation) sequence as shown in Figure 5.25(a). Figure 5.25(b) illustrates one stop of the forklift at P2S2 when the trailer was parked at the marked location. At this stop, measurements (both coordinate and magnetic field intensity) were taken at seven elevations. Note that one forklift position on the bridge deck is related to seven sensor positions by moving the forklift up and down as indicated in Figure 5.24(b).

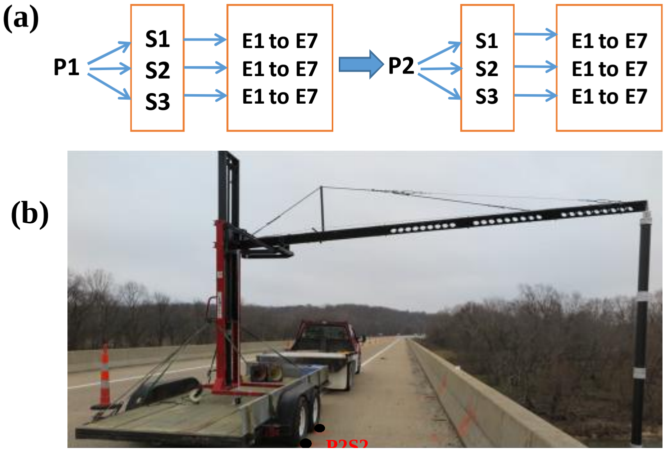

Figure 5.25. Measurement sequence with example measurement points at P2S2.

(5) *Deploy or inspect the smart rock and measure its coordinates*. During the first series of tests, one smart rock SR1 with one N45 magnet in the APUS configuration as shown in Figure 5.26 was dropped from the bridge deck into water around the upstream side of Bent 4 for maximum scour depth monitoring. The smart rock was tied to a rope and lowered down from the bridge deck to the river bottom at the predetermined area as indicated in Figure 5.27. Due to strong water current at the time, it was determined to be unsafe to ride a small boat around the deployed smart rock and get its location measured with a total station. During the second series of field tests, it was found that the smart rock deployed previously was washed away during the December 2015 flood. Thus, another smart rock SR1 (identical to the previous one) was deployed during the second series of field tests. This time, however, the smart rock was buried in the riverbed such that the top of the smart rock was flush with the riverbed surface to make it more difficult to be washed away. The smart rock was surveyed with the total station for ground truth coordinate data.

(6) *Measure the Total Magnetic Field*. After the deployment of the smart rock during the first or second series of field tests, the total magnetic field combining the effects of the smart rock and the ambient magnetic field was measured following the same sequence as used for ambient magnetic field measurement, as shown in Figure 5.25

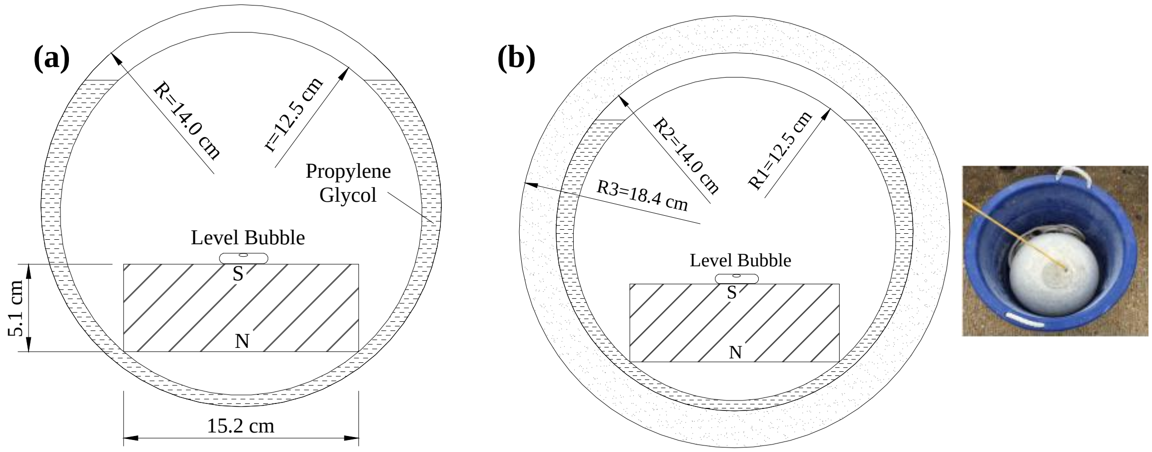

Figure 5.26. Design of smart rock SR1: (a) schematic view and (b) prototype.

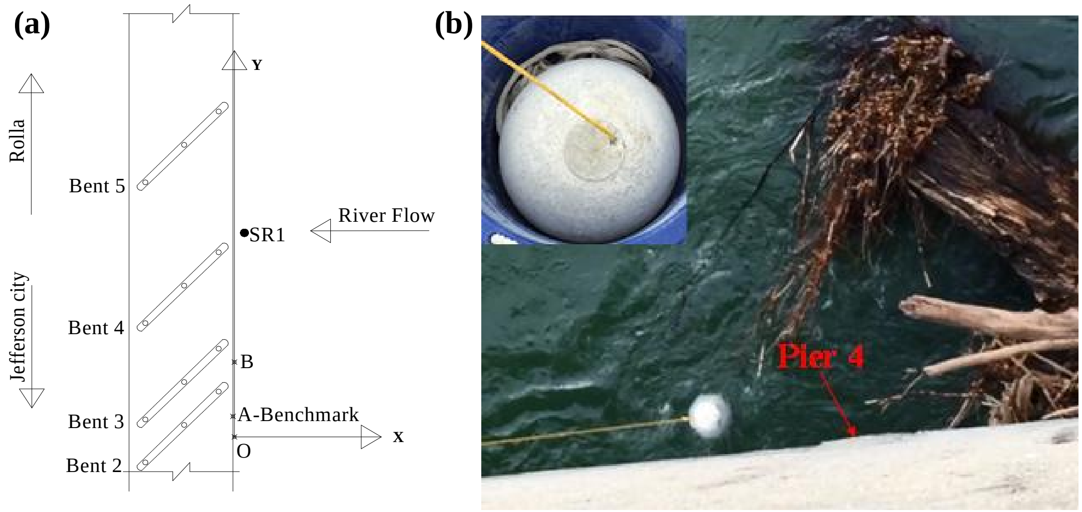

Figure 5.27. Smart rock SR1: (a) location and (b) deployment.

5.4.3. Test Results and Discussion. Eqs. (5.1-5.3) were used to locate the smart rock based on the measured coordinates, ambient and total magnetic fields at various measurement points near Bent 4 of the Gasconade River Bridge. The first series of field tests were carried out on December 11, 2015. Since the ground truth data of the smart rock was not available, the prediction error cannot be evaluated.

The second series of field tests were performed on October 18, 2016. Table 5.13 summarizes the coordinates, the AMF intensities prior to deployment of the smart rock, and the total intensities after deployment of the smart rock SR1 at 42 measurement points. Given $k = 101770\ nT.m^3$ for the N45 magnet calculated from the maximum residual flux density, the measured total magnetic field ($B_T^{(M)}$) and the three components ($B^{(M)}_{AX}$, $B^{(M)}_{AY}$ and $B^{(M)}_{AZ}$) of the ambient magnetic field, the coordinate of the smart rock SR1 was determined, which is listed in Table 5.14.

Table 5.13. Coordinates and magnetic field intensities at measurement points

Measurement Point	Measurement Point Coordinate (m)				AMF Intensity (10^4 nT)			SR1&AMF Intensity (10^4 nT)
		X_i	Y_i	Z_i	$B_{AX}^{(M)}$	$B_{AY}^{(M)}$	$B_{AZ}^{(M)}$	$B_T^{(M)}$
P1S1	E1	-3.06	64.04	-11.35	-1.605	-0.557	-4.767	5.093
	E2	-3.12	64.02	-11.02	-1.601	-0.536	-4.766	5.085
	E3	-3.10	64.06	-10.75	-1.630	-0.548	-4.750	5.079

Table 5.13. Coordinates and magnetic field intensities at measurement points (cont.)

P1S1	E4	-3.11	64.02	-10.43	-1.626	-0.525	-4.750	5.072
	E5	-3.10	64.03	-10.13	-1.629	-0.514	-4.744	5.066
	E6	-3.09	64.04	-9.82	-1.635	-0.520	-4.735	5.058
	E7	-3.11	64.06	-9.56	-1.646	-0.508	-4.726	5.052
P1S2	E1	-3.25	68.53	-11.42	-1.676	-0.667	-4.685	5.052
	E2	-3.29	68.56	-11.09	-1.644	-0.663	-4.691	5.046
	E3	-3.27	68.59	-10.82	-1.705	-0.692	-4.662	5.041
	E4	-3.26	68.50	-10.50	-1.710	-0.673	-4.660	5.035
	E5	-3.26	68.53	-10.21	-1.696	-0.733	-4.649	5.031
	E6	-3.27	68.54	-9.90	-1.681	-0.667	-4.660	5.025
	E7	-3.29	68.54	-9.61	-1.731	-0.651	-4.642	5.018
P1S3	E1	-3.10	73.07	-11.51	-1.754	-0.801	-4.625	5.016
	E2	-3.10	72.94	-11.14	-1.774	-0.781	-4.617	5.012
	E3	-3.11	72.98	-10.88	-1.771	-0.730	-4.621	5.008
	E4	-3.12	73.00	-10.55	-1.794	-0.736	-4.608	5.004
	E5	-3.13	73.00	-10.26	-1.797	-0.758	-4.598	5.000
	E6	-3.13	73.00	-9.97	-1.790	-0.746	-4.597	4.996
	E7	-3.13	73.04	-9.67	-1.827	-0.744	-4.580	4.992
P2S1	E1	-1.26	64.13	-11.31	-1.633	-0.513	-4.739	5.089
	E2	-1.29	64.13	-10.99	-1.651	-0.496	-4.730	5.078
	E3	-1.28	64.10	-10.69	-1.648	-0.470	-4.730	5.068
	E4	-1.31	64.08	-10.39	-1.654	-0.456	-4.724	5.057
	E5	-1.27	64.14	-10.11	-1.654	-0.490	-4.712	5.047
	E6	-1.26	64.11	-9.82	-1.626	-0.404	-4.726	5.038
	E7	-1.27	64.14	-9.51	-1.658	-0.445	-4.699	5.027
P2S2	E1	-0.97	68.69	-11.36	-1.717	-0.672	-4.621	5.019
	E2	-1.14	68.70	-11.08	-1.719	-0.620	-4.624	5.012
	E3	-1.16	68.68	-10.77	-1.726	-0.645	-4.611	5.002
	E4	-1.16	68.64	-10.48	-1.731	-0.672	-4.598	4.993
	E5	-1.15	68.61	-10.17	-1.738	-0.629	-4.597	4.982
	E6	-1.14	68.64	-9.86	-1.735	-0.608	-4.594	4.974
	E7	-1.16	68.63	-9.58	-1.752	-0.565	-4.587	4.963
P2S3	E1	-1.18	73.00	-11.46	-1.750	-0.757	-4.573	4.962
	E2	-1.17	72.93	-11.13	-1.778	-0.693	-4.565	4.956
	E3	-1.20	73.00	-10.86	-1.765	-0.702	-4.559	4.948
	E4	-1.21	72.98	-10.55	-1.777	-0.727	-4.542	4.940
	E5	-1.18	72.97	-10.26	-1.795	-0.682	-4.535	4.933
	E6	-1.21	72.99	-9.96	-1.784	-0.698	-4.526	4.924
	E7	-1.21	72.94	-9.64	-1.778	-0.672	-4.522	4.917

Table 5.14. Predicted and measured location of smart rock SR1

Coordinate	X_M (m)	Y_M (m)	Z_M (m)
Predicted	0.15	66.30	-17.71
Measured	0.41	66.02	-17.46
Prediction Error	-0.26	0.28	0.25
SRSS Total Error		0.46 m	

Table 5.14 summarizes the measured and predicted coordinates (X_M, Y_M, Z_M) of the smart rock SR1. Figure 5.28 shows both the measured (M_SR1) and the predicted (P_SR1) locations on the three-dimensional contour map of the riverbed in the coordinate system O-XYZ. The prediction error in rock positioning was *0.46 m*, which is less than the error limit of *0.5 m* for engineering application. This level of error is much larger than that at other bridge sites mainly because of the high elevation of the Gasconade River Bridge and thus large measurement distance up to *8m*.

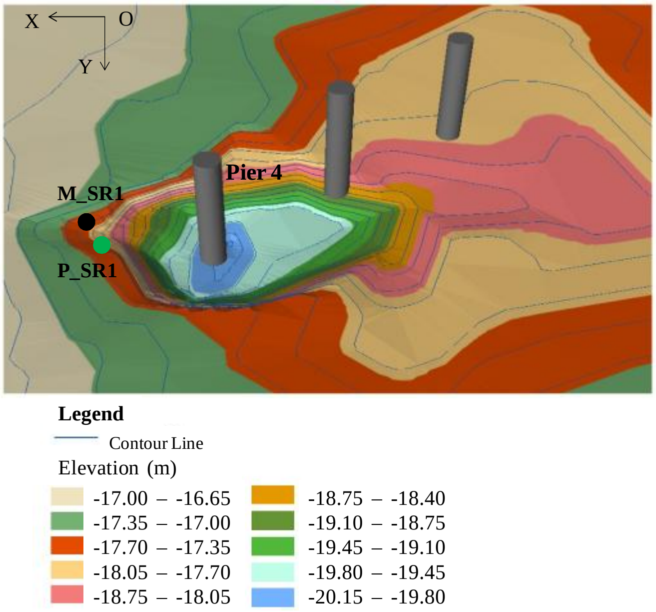

Figure 5.28. The measured and predicted smart rock locations on the riverbed profile.

5.5. SUMMARY

In this section, the smart rock technology developed and validated in Sections 2 to 4 was applied and further validated at three bridge sites (one in California and two in

Missouri) for monitoring of scour depth or riprap effectiveness. The smart rocks with an automatically pointing upward system (APUS) were deployed around the scour critical pier or abutment. Their location and movement were evaluated based on an optimization algorithm using the measured ambient (three components) and total magnetic fields at various measurement points around the smart rocks. All measurements were taken on the bridge deck using a commercial digital 3-axis magnetometer. A custom-designed test crane was built to support the magnetometer sensor, and mounted on a flatbed trailer to facilitate the field measurement above water at close distance to the deployed smart rock. A total station was used to survey the deployed smart rocks and measurement points for ground truth coordinate data for comparison with the predicted smart rock locations in field performance evaluation of the smart rock.

The localization of single smart rocks deployed at the three bridge sites was successful with a prediction error of less than 0.5 m, a target rock positioning accuracy set forth for engineering application. However, the localization for two smart rocks deployed at the Highway 1 Waddell Creek Bridge site requires further studies. The two smart rocks were difficult to locate individually. The localization error at the bridge site exceeded *1 m*, which is unsatisfactory in application.

The smart rock movement was discussed only at the I-44 Roubidoux Creek Bridge site based on the available field measurements in different seasons. The predicted displacements were in general agreement with the ground truth data. The prediction error was likely caused by potentially misplaced measurement bar in the process of smart rock survey.

The spherical smart rock directly placed between riprap rocks on the abutment embankment of the Waddell Creek Bridge was unstable due to lack of interlock with the natural rocks. They were washed away during high tide waves from the Pacific Ocean. Smart rocks directly placed on top of the riverbed at the Waddell Creek Bridge and US63 Gasconade River Bridge sites were also washed away due to high tides and the December 27, 2015, flood, respectively. Additional smart rocks were thus deployed for future monitoring by making them flush with the riverbed surface.

6. SEMI-ACTIVE SMART ROCKS FOR DIFFERENTIABLE, ACCURATE, AND RAPID POSITIONING: A PROOF-OF-CONCEPT STUDY

6.1. INTRODUCTION

In the previous sections, one or two magnets were embedded in concrete and deployed as field agents to provide their position information for bridge scour monitoring through remote magnetic field measurements with a magnetometer. The magnets remained stationary during a short period (seconds) of each measurement. Therefore, they are referred to as passive smart rocks. Passive smart rocks are cost effective and simple in design and operation. However, the magnetic field measured with the magnetometer represents a lumped effect of all smart rocks deployed near a bridge pier or abutment, the Earth, and other ferromagnetic substances. It is difficult to locate individual smart rocks as demonstrated at the Waddell Creek Bridge site, CA. In addition, the magnetic field of the magnets is generally small in comparison with the Earth's magnetic field and may further be contaminated by the presence of nearby ferromagnetic substances such as underground metal objects and steel reinforcement in a bridge pier and deck. It also depends upon the N-S pole orientation of the magnets.

In this study, semi-active smart rocks are proposed and developed to overcome the above difficulties by improving differentiability, accuracy, and efficiency in rock positioning. Each semi-active smart rock consists of a specially-designed permanent magnet system, a magnet rotation mechanism, an electric coil with many turns, and necessary electronics such as rock ID and battery indicator. The concept of semi-active smart rocks and their operation principle are first presented. A small-scale and a full-size semi-active smart rock are then designed with an automatically pointing south system (APSS) and prototyped to make the included magnet rotate according to a pre-determined time-varying current applied through the coil. Next, they are characterized for rise time, dynamic range, data repeatability, differentiability from other ferromagnetic substances, and localization accuracy. Finally, they are validated in an open field where a total magnetic field of the Earth, the magnet, the current coil, and any nearby ferromagnetic substances is measured.

6.2. SEMI-ACTIVE SMART ROCKS

To overcome the practical challenges associated with the static magnetic field measurement of a passive smart rock, one strategy is to make the magnet inside a rock rotate in a controllable fashion so that a time-varying magnetic field is generated and measured. Once embedded in concrete, the resulting unit is referred to as a semi-active smart rock since the total magnetic field intensity measured by a magnetometer includes the effect of external power and excitation to rotate the magnet.

6.2.1. Concept and Operation Principle. The main goal of developing semi-active smart rocks is to improve differentiability, accuracy, and efficiency in rock positioning for applications in bridge scour monitoring. The differentiability is associated with how separable smart rocks are in practical application. Identification (ID) numbers can be assigned to a group of smart rocks to maximize their differentiability. The accuracy is directly transferrable to the reliability of predicted scour depths from smart rocks in application. Localization of smart rocks can be significantly improved when time-varying magnetic fields by rotating a magnet can be measured with a magnetometer. Time efficiency in locating smart rocks is critical in a matter of minutes in the peak of a severe flood event. Having individual IDs, time-varying characteristics, and one- or two-way communication can expedite the process of rock positioning.

Based on the above attributes, a semi-active smart rock mainly consists of a permanent magnet, a magnet rotation mechanism, an electric coil for external excitation, and necessary electronics such as rock ID and battery indicator. To rotate the magnet, external DC provided with a battery must be transformed to AC using a converter. Once powered, the current in the electric coil induces an external magnetic field that exerts a magnetic force for magnet rotation in certain direction. The total magnetic field is measured with a magnetometer while the magnet is rotating.

6.2.2. APSS with a Rotatable Magnet. To make the magnet inside a smart rock rotate with minimum energy, a mechanical mechanism is proposed and specially designed in an automatically pointing south system (APSS). The key of this mechanism is to provide a low friction or frictionless interface between the magnet and the concrete encasement of the smart rock so that the magnet is aligned to the south direction unless disturbed with external power. Figure 6.1 illustrates such a rotating mechanism. As schematically shown in Figure 6.1(a), a cylinder magnet of 25 mm long and 11 mm in diameter is embedded in a solid acrylic sphere of 38 mm in diameter. The inner solid sphere is then enclosed by an outer spherical ball of 51 mm in diameter with the small gap in between filled with low viscosity fluid for lubrication. To manufacture the APSS, a 13 mm-diameter hole was first drilled through the center of a solid sphere at a depth of 32 mm to ensure that the magnet would be centered and balanced within the solid sphere. The hole was then filled with a two-part acrylic resin of the same specific gravity as the acrylic sphere. Next, two halves of an acrylic ball were placed outside the solid sphere and sealed with the acrylic resin. Finally, a tiny hole was drilled through the outer ball and sealed with the acrylic resin after lubrication fluid was injected to the required height. To minimize friction between the inner sphere and the outer ball as shown in Figure 6.1(a), clear silicone fluid with a low viscosity of 5 cSt (centistokes) @ 25^0C and a surface tension of 19.7 dynes/cm was selected. The low surface tension ensured less energy would be required to rotate the magnet. Figure 6.1(b) presents the finished APSS with the frictionless mechanism of a rotating magnet.

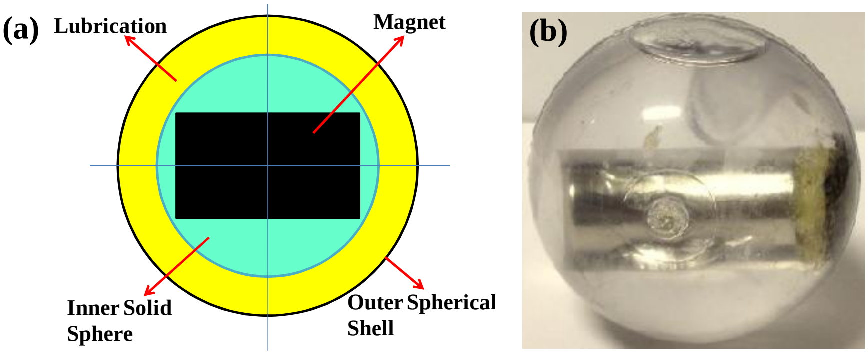

Figure 6.1. Small APSS with a rotatable magnet: (a) schematic view and (b) prototype.

Following the schematic view as shown in Figure 6.1(a), a full-size and improved APSS has already been designed and prototyped in Section 2. For completeness, a brief discussion is provided herein. The improved design consisted of one cylindrical N42 magnet with an attached level indicator, an inside organic glass ball, an outside organic glass ball, propylene glycol liquid filled in between the two balls, and distributed copper beads as balanced weights. As indicated in Figure 6.2, a level indicator was first attached to the side of the magnet that is 10.2 cm in diameter and 5.1 cm in height. The opposite side of the magnet was then glued to the surface of half of the inside ball with a diameter of 20 cm. Next, once completed, the whole inside ball was enclosed by two halves of the outside ball that is 22 cm in diameter. Finally, low friction liquid was injected into the gap between the inside and outside balls. The inside ball with the magnet and the level indicator was designed to remain in equilibrium or free to rotate when it floated in the outside ball. Therefore, the magnet in the APSS always points to the north pole of the Earth's magnetic field, which is approximately the geographical south of the Earth when no ferromagnetic substances are present within 1 m distance.

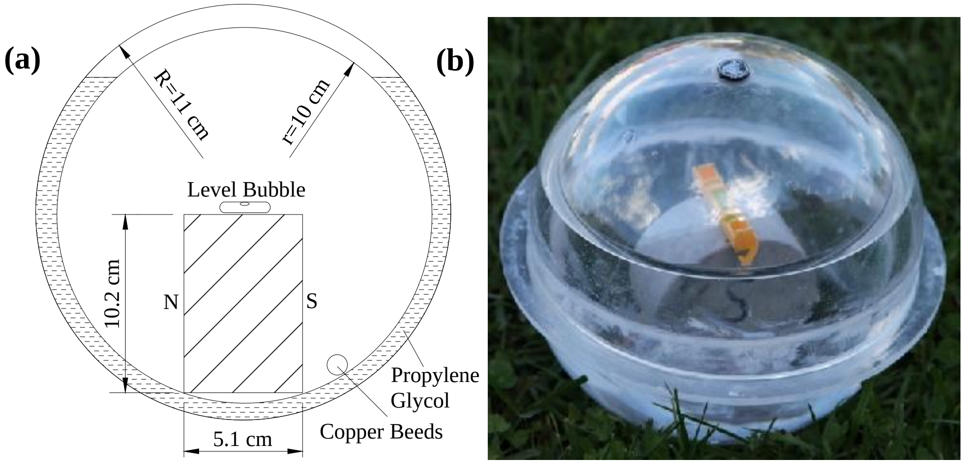

Figure 6.2. Full-size APSS: (a) design and (b) prototype.

6.2.3. Magnet Rotation Control. The rotation control of the magnet in a semi-active smart rock is provided by the circuitry of a printed circuit board (PCB) with magneto-inductive communication [104]. To rotate the magnet, a current coil of over one hundred turns was wrapped around a cylindrical core that was tightly fitted outside the encased magnet as shown in Figure 6.3(a). To control the magnet rotation, an extension board based on an H-bridge component was designed and connected to the free Input/output (I/O) pins on the PIC microcontroller of v3.0 PCB. As schematically shown in Figure 6.3(b), Input A and Input B of the H-Bridge were connected to the PIC microcontroller I/O pins. The H-bridge was connected to 6V and yielded two outputs – Output A and Output B. The coil and a series resistive load (for current limiting purpose) were connected to the H-bridge output. As current passes through the coil, a relatively strong magnetic field is generated within the coil core and the unrestrained magnet is free to rotate and aligned along the magnetic field vector or the coil axis. If the direction of current flow in coil is changed, the magnetic field vector will alternate, causing rotation of the magnet. In addition, the semi-active smart rock with the v3.0 PCB and its extension board is a comprehensive system that can be woken up by an external radio frequency (RF) signal through magneto-inductive communication, acquire data from embedded sensors as needed, and wirelessly transmit data to the base station. More importantly, the magnet inside the smart rock can be remotely rotated following a pre-programmed sequence as current was applied to the coil.

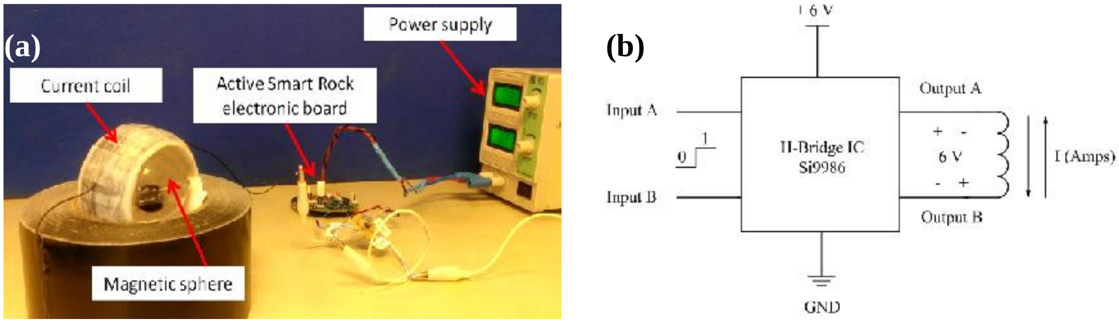

Figure 6.3. A magnet rotation system: (a) control system and (b) circuit design.

6.3. CHARACTERIZATION OF SEMI-ACTIVE SMART ROCKS

In this section, a field test using a small-scale APSS as the core of semi-active smart rock was carried out to study the feasibility and characterization of semi-active smart rock through the collected magnetic intensities over time.

6.3.1. Test Setup with a Small-scale APSS. In April, 2014, field tests were performed in an open baseball field at Ber Juan Park, Rolla, MO. As shown in Figure 6.4(a), the test setup included a free-to-rotate magnet in the APSS, a current coil on the cylindrical core, a v3.0 PCB programmed to regulate the applied current, a magnet rotating extension board, a constant power source, and a battery backup. For these tests, power was supplied by the battery that can last one hour continuously. The constant current source connected to the battery backup was employed to regulate voltage and apply current to the coil. The applied current is basically a periodical change of 0 and 1 A at a predefined interval. It has a trapezoidal pattern that increases from 0 to 1 A in a given rise time, remains at 1 A for a given duration, decreases from 1 to 0 A in the rise time, and remains at 0 A for the given duration. The duration is set equal to the rise time so that the total period for each cycle of the current supply is four times the rise time. Throughout the tests, the controllable magnet was located at the origin of a Cartesian coordinate system as displayed in Figure 6.4(b). As verified with a military compass, the axis of the coil was oriented along the North-South direction. As a result, the free-to-rotate magnet was in alignment with the coil immediately after the current was switched on. The magnetometer G858 was used to measure the total magnetic field strengths at four locations: M1 and M2 (*0.91 m* and *1.52 m* south of the magnet), and M3 and M4 (*0.91 m* and *1.52 m* west of the magnet). At each measurement point, the magnet was rotated with three current alternating rates corresponding to *0.2 sec*, *0.5 sec*, and *1.0 sec* rise times. In order to avoid its ferromagnetic effect, the power supply was placed sufficiently far away from the controllable magnet and the sensor head. The total magnetic field measured thus represented the combined effect of the Earth, the controllable magnet, and the current coil. The effect of the current coil is neglected.

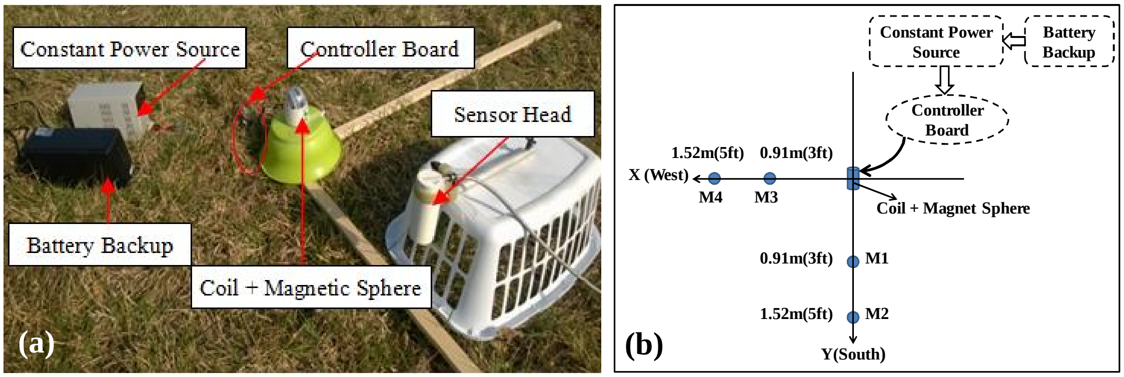

Figure 6.4. Characteristic tests at Ber Juan Park: (a) setup and (b) plan.

6.3.2. Test Data and Analysis. Figure 6.5 compares the static and time-varying magnetic field intensities measured over time at M1 location. The constant field intensity at the beginning and end of each time function represents the static magnetic field of the stationary magnet with no rotation. Each time-varying measurement includes 15 cycles of magnet rotation. It can be observed from Figure 6.5 that the time-varying magnetic intensities at *0.5 sec* and *1.0 sec* rise times are both repeatable over time with their respective periods. The high and low intensities are nearly unchanged over time. At

0.2 sec rise time, however, the high and low intensities slightly fluctuate over time. This fluctuation is governed by a balance of the overshooting inertia force and the magnetic force induced by alternating current in the coil; but it is limited by the maximum sampling rate (*10 Hz*) of the magnetometer. In this case, no temporary stop of the rotating magnet was observed.

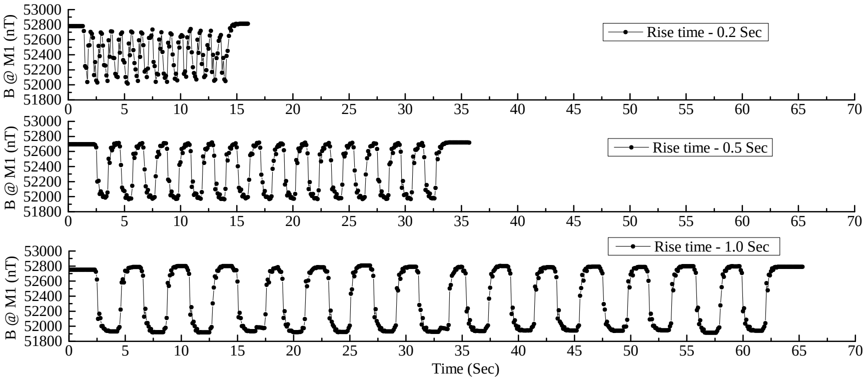

Figure 6.5. Magnetic field intensities measured at Point M1 with three rise time.

Due to the repetitive patterns and periodic characteristics, the magnetic field measurement of a magnet can be distinguished from that of surrounding ferromagnetic substances. For example, the magnetic field of a permanent magnet could be significantly weaker than the ambient magnetic field around a magnetized reinforcement cage in a bridge pier. Their fields are thus hard to differentiate from each other with static measurements. However, once rotated over time, the magnet generates unique time responses that make its localization much easier. As shown in Figure 6.5, at the beginning of tests or during the temporary stops (zero current applied), the total magnetic field intensity represents an algebraic summation of the effects of a magnet and the Earth, and thus reaches its maximum since the magnet and the Earth are aligned perfectly. When rotated for half a cycle due to the applied current (*1 A*), the magnet is in opposite alignment with the Earth, resulting in a minimum magnetic field intensity. After another half a cycle of rotation, the magnet is again in perfect alignment with the Earth, thus yielding the maximum total field intensity. This process repeats until the applied current is terminated and the magnet returns to its initial state as indicated in Figure 6.5.

Figures 6.6 shows the relative intensity, periodicity, and accuracy of magnetic fields measured at four locations with a current rise time of *0.2 sec*. In this case, the magnet continues to rotate with no temporary stop. Due to the short period (0.8 sec) of current alternation, the magnet cannot complete a full cycle of rotation and results in a slightly fluctuated field intensity that is governed by an interaction of the overshooting rotational inertia force and the magnetic force applied over time. In addition, the sample rate of *10 Hz* is too low for the magnetometer to acquire reliable data from a rapid oscillation of the magnetic field intensity over time. Therefore, a rise time of *0.2 sec* is not appropriate in application.

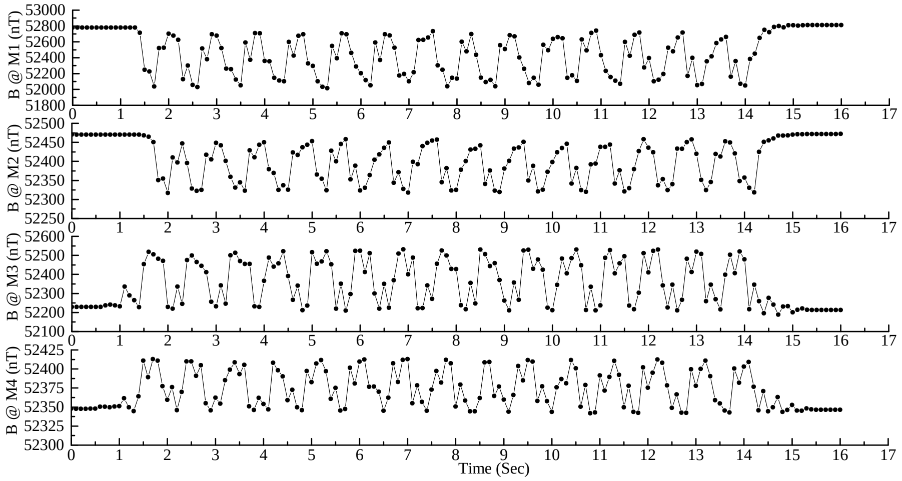

Figure 6.6. Magnetic field intensities measured at four points with a rise time of 0.2 sec.

Similarly, Figure 6.7 compares the magnetic fields measured at four locations when the coil current is applied with a rise time of *0.5 sec*. In contrast to Figure 6.6, complete cycles of magnetic field measurements are evidenced. For example, after the completion of the first half a cycle, the magnet has sufficient time to be stabilized before the next half a cycle of current is applied, resulting in low intensities at Points M1 and M2 and high intensities at Points M3 and M4. The appearance of these valleys and peaks in the time-varying function can ensure a reliable and accurate measurement of the magnetic field intensity.

As also indicated in Figure 6.7, while the magnetic field measurements over time at Points M1 and M2 are significantly smoother than those at Points M3 and M4. This is mainly because the change in magnetic field when measured from west of the magnet is more sensitive to any small magnet rotation than that when measured from south of the magnet. This result is verified with slight improvement by the magnetic field measurements with a rise time of *1.0 sec*, as shown in Figure 6.8. Indeed, the use of longer rise time can reduce the sensitivity to any small rotation of the magnet when measured from off the north-south pole direction. The plateaus at peaks and valleys of the measured field intensities with longer rise time are much longer than those with a rise time of *0.5 sec*. However, further increase in rise time requires more time to complete field tests or more power consumption in practical applications. Overall, a rise time of *1.0 sec* appears an appropriate choice for the small APSS, leading to repeatable, periodic, and accurate magnetic fields when measured over time from any location.

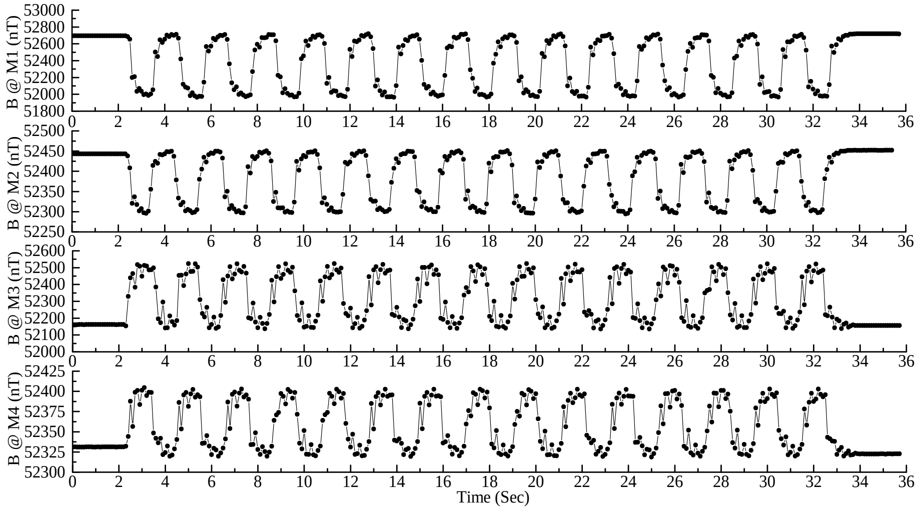

Figure 6.7. Magnetic field intensities measured at four points with a rise time of 0.5 sec.

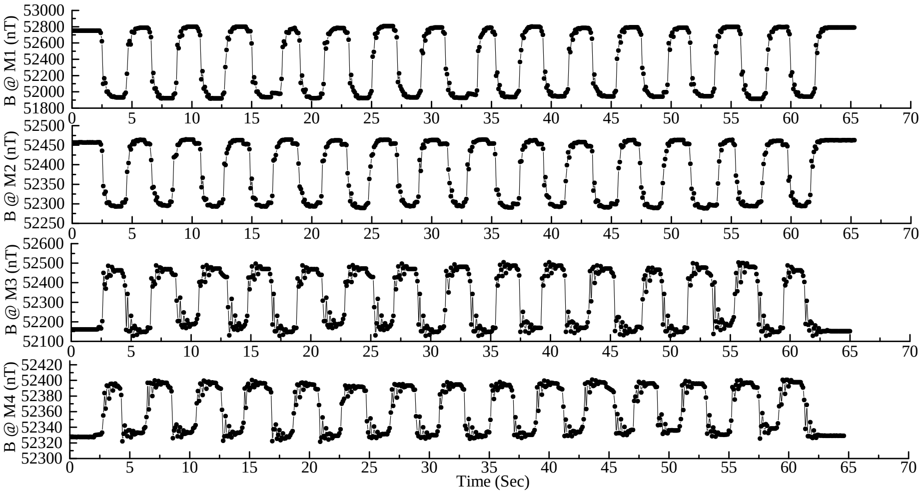

Figure 6.8. Magnetic field intensities measured at four points with a rise time of 1.0 sec.

6.4. APPLICATION OF SEMI-ACTIVE SMART ROCKS

In this section, the field tests using a full-size semi-active smart rock were also preformed in the open baseball field at Ber Juan Park to validate the characteristics of the magnetic intensity over time. Further, the localization algorithm proposed in Section 3 was improved to evaluate the location of the full-scale semi-active smart rock.

6.4.1. Test Setup with a Full-size Semi-active Smart Rock. The field tests were also performed in the open baseball field at Ber Juan Park. As indicated in Figure 6.9(a), the semi-active APSS was located at the origin of the Cartesian Coordinate O-XYZ. To locate the APSS, a sensor head of G858 Magnetometer was separately stationed at Q_1, Q_2, Q_3 …, Q_{25}, and Q_{26} as photographically and schematically showed in Figures 6.9(b) and 6.9(c), respectively. The 26 measurement points with the magnetometer sensor were selected to take into account the influence of inclination angle and distance on the magnetic field intensity as discussed in Section 3. They are represented by wooden poles and randomly distributed in height between two circles of 1.5 m and 5 m in diameter. A total station as shown in Figure 6.9(b) was set up at far distance to survey the APSS and 26 sensor positions with a prism placed on top of each wooden pole. The semi-active smart rock system is displayed in Figure 6.9(d), including a large APSS, a current coil tightly enclosing the APSS, a v3.0 PCB, a magnet rotation extension board, a current control, and a power supply. At a constant voltage of 3.6 V, the applied current periodically alternates between 0 and 1 A at a predetermined interval. A current rise time of 1.0 sec was programmed in the PCB to control the rotation of the magnet for each measurement point.

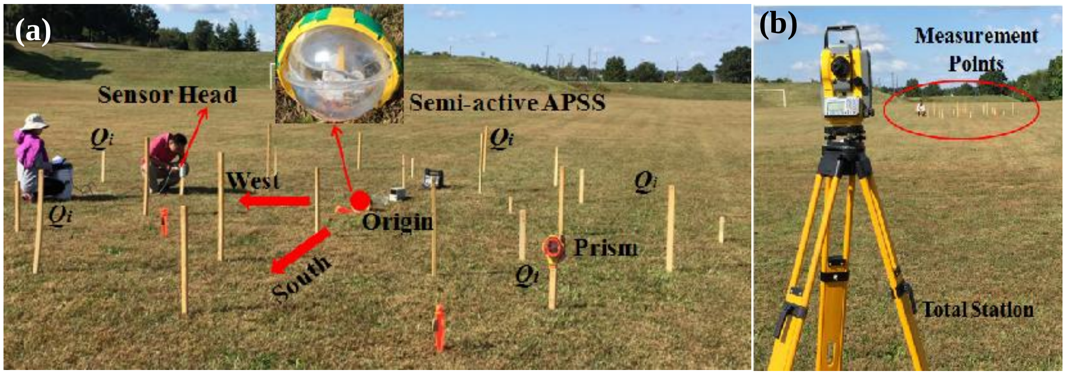

Figure 6.9. Experimental layout: (a) test setup, (b) total station for coordinate measurement, (c) measurement points, and (d) power, control, and APSS system.

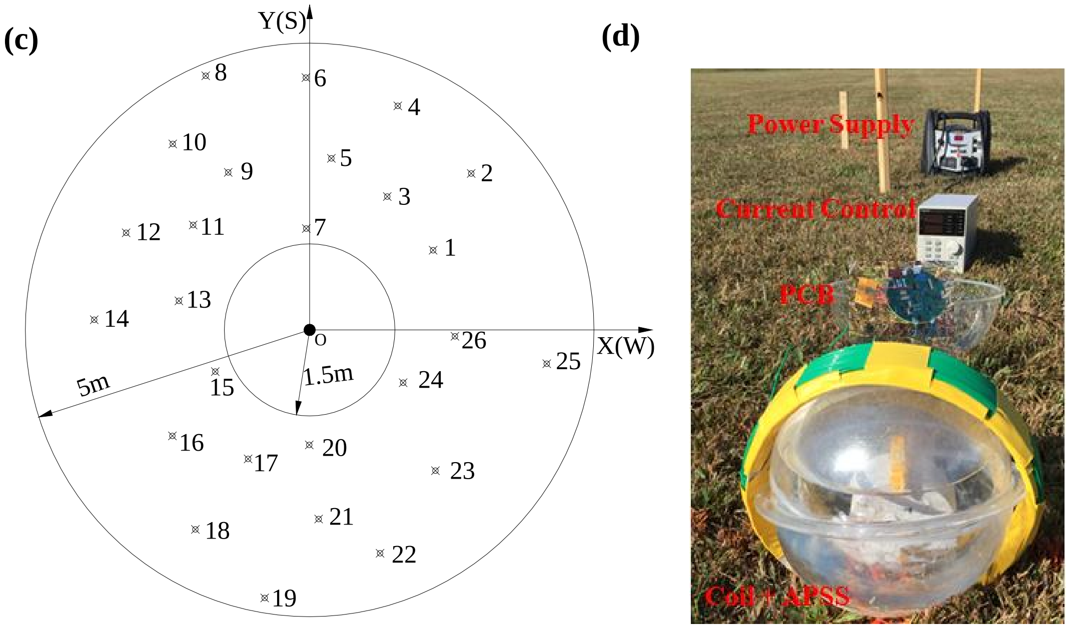

Figure 6.9. Experimental layout: (a) test setup, (b) total station for coordinate measurement, (c) measurement points, and (d) power, control, and APSS system (cont.).

6.4.2. Localization Algorithm. The general localization algorithm for an APSS in the open field was formulated in Section 3. Thus, it is briefly discussed here as an application to this particular case. Referring to Figure 6.10, a Cartesian coordinate system O-XYZ is selected with X-, Y-, and Z-axis pointing to west, south, and upward, respectively. Let the magnet in the APSS centered at the origin of the coordinate system, Point O (X_M, Y_M, Z_M), and measurements taken at Point Q_i (X_i, Y_i, Z_i) ($i=1, 2, \ldots, n$) near the APSS. The Earth's magnetic field is represented by the parallel vectors in YOZ plane expressed with two parameters of magnitude, B_E, and inclination angle, θ. The total magnetic field of the Earth and the APSS are measured at various Point Q_i, which is denoted as $B_{Ti}^{(M)}$. The total magnetic field can also be expressed into a summation of the measured $B_E^{(M)}$ and the computed magnetic field $\boldsymbol{B}_i$ of the APSS, which is denoted as $B_{Ti}^{(P)}$ and can be expressed into:

$$B_{Ti}^{(P)} = \sqrt{(B_{Xi})^2 + \left[B_{Yi} + (-B_E^{(M)} \cos{}^{-})\right]^2 + \left[B_{Zi} + (-B_E^{(M)} \sin{}^{-})\right]^2} \qquad (6.1)$$

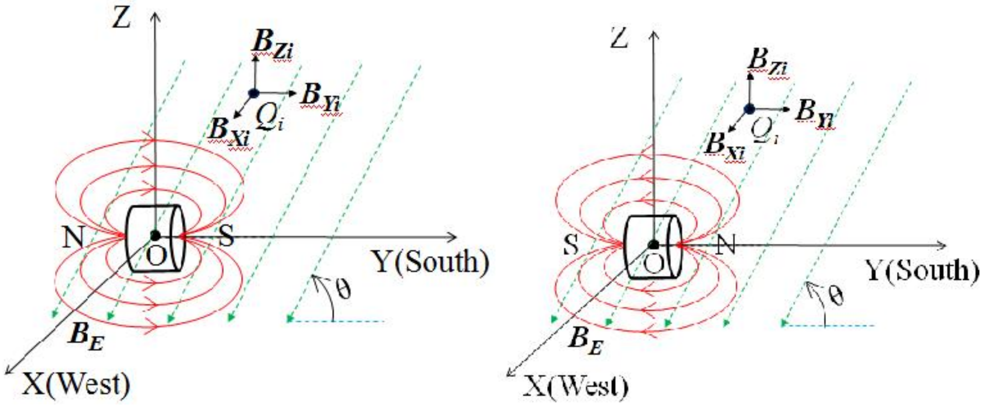

Figure 6.10. Two extreme orientations of the APSS: (a) Case A and (b) Case B

As the magnet rotates about X-axis, its magnetic field changes direction. For the two extreme cases in Figure 6.10, the Euler angles in the rotation matrix as discussed in Sections 3-5 are: $\alpha = \pi$, $\beta = 0$, and $\gamma = 0$ for Case A and $\alpha = 0$, $\beta = 0$, and $\gamma = 0$ for Case B. The magnetic fields at Point Q_i (X_i, Y_i, Z_i) can then be expressed into:

$$\begin{pmatrix} B_{Xi} \\ B_{Yi} \\ B_{Zi} \end{pmatrix} = \begin{pmatrix} -k\dfrac{3X_iY_i}{\left(X_i^{\,2}+Y_i^2+Z_i^{\,2}\right)^{\frac{5}{2}}} \\ -k\dfrac{2Y_i^2-X_i^{\,2}-Z_i^{\,2}}{\left(X_i^{\,2}+Y_i^2+Z_i^{\,2}\right)^{\frac{5}{2}}} \\ -k\dfrac{3Y_iZ_i}{\left(X_i^{\,2}+Y_i^2+Z_i^{\,2}\right)^{\frac{5}{2}}} \end{pmatrix} \text{ in Case A} \qquad (6.2a)$$

$$\begin{pmatrix} B_{Xi} \\ B_{Yi} \\ B_{Zi} \end{pmatrix} = \begin{pmatrix} k\dfrac{3X_iY_i}{\left(X_i^{\,2}+Y_i^2+Z_i^{\,2}\right)^{\frac{5}{2}}} \\ k\dfrac{2Y_i^2-X_i^{\,2}-Z_i^{\,2}}{\left(X_i^{\,2}+Y_i^2+Z_i^{\,2}\right)^{\frac{5}{2}}} \\ k\dfrac{3Y_iZ_i}{\left(X_i^{\,2}+Y_i^2+Z_i^{\,2}\right)^{\frac{5}{2}}} \end{pmatrix} \text{ in Case B} \qquad (6.2b)$$

To locate the APSS, an objective error function is defined into a SRSS difference of the predicted and the measured total magnetic field intensity at all measurement points Q_i ($i=1, 2,\ldots, n$). That is,

$$J(X_M, Y_M, Z_M) = \sqrt{\sum_{i=1}^{n} [B_{Ti}^{(P)} - B_{Ti}^{(M)}]^2} \tag{6.3}$$

Eq. (6.3) was minimized to solve for the coordinates of the APSS or Point $O(X_M, Y_M, Z_M)$. The Earth's magnetic field was measured around the 26 measurement points. The average value was determined to be $B_E = 51860$ nT·m^3. As discussed in Section 3, the coefficient k and θ at the same open site are $k = 42542$ nT·m^3 and $\theta = 67.7°$.

6.4.3. Magnetic Field Intensity over Time. Figure 6.11 shows the static and time-varying total magnetic intensities measured over time at selected twelve measurement points. Only two cycles of magnet rotation with a total of four current alternations were presented at each measurement point. It can be observed from Figure 6.11 that the constant field intensities at the beginning and end of the time functions collected at all points represent the static measurements with no magnet rotation (Case A as shown in Figure 6.10). The dramatic changes in intensity correspond to each and every switch of current in the rise time. The fluctuation immediately following each switch was associated with the back-and-forth rotation of the magnet due to the rotational inertia; it is gradually damped out before the next switch of current is activated, resulting in constant field intensities when the rotation of the magnet between Case A and Case B in Figure 6.10 is finally completed and stabilized. Upon two complete cycles of magnet rotation, the static measurements of field intensities are resumed.

Specifically, take the measurement at Point Q_3 in Figure 6.11 as an example. The static intensity between 1 sec to 5 sec represents Case A in Figure 6.10 when the south pole of the magnet is approximately oriented to the geographic South. Upon the first application of current controlled by the code programmed into the PCB, the south pole of the magnet is rotated and orientated to the opposite direction of the geographic South after the magnet has swung back and forth for a couple cycles under two competing forces: rotational inertia and magnetic force. The free vibration of the magnet corresponds to the intensity fluctuation between 6 sec and 11 sec. The constant intensity between 11 sec and 17.5 sec represents Case B in Figure 6.10 under the sustained current of 1 A. At approximately 17.5 sec, the current is switched off and the south pole of the magnet is rotated again and eventually oriented to the geographic South after a few cycle of free vibration between 18.5 and 24 sec. A short period of small change afterward represents Case A again. Although slightly different in details, the two halves of the cyclic response are similar, completing the full alternation of the orientation of the magnet. The cyclic behavior is repeated in the following on-off cycle of current.

The periodic responses in magnetic field are also observed at other measurement points as illustrated in Figure 6.11, validating the repeatability and periodicity of magnetic field intensities under periodic current excitations. With the semi-active smart rock, these features can be used to extract the intensity responses of a magnet in two cases (A and B) from a single measurement, thus improving the accuracy of rock positioning. The same features also enable the separation between the effects of the magnet and other ferromagnetic substances. This is because the intensities at peaks and valleys represent the summation and difference of the two magnetic field intensities generated from the magnet and the Earth. For all points except Q_{12}, the difference between each pair of peak and valley intensities or between Case A and Case B is significant. The exception at Point Q_{12} is because, as shown in Figure 6.9(c), it is located nearly along the east-west direction and least responsive to the rotation of the magnet.

Based on the free vibration responses at all measurement points in Figure 6.11, the damping ratio of the APSS can be estimated to be 1%. This level of damping verifies the low friction between the inside and outside balls of the APSS, validating its design for practical application.

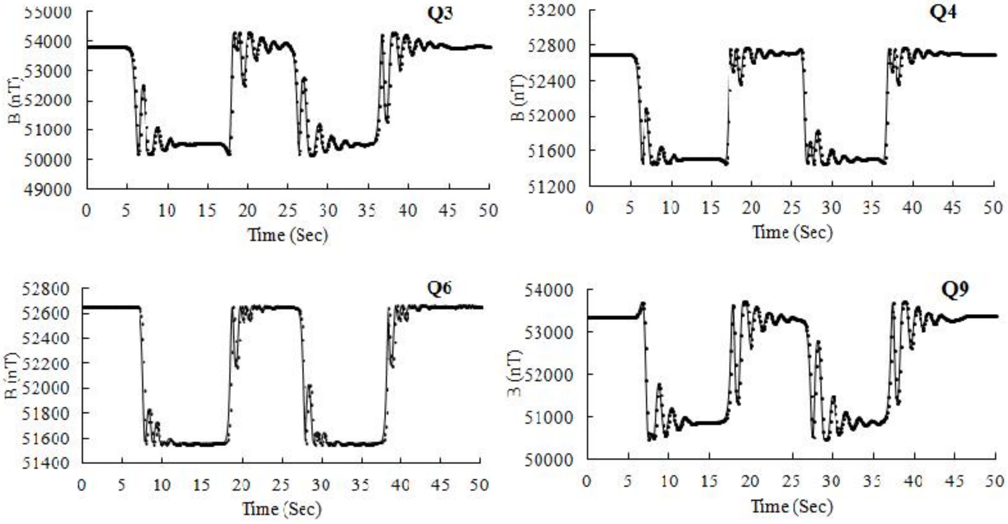

Figure 6.11. Total magnetic field intensities over time at various points.

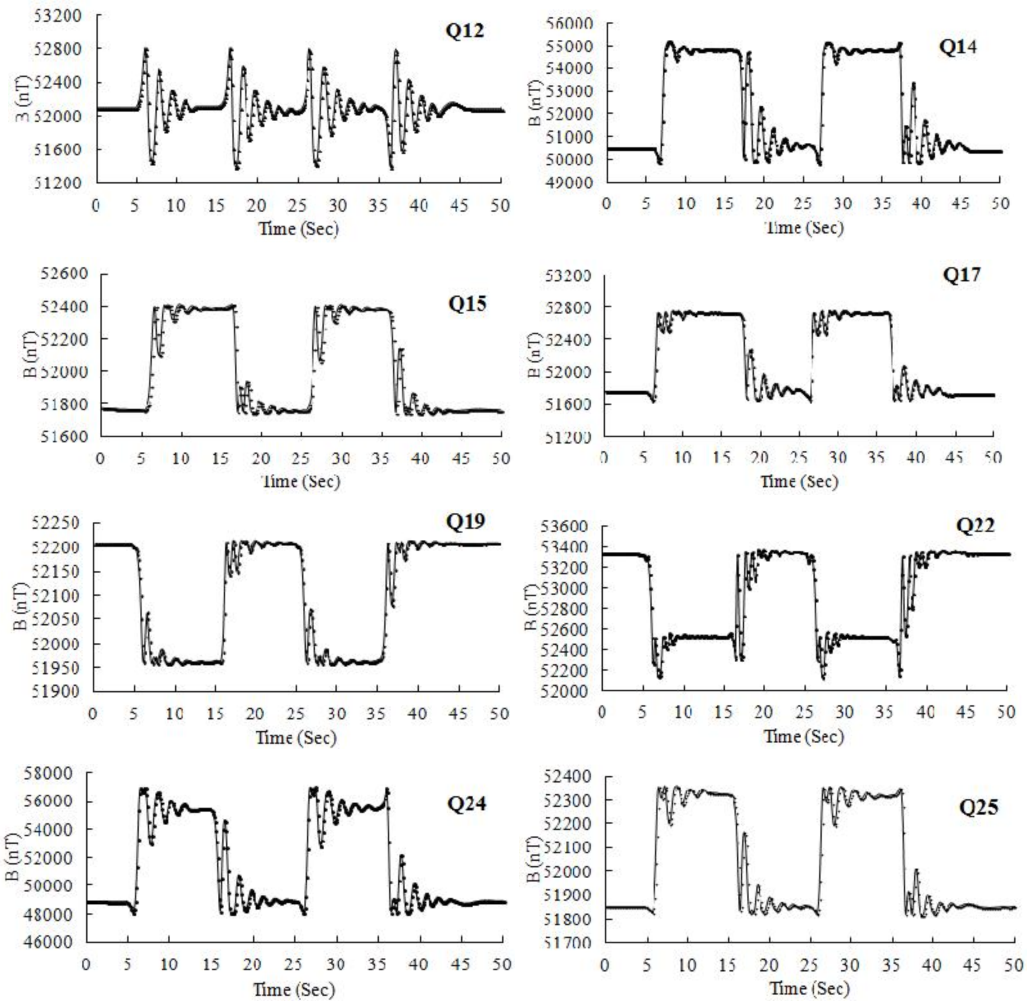

Figure 6.11. Total magnetic field intensities over time at various points (cont.).

6.4.4. Localization of Semi-active APSS. Table 6.1 indicates the coordinates and total magnetic intensities for Case A and Case B at 26 measurement points. Each total magnetic intensity for Case A represents an average of the static measurements at the beginning and end of tests at each point. Each total magnetic intensity for Case B is the average value of the stabilized data after the first application of current.

Table 6.2 summarizes the predicted coordinates from the two sets of data in Case A and Case B, compares the predicted with the measured coordinate, and presents the SRSS errors in the positioning of the semi-active APSS. Overall, the SRSS errors in location are 0.07 m and 0.05 m for Case A and Case B, respectively. These errors likely resulted from that the measurement of coordinates and intensities at all points, which may slightly differ from their expected locations. The nearby power supply may also affect slightly the measurement of magnetic field intensities. Nevertheless, the errors are quite small compared to the size of the magnet, which validates that the localization algorithm from two sets of data is quite accurate and reliable for application.

Table 6.1. Measured coordinates and intensities of the semi-active APSS

Measurement Point	X_i (m)	Y_i (m)	Z_i (m)	$B_{Ti}^{(M)}$ (10^4 nT) (Case A)	$B_{Ti}^{(M)}$ (10^4 nT) (Case B)
Q_1	2.17	1.39	0.88	5.314	5.111
Q_2	2.84	2.73	0.52	5.242	5.175
Q_3	1.37	2.33	0.29	5.381	5.053
Q_4	1.55	3.91	0.78	5.269	5.151
Q_5	0.38	2.99	0.89	5.408	5.020
Q_6	-0.07	4.40	0.67	5.265	5.156
Q_7	-0.06	1.77	0.68	6.201	4.308
Q_8	-1.83	4.43	0.23	5.235	5.183
Q_9	-1.43	2.75	0.75	5.337	5.088
Q_{10}	-2.41	3.24	0.27	5.238	5.183
Q_{11}	-2.05	1.83	0.43	5.275	5.166
Q_{12}	-3.23	1.69	0.68	5.210	5.211
Q_{13}	-2.30	0.51	0.69	5.149	5.292
Q_{14}	-1.66	-0.73	0.23	5.050	5.482
Q_{15}	-3.79	0.18	0.26	5.177	5.239
Q_{16}	-2.41	-1.85	0.46	5.189	5.233
Q_{17}	-1.08	-2.25	0.82	5.176	5.273
Q_{18}	-2.01	-3.48	0.62	5.223	5.198
Q_{19}	-0.79	-4.67	0.84	5.221	5.196
Q_{20}	0.16	-3.30	0.38	5.272	5.154
Q_{21}	1.24	-3.89	0.69	5.224	5.197
Q_{22}	-0.01	-2.01	0.53	5.332	5.253
Q_{23}	2.21	-2.45	0.53	5.199	5.224
Q_{24}	1.64	-0.92	0.94	4.888	5.541
Q_{25}	4.17	-0.59	0.52	5.185	5.233
Q_{26}	2.56	-0.11	0.32	5.110	5.300

Table 6.2. Predicted and measured coordinates of the semi-active APSS location

Location Coordinate	Case A			Case B		
	X_M (m)	Y_M (m)	Z_M (m)	X_M (m)	Y_M (m)	Z_M (m)
Predicted	0.06	-0.00	0.04	0.02	0.00	0.05
Measured	0.00	0.00	0.00	0.00	0.00	0.00
Prediction Error	0.06	-0.00	0.04	0.02	0.00	0.05
SRSS Error	0.07 m			0.05 m		

6.5. SUMMARY

In this section, a small-scale semi-active smart rock with an embedded, rotation-controllable magnet was first proposed, designed, and characterized for its performance in terms of the dynamic range of measurement, data repeatability, and differentiability between the effects of the magnet and its surrounding ferromagnetic substances. Then, a large-scale semi-active smart rock with the APSS proposed in Section 2 was designed and tested to realize the localization from time-varying data sets. Based on the field tests and analysis, the following conclusions can be drawn:

(1) The embedded magnet in small- and large-scale APSS can be rotated under external power by applying current through a coil that is wrapped around the magnet. The mechanism to make the magnet free to rotate is quite effective. Throughout each test period, the magnet in the APSS consistently rotated and stopped as expected.

(2) The magnetic field intensity induced by a rotating magnet over time takes the form of a time-varying function of the applied current through the electric coil wrapped around the magnet. The known variation of the field intensity over time (e.g. periodic) allows additional verifications on the quality of measured data.

(3) The time-varying magnetic field of a rotating magnet significantly differs from the static field of a stationary magnet. This difference can be used to separate the effects of magnets and other ferromagnetic substances, facilitating the detection of smart rocks in practical applications.

(4) The rise time of current excitation is a key factor to achieve repeatable and accurate measurements of the magnetic field induced by a magnet, depending on the magnet size and the sampling rate of a magnetometer. Specifically, the overshooting inertia force of a rotating magnet and current induced magnetic force determine a short

period of free vibration of the magnet. The level of vibration is governed by the damping of the APSS.

(5) The continuous data collection from an initial stationary magnet to the first rotation of the magnet and from the last rotating to the final stationary state can potentially be used to determine the orientation of the magnet with respect to the measuring point.

(6) The two sets of data before and after rotation of a magnet allow the dual localizations for the semi-active smart rock, resulting in higher reliability and accuracy in application.

7. CONCLUSIONS AND FUTURE WORK

7.1. MAIN FINDINGS FROM THE OVERALL DISSERTATION WORK

In this dissertation, a novel smart rock technology has been developed for the monitoring of bridge scour and riprap effectiveness and demonstrated at three bridge sites. Once properly designed, a smart rock functions like a field agent deployed around a bridge pier for rock positioning, and rolls to the bottom of a scour hole around the bridge pier. The position of the rock can be transformed to the maximum scour depth that is critical in bridge design and maintenance. The change in smart rock position can also be indicative of the disassembling process of a riprap mitigation measure. Therefore, a smart rock can also be referred to as a “scour and movement sensor” for scour depth measurement and riprap effectiveness monitoring.

The key technical challenge is to locate the smart rock before, during , and after a flood event. To address this challenge, three types of passive smart rocks with Arbitrarily Oriented System (AOS), Automatically Pointing South System (APSS), and Automatically Pointing Upward System (APUS) were developed and characterized in an open field and at a bridge site. Several localization algorithms were formulated based on the minimization of an objective error function between the predicted and measured magnetic field intensities. To further overcome the localization challenge, a semi-active smart rock was developed and characterized for the measurement of time-varying magnetic field intensities by rotating the magnet in smart rocks within a short period of time. Based on extensive test data and localization analysis, the following main conclusions can be drawn:

(1) The first model of smart rock with the AOS was developed by directly embedding a magnet in concrete encasement. It is small in size and easy to fabricate but less efficiency in computational time to determine the arbitrary orientation of the magnet. This model is not recommended for practical application.

(2) The second model of smart rock with the APSS was developed by making a magnet free to rotate like a compass needle so that the magnet is always oriented in approximate alignment with the geographic south of the Earth, simplifying the process of rock localization with the known magnet orientation. To locate the APSS effectively and

accurately, sufficient number of measurements should be taken along the extension of the south and north poles of the magnet since the field intensity at two poles is twice as much as that at equators. Thus, the APSS is most desirable when measured at river banks.

(3) The third model of smart rock with the APUS was developed by making the south pole of a magnet point upward with unbalanced weights, which is most desirable when measurements are taken from the bridge deck in bridge scour monitoring. In comparison with the APSS, the gravity-controlled APUS (e.g. orientation) is less affected by steel reinforcement and other ferromagnetic substances when deployed in proximity to a bridge pier, thus improving the accuracy of rock localization.

(4) For the purpose of rock localization, the effective measurement distance of a cylinder magnet depends on the maximum residual flux density and volume of the magnet and its relation with the measurement station. The larger the flux density and/or the volume, the stronger the magnetic field generated by the magnet and the further the measurement distance for effective magnetic field intensity. For the selected cylindrical magnet (N42) in this study, the most sensitive and reliable measurement distance ranges from *1.5 m* to *7.5 m*.

(5) The localization errors for the AOS and APSS at the open field site were less than *10 cm*, which is quite accurate and satisfactory. They may be caused by the non-perfect collocation of the measurement point and the magnetometer sensor and by the use of the averaged Earth's magnetic field of all measurement points.

(6) The localization errors of the AOS and APSS in the open river bank area near a bridge pier at the Gasconade River Bridge site were between *10 cm* and *20 cm* likely due to the non-perfect collocation of the measurement point, the magnetometer sensor for magnetic field measurement, and the AMFOD for direction measurement of the ambient magnetic field. The error for the APSS may also be attributed to a small rotation of the magnet in the ambient magnetic field particularly when the APSS was located near the bridge pier.

(7) In comparison with the APSS, the gravity-controlled APUS is not affected by the presence of steel reinforcement in nearby bridge piers in application. The smart rocks with the APUS were implemented around scour critical piers of the three bridges. A single smart rock was successfully located with an accuracy of less than *0.5 m*, a target

set forth with bridge engineers. However, the localization of two smart rocks led to a prediction error of over *1.0 m*. This is mainly attributed to the non-optimal selection and distribution of the measurement points due to physical limits, and the error in ground truth data for the location of smart rocks underwater.

(8) At the I-44W Roubidoux Creek Bridge site, the prediction errors of one smart rock with the APUS were less than 35 cm based on three series of field tests in different seasons, which is satisfactory in engineering application. The reasons for the errors may include the influence of passing vehicles during intensity measurements, the non-perfect collocation of measurement points and the sensor head as a result of wind induced movement, and the potentially-misplaced bar in the process of acquiring ground truth location of the smart rock.

(9) At the State Hwy1 Waddell Creek Bridge site, the smart rock deployed around the south abutment was located with a prediction error of *0.36 m* mainly due to wind induced movement of the sensor during the first series of tests. The single smart rock deployed near Bent 2 during the second series of field tests was located with a prediction error of *0.27 cm*, which was less than the diameter of the smart rock and acceptable for engineering application.

(10) At the US Hwy63 Gasconade River Bridge site, the smart rock deployed in the upstream of Bent 4 was located with a prediction error of *0.46 m*, which is still acceptable for engineering application. The larger error at this particular site was largely because this bridge is much higher than the other two bridges and the measurement points are farther away from the deployed smart rock.

(11) The semi-active smart rock with a rotation-controllable APUS significantly overcomes several challenges with the passive smart rocks as stated in the first ten conclusions. Under current excitation, the magnet rotates in a predetermined function and generates a time-varying magnetic field intensity. One time-varying measurement gives multiple useful parameters such as the maximum and minimum intensities with two extreme orientations of the magnet and the free vibration of the magnet as a result of the interaction between two balanced inertial and magnetic forces. Therefore, the time-varying measurement enables the separation of ambient magnetic field from that of the magnet successfully. The unique data set taken before, during, and after the magnet

rotation also allow an accurate localization of two smart rocks. Magneto-inductive communication with individual smart rocks may further help locate them reliably in field conditions.

7.2. FUTURE WORK

Although the potential of the smart rock technology has been successfully demonstrated to certain extent in an open field and at three bridge sites, this project represents the first study of smart rock implementation. For practical applications, several improvements can be made in the following directions:

(1) The spherical smart rocks with *0.368 m* in diameter and a density of $1495\ kg/m^3$ deployed at three bridge sites were designed based on the critical velocity of water flow. The rocks directly placed on the riverbed at the State Hwy1 Waddell Creek Bridge and US Hwy63 Gasconade River Bridge sites were washed away due to tidal waves from the Pacific Ocean in California and the December 27, 2015, flood in Missouri, respectively. For the monitoring of riprap effectiveness, a polyhedral shape of smart rocks is recommended since it can provide the interlock with other natural rocks in the riprap measure. For the measurement of scour depth, spherical rocks may be embedded in deposits to ensure their top is flush with the riverbed surface and increase their resistance to water current. More studies to derive accurate hydraulics data at bridge sites are needed to improve the design of smart rocks.

(2) The custom-built crane used to facilitate the field tests for measurements at close distance to the deployed smart rocks has been demonstrated to be effective. However, the assembling of such a crane takes more than one hour and its operation requires lane closure on the bridge deck. The awkward crane also limits the number of measurement points in application. Therefore, future research is directed to the development of a mobile platform with an unmanned aerial vehicle (UAV) so that measurements can be taken above water in the vicinity of bridge piers without interrupting traffic on the bridge. The effects of the UAV on the magnetic field and the operation speed on the measured data need to be investigated.

(3) Using a total station to survey smart rocks and magnetometer sensors for their coordinates is viable during field tests but not conducive in terms of efficiency and

accuracy. A high accuracy positioning system that is integrated into the smart rocks and magnetometer sensors would be desirable.

(4) The Earth's magnetic field and the secondary field of magnetized ferromagnetic substances at and around a bridge change over time. After smart rocks have been deployed near the bridge, the time-varying measurements can no longer be taken accurately. Therefore, a well-calibrated mathematic model of the ambient magnetic field at the bridge site was highly desirable so that the time-varying magnetic field can be simulated consistently and accurately.

BIBLIOGRAPHY

[1] Lagasse, P.F., Richardson, E.V., Schall, J.D., and Price, G.R. (1997). “Instrumentation for measuring scour at bridge piers and abutments.” *NCHRP Report 396*: TRB, National Research Council, Washington, D.C..

[2] N.T.S.B. (1987). “Collapse of New York Thruway (I-90) Bridge, Schoharie Creek, near Amsterdam, New York, April 5, 1987.” NTSB Number: HAR-88/02, NTIS Number: PB88-916202.

[3] N.T.S.B. (1989). “Collapse of the northbound U.S. Route 51 Bridge spans over the Hatchie River, near Covington, Tennessee, April 1, 1989.” NTSB Number: HAR-90/01, NTIS Number: PB90-916201.

[4] Arneson, L.A., Zevenbergen, L.W., Lagasse, P.F., and Clopper, P.E. (2012). “Hydraulic Engineering Circular No.18: Evaluating Scour at Bridges.” *5th Edition, U.S. Department of Transportation*, Federal Highway Administration, Publication No. FHWA-HIF-12-003.

[5] Brice, J.C., and Blodgett, J.C. (1978). “Countermeasures for hydraulic problems at bridges.” Vol. 1 & 2, FHWA/RD-78-162 & 163, Federal Highway Administration, U.S. Department of Transportation, Washington, D.C.

[6] Butch, G.K. (1996). “Evaluation of selected instruments for monitoring scour at bridges in New York.” *North American Water and Environment Congress*, ASCE.

[7] Mueller, D. S. (2000). “National bridge scour program-measuring scour of the streambed at highway bridges.” *U.S. Geological Survey*, Reston, VA.

[8] Rhodes, J. and R. Trent (1993). “Economics of floods, scour, and bridge failures.” *Hydraulic Engineering*, ASCE.

[9] Lagasse, P. F., Clopper, P. E., Pagán-Ortiz, J. E., Zevenbergen, L. W., Arneson, L. A., Schall, J. D., and Girard, L. G. (2009). “Bridge scours and stream instability countermeasures: experience, selection and design guidance.” *Hydraulic Engineering Circular No. 23*, Volume I, FHWA NHI HEC-23, Department of Transportation, Federal Highway Administration, Washington, D.C..

[10] Ali, K. H. and O. Karim (2002). “Simulation of flow around piers.” *Journal of Hydraulic Research*, 40(2),161-174.

[11] Salaheldin, T. M., et al. (2004). “Numerical modeling of three-dimensional flow field around circular piers. ” *Journal of Hydraulic Engineering*, 130(2), 91-100.

[12] Landers, M. N., and Mueller, D. S. (1996). “Evaluation of selected pier scour equations using field data.” *Journal of Transportation Research Record*, No. 1523, 186-195.

[13] Richardson, E. V., and Davis, S. R. (2001). “Evaluating scour at bridges.” *Hydraulic Engineering Circular 18, 5th Edition*, FHWA NHI 01-001, Federal Highway Administration, U.S. Department of Transportation, Washington, D. C.

[14] Hunt. B.E. (2009). “Monitoring scour critical bridges: A Synthesis of Highway Practice.” *NCHRP Synthesis Report 396. Transportation Research Board, National Academy of Science*, Washington, D.C. .

[15] Lueker M., Marr J., Ellis C., Hendrickson A., and Winsted V. (2010). “Bridge scour monitoring technologies: development of evaluation and selection protocols for application on river bridges in Minnesota.” *International conference on scour and erosion* 2010, 949-957.

[16] Briaud, J. L., and Hunt, B. E. (2006). “Bridge scour & the structural engineer.” *Structures Magazine*, 58-61.

[17] Fukui J. and Otuka M. (2002). “Development of the New Inspection Method on Scour Condition around Existing Bridge Foundations”. *First International Conference on Scour of Foundation (ICSF-1)*, University Drive East, College Station, Texas. EEUU.

[18] Forde M.C., McCann D.M, Clark M.R, Broughton K.J, Fenning P.J and Brown A. (1999). “Radar Measurement of Bridge Scour.” *NDT&E International*, 32, 481-492.

[19] Gorin, S. R., and Haeni, F. P. (1989). “Use of surface-geophysical methods to assess riverbed scour at bridge piers.” *U.S. Geological Survey Water-Resources Investigations Rep. No. 88-4212*, Federal Highway Administration, 33.

[20] Horne, W. A. (1993). “Scour inspection using ground penetrating radar.” *Proc., National Conf. on Hydraulic Engineering*, San Francisco, 1888–1893.

[21] Millard, S. G., Bungey, J. H., Thomas, C., Soutsos, M. N., Shaw, M. R., and Patterson, A. (1998). “Assessing bridge pier scour by radar.” *NDT Int.*, 31(4), 251–258.

[22] Webb D. J., Anderson N.L., Newton T. and Cardimona S. (2000). “ Bridge Scour: Application of Ground Penetration Radar.” *Federal Highway Administration and Missouri Department of Transportation special publication*,1-19.

[23] Schall J.D. and Price G.R. (2004).“Portable Scour Monitoring Equipment.” *NCHRP Report-515*, Transportation Research Board, Washington D.C.

[24] Park, I., Lee, J., and Cho, W. (2004). “Assessment of bridge scour and riverbed variation by ground penetrating radar.” *Proc., 10th Int. Conf. on Ground Penetrating Radar, GPR 2004*, Delft, The Netherlands, 411–414.

[25] Mason, R. R., and Shepard, D. M. (1994). “Field performance of an acoustic scour-depth monitoring system.” *Proc., Fundamentals and Advancements in Hydraulic Measurements and Experimentation*, New York, 366–375.

[26] Hayes, D. C., and Drummond, F. E. (1995). “Use of fathometers and electrical-conductivity probes to monitor riverbed scour at bridges and piers.” *Water Resource Investigations Rep. No. 94-4164*, U.S. Geological Survey, Hartford, Connecticut.

[27] Okoshi M. and Fukui J. (2001) “Present of Investigation technique for Scouring”. *The Foundation Engineering and Equipment*, 29(9), 19-21.

[28] Lu D. and C. S.Cai (2010). “ Bridge Scour: Prediction, Modeling, Monitoring and Countermeasures- -Review.” *Practice Periodical on Structural Design and Construction*, 15(2),125-134.

[29] Browne Terence M., (2010). “ Underwater Acoustic imaging devices for portable scour monitoring.” *International conference on scour and erosion 2010* (*ISCE-5*), *Scour and Erosion*, 931-940.

[30] Xiong W., Cai C.S., and Kong X.. (2012). “Instrumentation design for bridge scour monitoring using fiber Bragg grating sensors.” *Applied Optics*,51(5),547-557.

[31] Schall, J.D., G.R. Price, G.A. Fisher, P.F. Lagasse, and E.V. Richardson (1997b). “Magnetic Sliding Collar Scour Monitor – Installation, Operation and Fabrication Manual. ” *NCHRP Report 397B, Transportation Research Board, National Research Council, National Academy Press*, Washington, D.C.

[32] Lu, J.Y., Hong, J.H., Su, C.C., Wang, C.Y., and Lai, J.S. (2008). “Field measurements and simulation of bridge scour depth variation during floods.” *J. Hydra. Eng.*, 134(6), 810–821.

[33] Avila, C. M. C., Racin, J. A., and Davies, P. (1999). “Talk to your bridges and they will talk back—Caltrans bridge scour monitoring program.” *Proc., ASCE Hydraulic Conf.*, ASCE, New York.

[34] Zarafshan, A., Iranmanesh, A., and Ansari, F. (2011). “Vibration-based method and sensor for monitoring of bridge scour.” *Journal of bridge engineering*, 17(6), 829-838.

[35] M. I. Ibrahimy and S. M. A. Motakabber (2015)."Bridge scour monitoring by coupling factor between reader and tag antennas of RFID system." International Journal of Geomaterial, 8(2), 1328-1332.

[36] Dowding, C. H., and Pierce, C. E. (1994). “Use of time domain reflectometry to detect bridge scour and monitor pier movement.” *Proc., Symp. And Workshop on Time Domain Reflectometry in Environmental, Infrastructures and Mining Applications,* Northwestern Univ., Evanston, IL, 579-587.

[37] Yankielun, N. E., and Zabilansky, L. (1999). “Laboratory investigation of time-domain reflectometry system for monitoring bridge scour.” *J. Hydra. Eng.*, 125(12), 1279–1284.

[38] Yu, X., and Zabilansky, L. J.(2006). “Time domain reflectometry for automatic bridge scour monitoring.” *Geotechnical Special Publication*,149, 152–159.

[39] Yu, X.B., and Yu, X. (2007). “Algorithm for time domain reflectometry bridge scour measurement system.” *Proc., 7th Int. Symp. on Field Measurements in Geomechanics, FMGM 2007*, Boston, 1–10.

[40] Yu, X.B., and Yu, X. (2009). “Time domain reflectometry automatic bridge scour measurement system: Principles and Potentials.” *Structural. Health Monitoring,* 8(6), 463-476.

[41] Yu, X. B., and Yu, X. (2011a). “Development and evaluation of an automation algorithm for a time-domain reflectometry bridge scour monitoring system.” *Canadian Geotechnical Journal*, 48(1), 26-35.

[42] Yu X. B. and Yu X. (2011b). “Assessment of an automation algorithm for TDR bridge Scour monitoring system.” *Advances in Structural Engineering*, 14(1), 13-24.

[43] Yu, X. B., and Yu, X. (2010). “Laboratory Evaluation of Time-Domain Reflectometry for Bridge Scour Measurement: Comparison with the Ultrasonic Method. ” *Advances in Civil Engineering*, Vol. 2010, 1-12.

[44] Yu, X. B., Zhang, B., Tao, J., and Yu, X. (2013). “A New Time Domain Reflectometry Bridge Scour Sensor.” *Structural Health Monitoring*, 12(2), 99-113.

[45] Tao J. L., X. B. Yu, and X. Yu. (2013). “Real-time TDR Field Bridge scour monitoring system.” *Structure congress*, 2996-3009.

[46] Gao Q. and Yu X. (2015). “Design and evaluation of a high sensitivity spiral TDR scour sensor. ” *Smart Materials and Structures*, 24, 1-9.

[47] Joan, R. C. and Paulo J. S.C. (2003). “Fiber optic sensors for bridge monitoring.” *Journal of Bridge Engineering*, 8(6), 362-373.

[48] Ansari, F. (2010) “Simple cost-effective scour sensor.” *Research Report ICT-10-070*, Illinois Center for Transportation.

[49] Lin, Y. B., Chang, K. C., Lai, J.-S., and Wu, I.-W. (2004). “Application of optical fiber sensors on local scour monitoring.” *Proc., IEEE Sensors*, Vol. 2, Vienna, Austria, 832–835.

[50] Lin, Y. B., Chen, J.-C., Chang, K.-C., Chern, J.-C., and Lai, J.-S. (2005). “Real-time monitoring of local scour by using fiber Bragg grating sensors.” *Smart Material and Structures*, 14(4), 664–670.

[51] Lin Y.B, Lai J.S, Chang K.C and Li L.S. (2006), “Flood Scour Monitoring System Using Fiber Bragg Grating Sensors”. *Smart materials and Structures*,15(6), 1950-1959.

[52] Huang L.-Q., Wang D.-J. and Zhou Z. (2007) “A New Type of Optical FBG-based Scour Monitoring Sensor”. *Pacific Science Review*, 9(1), 103-109.

[53] Zhou. Z., Huang M.H., Huang L.Q., Ou J.P., and Chen G.D. (2011). “An optical fiber Bragg grating sensing system for scour monitoring.” *Advances in structural engineering*, 14(1), 67-78.

[54] Kong X., Cai C.S., Hu J.X., Xiong W. and Peng H. (2016) “Field application of an innovative bridge scour monitoring system with Fiber Bragg Grating Sensors. ” *Journal of Aerospace Engineering*, B4016008,1-10.

[55] John. I. II, Dr. M. Saafi, J. Jow, K. Rose, and P. Romine. (2007). “Sensor networks for bridge stability safety monitoring during flood induced scour.” *Structure Congress*.

[56] Fan, W., Wang, H., Wang, C., and Chen, M. (2008). “Piezoelectric type real-time scouring monitoring sensor at the foundation of bridge pier. ” *World Forum on Smart Materials and Smart Structures Technology*, CRC Press.

[57] Wang C., Wang H. and Ho C. (2012) “A piezoelectric film type scour monitoring system for bridge pier.” *Advances in structural engineering*, 15(6), 897-905.

[58] Prendergast L.J. and Gavin K. (2014) “A review of bridge scour monitoring techniques.” *Journal of Rock Mechanics and Geotechnical Engineering*, 2014, 6(2), 138-149.

[59] Camp, C.V., Pezeshk, S., and Leatherwood, T.D. (1998) “Detecting bridge scour by measuring the thermal variation across the stream bed.” *International Water Resources Engineering Conference*, Memphis, TN, 1998, August 3-6.

[60] Cigada A., Ballio F., Inzoli F. (2008) “Hydraulic Monitoring Unit.” *Application for international patent N*. PCT/EP2008/059075.

[61] Manzoni, S., Crotti, G., Cigada, A., Inzoli, F., and Ballio, F. (2010) “Monitoring bridge scour by Bragg grating array.” *Scour and Erosion*: *Proceedings of 5th International Conference on Scour and Erosion*, ASCE, November 7-10, 2010, San Francisco, CA.

[62] Manzoni, S., Crotti, G., Ballio, F., Cigada, A., and Colombo, E. (2011) “BLESS: A fiber optic sedimeter.” *Flow Measurement and Instrumentation*, 22(5), 447–455.

[63] Ding Y., Yan T., Dong X., Wang X. (2016) “A new type of temperature-based sensor for monitoring of Bridge scour.” *Measurement*, 2016, 78, 245-252.

[64] Amirmojahedi M., Akib S., Basser H. and Ooi CH R. (2016) “Methods for monitoring scour from large-diameter heat probe tests.” *Structural Health Monitoring*, 15(1), 38-49.

[65] Samizo, M., Watanabe, S., Sugiyama, T., and Okada, K. (2010) “Evaluation of the structural integrity of bridge pier foundations using microtremors in flood conditions.” *Scour and Erosion: Proceedings of 5th International Conference on Scour and Erosion*, ASCE, November 7-10, 2010, San Francisco, CA.

[66] Ko Y. Y., Lee W.F., Chang W. K., Mei H. T., and Chen C. H. (2010) “Scour evaluation of bridge foundations using vibration measurement.” *International Conference on Scour and Erosion*, 2010, 884-893.

[67] Yao C., Darby C., B., Yu O.-Y., Hurlebaus S., Chang K.-A., Price J., Hunt B., and Briaud J.-L. (2010) “Motion Sensors for Scour Monitoring: Laboratory Experiment with a Shallow Foundation.” *GeoFlorida: Advances in Analysis, Modeling and Design*, 970-979.

[68] Fisher M, Chowdhury MN, Khan AA, Atamturktur S. (2013) “An evaluation of scour measurement devices.” *Flow Measurement and Instrumentation*, 33, 55-67.

[69] L. J. Prendergast, D. Hester, K. Gavin, J. J. O'Sullivan (2013). “An investigation of the changes in the natural frequency of a pile affected by scour.” *Journal of Sound and Vibration*, 332, 6685-6702.

[70] L.J. Prendergast, D. Hester, K. Gavin (2016). “Determining the presence of scour around bridge foundations using vehicle-induced vibrations.” *Journal of Bridge Engineering*. 04016065-1-14.

[71] R. P. Palanisamy and S-H. Sim (2015). “Bridge scour monitoring using extended Kalman filter.” *6th International Conference on Advances in Experimental Structural Engineering, 11th International Workshop on Advanced Smart Material and Smart Structures Technology*, August 1-2, 2015, University of Illinois, Urbana-Champaign, United States.

[72] Lin, Y. B., Lai, J. S., Chang, K. C., Chang, W. Y., Lee, F. Z., and Tan, Y. C. (2010). “Using mems sensors in the bridge scour monitoring system.” *Journal of the Chinese Institute of Engineers*, 33(1), 25-35.

[73] Chang, W.-Y., Lai, J.-S., Tsai, W.-F., Lee, L.-C., Lin, F., and Loh, C.-H. (2012). “Multi-lens pier scour monitoring and scour depth prediction.” *Proceedings of the ICE - Water Management*, 1-17.

[74] Lauth T.J., Papanicolaou A. N. (2008). “Experimental/Feasibility Study of Radio Frequency Tracers for Monitoring Sediment Transport and Scour around Bridges.” *World Environmental and Water Resources Congress* 2008, 1-10.

[75] Chen S, Chen Z.J. and Wang W. (2010). “Multi-Scale Detection Technics for Local Scour Monitoring in River Bed: Case Study, at Sutong Bridge.”, *ASCE Conf., Earth & Space*, 2010, 2431-2441.

[76] Chen S., Sun Y.-X. and Liu D.-W. (2012). “Monitoring technique for local scour around bridge pier.” *Earth and Space*, 914-919.

[77] Shin, J. H., and Park, H. (2010). “Development and Application of a 3-Dimensional Scour Monitoring System for Sea-Crossing Bridge Piers.” *International Journal of Offshore and Polar Engineers,* 20(4), 292-297.

[78] Jesse T. H. and Jack A. P. (2011). “Near real-time scour monitoring system: application to Indian River Inlet, Delaware.” *Journal of Hydraulic Engineering*, 137(9),1037-1046.

[79] Chang W.-Y., Lai J.-S., Yu T.-Y., et al.(2014) “Pier scour monitoring system by bed-level image tracking. ” *International Journal of sediment Research*, 29, 269-277.

[80] Swarta R. A., Rajbandari B. and Winter B. D. (2014) “Autonomous scour monitoring of bridges and embankments using bio-inspired whisker flow sensor arrays.” *Proceedings of the ASME 2014 conference on Smart Materials, Adaptive Structures and Intelligent Systems*, 2014, Newport, Rhode Island, USA, 1-5.

[81] C-C Chen, C-C Yang, S-Y Chen, W-C Chen, G-N Sung, C-T Kuo, Y-J Hsien, C-M Wu and C-M Huang (2015). “Hall effect sensors for real-time monitoring pier scour. ” *Sensors and Transducers*, 184(1), 11-18.

[82] C-C Yang, S-Y Chen, Y-J Hsien, F-C Cheng, Y-C Huang, J-J Chue, C-T Kuo, C-M Wu and C-M Huang (2016). “A rugged sensor for real-time bridge safety monitoring in Taiwan.” *Sensors Applications Symposium (SAS), IEEE*, 1-5.

[83] Michalis P., Tarantino A., Tachtatzis C. and Judd M. D. (2015). “Wireless monitoring of scour and redeposited sediment evolution at bridge foundations based on soil electromagnetic properties. ” *Smart Materials and Structures*, 24(12),1-15.

[84] Azhari F., Scheel P. J. and Loh K. J. (2015). “Monitoring bridge scour using dissolved oxygen probes.” *Structural monitoring and Maintenance*, 2(2), 145-164.

[85] Weitschies, W., et al. (1994). “Magnetic markers as a noninvasive tool to monitor gastrointestinal transit. ” *IEEE Transactions on Bio-medical Engineerin*g, 41(2), 192-195.

[86] E. P. Furlani, S. Reznik, and A. Kroll (1995). “A three-dimensional field solution for radially polarized cylinders, ” *IEEE Transactions on Magnetics*, 31(1), 844-851.

[87] S. I. Babic and C. Akyel (2008). “Magnetic force calculation between thin coaxial circular coils in air. ” *IEEE Transactions on Magnetics*, 44(4), 445-452.

[88] Derby, N. and S. Olbert (2010). “Cylindrical magnets and ideal solenoids. ” *American Journal of Physics***,** 78(3), 229-235.

[89] Model, R. and L. Trahms (1993). “An inverse problem of magnetic source localization.” *Numerical Algorithms*, 5(12), 603-610.

[90] Raab, F. H., et al. (1979). “Magnetic position and orientation tracking system.” *IEEE Transactions on Aerospace and Electronic Systems*, AES-15(5): 709-718.

[91] Prakash, N. M. and F. Spelman (1997). “Localization of a magnetic marker for GI motility studies: an in vitro feasibility study.” *Engineering in Medicine and Biology Society*, *Proceedings of the 19th Annual International Conference of the IEEE.*

[92] Schlageter, V., et al. (2001). “Tracking system with five degrees of freedom using a 2D-array of Hall sensors and a permanent magnet.” Sensors *and Actuators A: Physical*, 92(1), 37-42.

[93] Yabukami, S., et al. (2000). “Motion capture system of magnetic markers using three-axial magnetic field sensor. ” *IEEE Transactions on Magnetics*, 36(5), 3646-3648.

[94] Plotkin, A. and E. Paperno (2003). “3-D magnetic tracking of a single subminiature coil with a large 2-D array of uniaxial transmitters. ” *IEEE Transactions on Magnetics*, 39(5), 3295-3297.

[95] Jiang, S., et al. (2008). “Dipole source localization by means of simplified double magnetic dipole model.” *International Journal of Bioelectromagnetism*, 10(2),111-123.

[96] Wang, X., et al. (2004). “A low-cost tracking method based on magnetic marker for capsule endoscope.” *International Conference on Information Acquisition*, 2004, IEEE.

[97] Yang, W., et al. (2009). “A new 6D magnetic localization technique for wireless capsule endoscope based on a rectangle magnet.” *Chinese Journal of Electronics*, 19(2), 360-364.

[98] Yang, W., et al. (2010). “A new tracking system for three magnetic objectives.” *IEEE Transactions on Magnetics*, 46(12), 4023-4029.

[99] Hu, C., et al. (2007). “A linear algorithm for tracing magnet position and orientation by using three-axis magnetic sensors.” *IEEE Transactions on Magnetics*, ***43***(12), 4096-4101.

[100] Hu, C., et al. (2010). “A cubic 3-axis magnetic sensor array for wirelessly tracking magnet position and orientation. ” *IEEE Sensors Journal*, 10(5), 903-913.

[101] He, X., et al. (2015). “Magnetic localization and orientation of the capsule endoscope based on a random complex algorithm.” *Medical Devices (Auckl*), 8, 175-184.

[102] Boggs, P. T. and J. W. Tolle (1989). “A strategy for global convergence in a sequential quadratic programming algorithm.” *SIAM Journal on Numerical Analysis*, 26(3), 600-623.

[103] Http: //www. geometrics. com /geometrics-products/ geometrics – magnetometers /g-858-magmapper/.

[104] Radchenko, A., et al. (2013). “Real-time bridge scour monitoring with magneto inductive field coupling.” *Proceedings of Sensors and Smart Structures Technologies for Civil, Mechanical, and Aerospace Systems*, SPIE 2013 Conference, San Diego, CA.

VITA

Yan Tang was born in the City of Baiyin, Gansu, China. She was admitted to Lanzhou Jiaotong University, Lanzhou, Gansu, China, in 2004 and received her B.S. degree in Hydraulic and Hydro-power Engineering in 2008. Upon graduation in 2008, she was directly admitted into her graduate study in Lanzhou Jiaotong University, Lanzhou, Gansu, China and received her M.S. degree in Hydraulic and Hydro-power Engineering in 2011. Then, she was admitted into her PhD program in Hydraulic and Hydro-power Engineering at China Institute of Water Resources and Hydropower Research, Beijing, China in 2011. In 2013, she transferred to the PhD Program in Civil Engineering at Missouri University of Science and Technology under the supervision of Professor Genda Chen. She has served as a Graduate Research Assistant between January 2013 and December 2016 in the Department of Civil, Architectural, and Environmental Engineering. During this period, her research interests were focused on the innovation and application of smart rock technology for bridge scour monitoring. Based on her dissertation work, she has authored two conference papers, co-authored three Journal papers and three conference papers. In addition, two more were in preparation for potential publication. In May 2017, she received her Ph. D. degree in Civil Engineering from Missouri University of Science and Technology, Rolla, Missouri.